

INFORMATION TO USERS

This manuscript has been reproduced from the microfilm master. UMI films the text directly from the original or copy submitted. Thus, some thesis and dissertation copies are in typewriter face, while others may be from any type of computer printer.

The quality of this reproduction is dependent upon the quality of the copy submitted. Broken or indistinct print, colored or poor quality illustrations and photographs, print bleedthrough, substandard margins, and improper alignment can adversely affect reproduction.

In the unlikely event that the author did not send UMI a complete manuscript and there are missing pages, these will be noted. Also, if unauthorized copyright material had to be removed, a note will indicate the deletion.

Oversize materials (e.g., maps, drawings, charts) are reproduced by sectioning the original, beginning at the upper left-hand corner and continuing from left to right in equal sections with small overlaps. Each original is also photographed in one exposure and is included in reduced form at the back of the book.

Photographs included in the original manuscript have been reproduced xerographically in this copy. Higher quality 6" x 9" black and white photographic prints are available for any photographs or illustrations appearing in this copy for an additional charge. Contact UMI directly to order.

UMI

**A Bell & Howell Information Company
300 North Zeeb Road, Ann Arbor MI 48106-1346 USA
313/761-4700 800/521-0600**

University of Alberta

Numerical Model of Electrokinetic Flow in Capillary Channels

by

Liangang Hu ©

A thesis

Submitted to the Faculty of Graduate Studies and Research
in partial fulfilment of the requirements for the degree of
Master of Science

Department of Chemical and Materials Engineering
Edmonton, Alberta

Spring, 1997



National Library
of Canada

Acquisitions and
Bibliographic Services

395 Wellington Street
Ottawa ON K1A 0N4
Canada

Bibliothèque nationale
du Canada

Acquisitions et
services bibliographiques

395, rue Wellington
Ottawa ON K1A 0N4
Canada

Your file *Votre référence*

Our file *Notre référence*

The author has granted a non-exclusive licence allowing the National Library of Canada to reproduce, loan, distribute or sell copies of his/her thesis by any means and in any form or format, making this thesis available to interested persons.

The author retains ownership of the copyright in his/her thesis. Neither the thesis nor substantial extracts from it may be printed or otherwise reproduced with the author's permission.

L'auteur a accordé une licence non exclusive permettant à la Bibliothèque nationale du Canada de reproduire, prêter, distribuer ou vendre des copies de sa thèse de quelque manière et sous quelque forme que ce soit pour mettre des exemplaires de cette thèse à la disposition des personnes intéressées.

L'auteur conserve la propriété du droit d'auteur qui protège sa thèse. Ni la thèse ni des extraits substantiels de celle-ci ne doivent être imprimés ou autrement reproduits sans son autorisation.

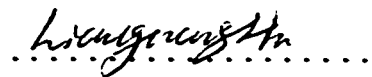
0-612-21173-8

University of Alberta
Library Release Form

Name of Author: **Lianguang Hu**
Title of Thesis: **Numerical Model of Electrokinetic Flow in Capillary
Channels**
Degree: **Master of Science**
Year this degree granted: **1997**

Permission is hereby granted to **The University of Alberta Library** to reproduce single copies of this thesis and to lend or sell such copies for private, scholarly, or scientific research purposes only.

The author reserves all other publication and other rights in association with the copyright in the thesis, and except as hereinbefore provided, neither the thesis nor any substantial portion thereof may be printed or otherwise reproduced in any material form whatever without the author's prior written permission.


(Student's signature)

Lianguang Hu
#205 , 9710-82 Avenue
Edmonton, Alberta, T6E 1Y5

Date: Jan 6/97

University of Alberta

Faculty of Graduate of Studies and Research

The undersigned certify that they have read, and recommend to the Faculty of Graduate Studies and Research for acceptance, a thesis entitled **Numerical Model of Electrokinetic Flow in Capillary Channels** submitted by **Lianguang Hu** in partial fulfilment of the requirements for the degree of **Master of Science**

J. H. Masliyah

(Co-supervisor)

D. J. Harrison

(Co-supervisor)

R. P. Batycky

J. D. Dale

Date Jan 2/97

Abstract

A numerical study is presented for the steady electrokinetic flows in both single straight capillary channels and in intersecting channels with a T-shaped configuration. The electric potential and space charge density distribution along the capillary are obtained numerically by solving the non-linear Poisson-Boltzman equation for arbitrary electrokinetic length(κa) and arbitrary surface potential. The velocity and pressure profiles are obtained by solving a modified Navier-Stokes equation using a primitive variable algorithm.

Initially the electroosmotic flow in a single straight channel is studied. The flow behaviour is investigated by changing the surface potential on part of capillary channel and by use of auxiliary pumping capillary. The pressure distribution induced by the difference in electroosmotic flow along the channel is obtained. The velocity profiles are shown to be a combination of an electroosmotic flow and a pressure driven flow.

A study of flow in the T-shaped intersecting channels showed that the induced pressure within the channel is an important factor that affects fluid leakage out of the side channel. The parameters which affect leakage from a floating channel are investigated. The results showed that the flow in each channel can be controlled by applying a potential at each reservoir connected to the end of a channel. The dependence of flow on the surface zeta potential of each channel is studied.

Acknowledgement

The author would like to express his sincere appreciation to Dr. J. H. Masliyah and Dr. D. J. Harrison who supervised the preparation of this thesis. Their thoughtful guidance, encouragement, and advice are highly appreciated.

The author owes much appreciation to Dr. S. Liu who gave the author advice and suggestions on the mathematical simulation. The author also acknowledges the Department of Chemical and Materials Engineering for the generous award of Teaching Assistantship and for its excellent computing facilities.

Finally, the author is most thankful to his wife and family for their immeasurable emotional support and encouragement during his study at the University of Alberta.

Contents

Chapter 1	Introduction	1
1.1	Concept of Capillary Zone Electrophoresis	1
1.2	Electrophoresis in Glass Chip	3
1.3	Mechanism of Electroosmotic Flow	5
1.4	Outline of Thesis	7
Chapter 2	Physical Phenomena and Mathematical Formulation	8
2.1	Definition of the Problem and Assumptions	8
2.2	Electrical Potential Distribution due to Electric Double Layer	10
2.3	External Electric Potential Distribution due to Electric Field	14
2.3.1	Laplacian Equation	14
2.3.2	Kirchhoff's Rule	15
2.4	Electrokinetic Transport Equations	16
2.5	Solution to the 1-D Poisson-Boltzmann Equation	19
2.5.1	Debye-Hückel Approximation and Analytical Solutions	19
2.5.2	Numerical Solution to the 1-D P-B Equation	20
2.6	Numerical Solution to Electric Potentials for the T-shaped Channels ..	22
2.6.1	Electric Potential due to Debye Double Layer	22
2.6.2	Electric Potential due to External Electric Field	22
Chapter 3	Numerical Implementation	32
3.1	Introduction	32
3.2	Finite Difference Equations	33
3.2.1	Grid Definition	33
3.2.2	Discretization of the Momentum Equation	34

3.2.3 Treatment of Continuity Equation	36
3.2.4 Boundary Conditions	38
3.3 Solution Procedure	38
3.3.1 Under-relaxation Factor	38
3.3.2 Solution Procedure	39
3.3.3 Convergence Criteria	39
3.4 Test of Program	40
 Chapter 4: Electroosmotic Flow in Straight Channel	47
4.1 Introduction	47
4.2 Fully Developed and Developing Electroosmotic Flow in Capillary Channel	48
4.2.1 Fully-developed Electroosmotic Flow in Capillary Channel	48
4.2.2 Developing Electroosmotic Flow	50
4.3 Controlling of Electroosmotic Flow in Capillary Electrophoresis	55
4.3.1 Introduction	55
4.3.2 Effect of Surface Potential	56
4.3.3 Control of Flow by Changing ζ Potential in a Portion of Capillary Wall	56
4.3.4 Control of Flow by Auxiliary Electroosmotic Pumping	62
 Chapter 5 Electroosmotic Flow in T-shaped Capillary Channel	66
5.1 Introduction	66
5.2 Fluid Leakage from the Floating Side Channel	67
5.2.1 Effect of the Channel Length on the Leakage	67
5.2.2 Effect of the Side Channel Location	74
5.2.3 Effect of the Side Channel Length	74
5.2.4 Effect of the Surface Potential and the Electric Field	80
5.2.5 Effect of the Floating Channel Length When Flow is Around a Corner	80

5.3 Flow in each Channel with an Electric Potential Applied on each Reservoir	86
5.3.1 Control of Leakage by Use of a Potential	86
5.3.2 Effect of the Surface Potential in the Channels	87
Chapter 6 Conclusions and Recommendations	106
References	109

List of Figures

1.1	Schematic of a system for CE	2
1.2	Device layout (COCE) with reservoirs and channel indicated	3
1.3	Photomicrograph of leakage	4
2.1	The arrangement of coordinates and boundary condition for electric potential	9
2.2	Equivalent circuit for the device of figure 1.2	15
2.3	The nodal arrangement for one dimensional problem	20
2.4	Dimensionless transverse electrostatic potential distribution across a channel	24
2.5	Dimensionless transverse electrostatic potential distribution across a channel	25
2.6	Dimensionless transverse electrostatic potential distribution across a channel	26
2.7	Dimensionless transverse electrostatic potential distribution across a channel	27
2.8	Dimensionless electric potential distribution in the main channel	28
2.9	Dimensionless electric potential distribution in the side channel	29
2.10	External potential distribution along the main channel and side channel	30
2.11	External electric potential distribution channel and side channel	31
3.1	Staggered grid	33
3.2	Geometry and coordinate system for developing duct flow	40
3.3	Velocity profile development between parallel plates for creeping flow	42
3.4	Poiseuille creeping flow for axial velocity development between parallel plates	43
3.5	Development of axial velocity in Poiseuille creeping flow	44
3.6	Transverse velocity profile development between parallel plates	45
3.7	Average pressure variation along a two-dimensional channel	46
4.1	Electroosmotic flow in capillary channel	47
4.2	Comparison of velocity profile for different κa	51
4.3	Variation of dimensionless velocity with κa	52

4.4	Pressure profile along centerline of channel	53
4.5	Developed velocity profile	54
4.6	Dimensionless average velocity versus ζ potential	55
4.7	Schematic of the apparatus used to control electroosmotic flow by radial voltage	56
4.8	Velocity and profile in capillary channel	58
4.9	Dimensionless average velocity versus the fraction of imperfect wall	59
4.10	Variation of dimensionless average velocity with ζ'	60
4.11	Velocity and pressure profile in capillary channel	61
4.12	Auxiliary electroosmotic pumping scheme	62
4.13	Velocity and pressure profile in capillary	64
4.14	Dimensionless average velocity versus the electric potential	65
5.1	The schematic of connecting channels	67
5.2	Variation of dimensionless velocity in the channels with the length of channel	69
5.3	Pressure distribution along the center line of main channel	70
5.4	Electric potential distributions in the channels	71
5.5	Velocity profile in main channel and side channel	72
5.6	Streamline at intersection	73
5.7	Pressure profile along center line of main channel	76
5.8	Dimensionless average velocity in each channel versus location of side channel	77
5.9	Dimensionless average velocity in each channel versus side channel length	78
5.10	Pressure profile along center line of the main channel	79
5.11	Dimensionless average velocity versus ζ potential	81
5.12	Dimensionless average velocity versus electric potential gradient	82
5.13	Dimensionless average velocity versus the floating channel length	83
5.14	Velocity profile in each channel	84
5.15	Streamline at intersection	85
5.16	Variation of dimensionless velocity with side potential	88
5.17	Electric potential distributions in the channels	89
5.18	Pressure profile along the center line of the main channel	90
5.19	Variation of average velocity in the side channel with ζ'	92

5.20	Variation of average velocity in the main channel with ζ'	93
5.21	Variation of velocity ratio in the side channel with ζ'	94
5.22	Variation of velocity ratio in the main channel with ζ'	95
5.23	Pressure profile along centerline of the main channel	96
5.24	Velocity profile at different sections	97
5.25	Streamline in the channels	98
5.26	Variation of dimensionless average velocity with ζ	99
5.27	Variation of velocity ratio in the channels with ζ	100
5.28	Pressure profile along the centerline of the main channel	101
5.29	Velocity profile at different sections	102
5.30	Streamline in the channels	103

Nomenclature

a	half width of capillary channel, (m)
au	coefficient in discretization equation for u
av	coefficient in discretization equation for v
ap	coefficient in discretization equation for p
b	constant term in discretization equation
c	solute concentration, (mol/m ³)
e	elementary charge, (C)
E₁	electric field strength in the left channel, $E_1=(\Phi_1-\Phi_J)/L_1$
E₂	electric field strength in the right channel, $E_2=(\Phi_J-\Phi_2)/L_2$
E_s	electric field strength in the side channel, $E_s=(\Phi_3-\Phi_J)/L_s$
E_x	electric field in axial direction, $-d\Phi/dX$
f	general variable defined by equation (2.58)
I	electric current, (A)
k	Boltzmann constant, (J/K)
L	dimensionless length of channel
L_m	dimensionless main channel length
L_s	dimensionless side channel length
L₁, L₂, L₃	length of left, right and side channel, respectively
n₊	ionic number concentration of the cations, (m ⁻³)
n₋	ionic number concentration of the anions, (m ⁻³)
n_∞	ionic number concentration in the bulk solution, (m ⁻³)
p	fluid pressure, (Pa)
p_x	negative pressure gradient, $-dp/dx$, (Pa/m)
P	dimensionless pressure
P_x	dimensionless negative pressure gradient, $-dP/dX$
R	electric resistance, (Ω)
S	source term in discretization equation

s	stream function, (m^2/s)
T	absolute temperature, (K)
u	fluid velocity in x direction, (m/s)
u_e	electroosmotic flow velocity according Helmholtz - Smoluchowski equation m/s
U	dimensionless velocity in x direction
U_{in}	dimensionless average velocity in the left channel
$U_{e,in}$	dimensionless average electroosmotic velocity in the left channel
U_{out}	dimensionless average velocity in the right channel
$U_{e,out}$	dimensionless average electroosmotic velocity in the right channel
$\langle u \rangle$	characteristic velocity, (m/s)
U'	velocity correction
U^*	axial velocity based on guessed pressure P^*
v	fluid velocity in y direction, (m/s)
V	dimensionless velocity in y direction
V_{in}	dimensionless average velocity in the side channel
$V_{e,in}$	dimensionless average electroosmotic velocity in the side channel
x	coordinates in x direction, (m)
X	dimensionless x coordinates
y	coordinates in y direction, (m)
Y	dimensionless y coordinates
z	absolute value of a ($z:z$) electrolyte solution valency

Greek

α	relaxation factor
ε	dielectric constant, dimensionless
ε_0	permittivity of vacuum, (C/m V)
ζ	dimensionless surface potential
θ	relaxation factor
κ	inverse Debye length, (m^{-1})
μ	fluid viscosity , (Pa s)

ρ	free charge density, (C/m ³)
Φ	dimensionless external electric potential
Φ_1	dimensionless external electric potential at left reservoir
Φ_2	dimensionless external electric potential at right reservoir
Φ_3	dimensionless external electric potential at side reservoir
Φ_j	dimensionless external electric potential at intersection
ϕ	external potential, (V)
ϕ_x	$\phi_x = -d\phi/dx$, (V/m)
Ψ	dimensionless potential due to electric double layer
Ψ_s	dimensionless surface potential
ψ	potential due to electric double layer, (V)
ψ_s	surface potential, (V)

Subscripts

E,W,S,N	neighbour grid point on the east, west, south, and north, respectively
e,w,s,n	control volume face on the east, west, south, and north, respectively
in	inlet
m	the main channel
nb	general neighbour grid point
s	surface or the side channel
u	velocity in x direction
v	velocity in y direction
p	pressure
1, 2, 3	left, right and side channel, respectively

Superscripts

'	correction
*	previous-iteration value of a variable

Chapter 1

Introduction

1.1 Concept of Capillary Zone Electrophoresis

Over the past decade, capillary electrophoresis(CE) has emerged as a very powerful alternative for the separation of charged species present in an aqueous medium. Capillary electrophoresis is a modern analytical technique which permits rapid and effective separation of charged ionic species present in small amounts. The most attractive features of this relatively new separation technique include high separation efficiencies, high resolving power, high speed, full automation and applicability to a variety of biologically important molecules. CE has been applied to chemical, biochemical and pharmaceutical analyses. Some examples are the separation of proteins, Amino acids, peptide, tryptic mapping, DNA sequencing, Serum analysis, analysis of neurotransmitters in single cells, determination of organic and inorganic ions, and chiral separations. The separation in CE is based on the difference in electrophoretic mobilities resulting in different velocities of migration of the different species in an electrophoretic buffer solution contained in the capillary. The separation mechanism is mainly based on differences in solute size and charge at a given pH[1,2]. Figure 1.1 shows the schematic of a system for CE. In capillary electrophoresis, a background electrolyte with adequate buffering properties forms a conducting medium along the migration path. Under the

influence of electric field applied tangentially to the capillary surface, two mechanisms of electrokinetic phenomena occur[3,4], i.e. electrophoresis and electroosmosis. Electrophoresis is the migration of charged species relative to the bulk solution under the influence of an electric force exerted by an electric field. The migration velocity is a characteristic of the molecular charge, size and shape. Concomitant to the electrophoretic migration, a bulk flow of solution is induced by the electric field. This migration, called electroosmosis, is dependent on the characteristics of the capillary surface as well as the composition of the buffer. It is the electroosmotic flow (EOF) that makes the full automation of capillary electrophoresis possible.

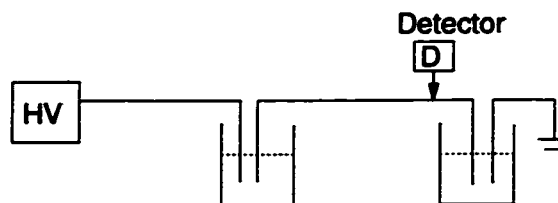


Figure 1.1 Schematic of a system for CE

The electroosmotic flow in un-coated fused-silica capillary having a negatively charged surface is usually significantly greater than the electrophoretic flow of individual ions. Consequently, both cations and anions can be swept to the cathode. Cations are attracted toward the cathode and their speed is augmented by the EOF. Anions, although electrophoretically attracted toward the anode, are swept towards the cathode with the bulk flow of electrophoretic medium. Since different ions have different mobilities, the electrophoretic separation of different charged species is thus achieved.

Electroosmotic flow plays an important role in capillary electrophoresis. It affects the residence time in the capillary and therefore, may affect both efficiency and resolution indirectly[5]. Therefore, the control of EOF may have a large effect in improving resolution and efficiency and is one of the most important aspects of controlling reproducibility in CE[6]. Several strategies have been suggested to control electroosmotic flow in recent years. These include derivatizing the inner surface of the capillary[7], altering the buffer pH[8-9], applying radial voltage to the capillary wall [10-14], and auxiliary capillary pumping [15]. The experimental results due to[10-15] have shown the effect of applied radial voltage and auxiliary pumping on the EOF. However, the velocity profile along capillary is not well understood.

When the surface potential of the wall of a segment of a channel is different from the other part of the capillary, the electroosmotic flow in both segments of the capillary will be different. One segment can either hinder or augment the other and the velocity profiles in both parts of the channel will no longer be plug-like. When electric potential gradients are different in two capillary segments that are joined together, the flow within one segment will also influence the other. The flow mechanism of the above two physical situations can be modeled by varying the surface potential within a given portion of the capillary walls and varying the electric field along the capillary. A numerical model is developed to predict the electroosmotic flow and velocity profile for the above two cases.

1.2 Electrophoresis in a Glass Chip

It has been successfully demonstrated that an electroosmotic sample injection system and electrophoretic separation can be integrated together on a planar glass chip[16-22]. By micromachining a complex manifold of flow channels in a planar substrate, one can fabricate a network of capillaries capable of sample injection, pretreatment, and separation. Instead of using a pressure difference to induce the flow, electrokinetic phenomena have been employed. The use of electroosmotic pumping offers an additional advantage as compared to micromachined pumps and valves in that there are no moving parts, and

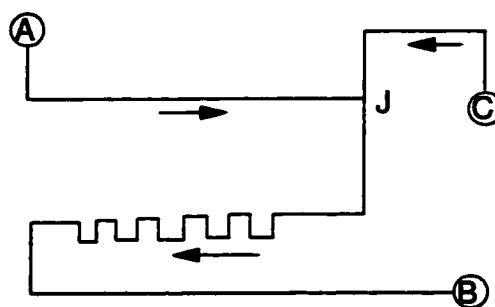


Figure 1.2 Device layout with reservoir and channel labels indicated [17]

reliable performance has been achieved with this technology. To understand what factors play a role in the performance of such a device, it is useful to consider here the modes of operation. Figure 1.2 shows a channel layout of a simple device for sample injection and separation. It consists of reservoirs, A, B and C, at the heads of three interconnected capillary channels. As conceived, the application of a voltage between any two reservoirs

will cause electroosmotic pumping of fluid along those channel segments between the reservoirs. Valveless switching of fluid flow between channels should be achieved by switching the voltages applied to each channel. For example, voltage applied between A (sample electrolyte) and B (separation, waste) would draw sample solution into channel AB and past the intersection region J. Subsequent application of a voltage between C (carrier electrolyte) and B would then drive a small plug of sample at J along separation channel JB, resulting in electrophoretic separation of the components in the sample plug.

Compared to conventional systems, such devices can reduce solvent and sample consumption or decrease analysis time because of their decreased dimensions. Very rapid separations (< 5 s) of fluorescently labelled amino acid mixtures can be effected within such devices[20]. The separation efficiency has been improved by increasing the voltage range and improving the detector. More challenging and complex samples may be separated with compact CE devices[17].

As described above, fluid flow in a manifold of intersecting channels can be directed in the desired direction by the appropriate application of potentials to various channels within the manifold. This valveless control of fluid flow is subject to leakage between the channels at their intersection region. When the potential of a side channel is left uncontrolled (hereinafter called floating), solution may leak into the active main channel. A photomicrograph of a device taken while two of the three channels were actively under potential control is shown in Figure 1.3[16]. The device was flooded with 488-nm light while positioned on an Olympus BH-2 microscope stage (20:1 magnification). The applied potential drove the buffer solution along the channel CB,

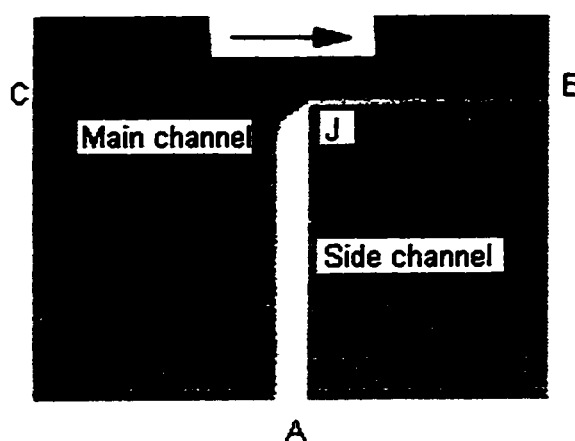


Figure 1.3 Photomicrograph of a device with 1 kV/cm applied along the horizontal channel, while the side channel is left floating [16]

while the side channel AJ was filled with a fluorescent dye and left floating. There is a convective flow of the dye out of the side channel. This indicated that the electroosmotic flow along the main channel caused liquid leakage out of the side channel. It has been shown that the leakage can vary greatly within different devices, from 1% up to 30% in some layouts. The magnitude of the effect depends on the applied potentials, and the dimensions of the connecting channels. As these leakage effects are of great importance in determining the separation efficiency of a CE device, the flow behaviour within these intersecting channels needs to be better understood.

The experimental study[16] clearly shows that the leakage from a side channel to a main channel is mainly due to hydrodynamic effects. The flow out of the floating side channel into the active channel in which electroosmotic flow is induced under the influence of an electric field may be due to the viscous effect or static pressure difference between the reservoir and intersection. Some qualitative studies have been carried out trying to understand the factors which influence the flow behaviour in the channels[18]. It is desirable, however, to develop a more quantitative description of the influence of the resistance to flow in intersecting channels, and to study the phenomena such as leakage or mixing at channel intersections[17]. The objective of the present work is to attempt to establish a mathematical model to predict the flow behaviour in intersecting channels.

1.3 The Mechanism of Electroosmotic Flow

Silica surfaces are characterized by the presence of several types of silanol groups (SiOH), which are weakly acidic in character. In contact with an aqueous solution, some of the silanol groups are ionized and cause the surface to be negatively charged and an electric double layer develops within it. The interface between the fused silica wall and the bulk buffer inside the capillary has been studied extensively [3,23]. The structure of this interface may be divided into three parts : (1) the silica surface (2) the immobile layer (also called the Stern layer or inner Helmholtz plane and (3) the diffuse layer [12]. The immobile layer is modeled as tightly bound counterions and the diffuse layer as

solvated, loosely held counterions.

The thickness of the diffuse electric double layer is of order of the Debye length κ^{-1} . When an electric field is imposed tangentially to a surface, the electric forces act upon the spatial distribution of the ions within the diffuse layer causing unilateral movement of the ions toward the oppositely charged electrode. During their migration, these ions drag the surrounding solvent molecules, resulting in an overall movement of the solution. This bulk movement of the solution relative to the stationary charged surface is referred to as electroosmotic flow. The electric double layer or electrokinetic radius κa and zeta potential determine the flow velocity profile when an electric potential is applied across a capillary.

The governing equations of the electrokinetic phenomena under the influence of applied pressure and potential gradients across capillaries filled with an electrolyte are well known [3], The basic relationships involved were formulated by Smoluchowski[4]. However, Smoluchowski's model suffered from a restriction due to the assumption that the electrokinetic radius κa was large, that is, the double layer thickness was small compared with the capillary radius (a). Rice and Whitehead [24] calculated analytically the correction factors that must be applied to Smoluchowski's results for narrow cylindrical capillaries having arbitrary values of κa ($0 < \kappa a < \infty$). However, their theory itself is subject to a severe restriction that the surface zeta potential be sufficiently low to permit the use of the Debye-Hückel approximation, effectively limiting the application of their prediction to surface potentials less than 25 mV for a monovalent electrolyte. Levine et al. [25] extended the Rice-Whitehead theory to higher zeta potentials by developing analytical approximations to the solution of the nonlinear Poisson-Boltzmann equation within the capillary. However, their analysis is confined to monovalent electrolyte. The previous published solutions have been to a large extent analytical and are limited in their applicability.

This work attempts to provide some insights into the electroosmotic flow and hydrodynamic flow phenomena within intersecting channels. The purpose of this study is not to present an analysis of any particular CE device. Instead, an attempt will be made to model the flow in general terms and thereby to predict the flow rate and velocity

profile in each channel and explore the factors which control flow within intersecting channels. To this end, the analysis will focus on the numerical solution of the governing equations for steady electrokinetic flow in capillary channels. The different factors that affect the electrokinetic flow will be discussed.

1.4 Outline of the Thesis

In chapter 2, the problem to be investigated and the solution strategies are described. The governing differential equations and the boundary conditions are stated. Numerical solutions for the electrical potential both due to the electric double layer and to an externally applied field are obtained. Comparisons of the numerical solutions with the analytical solutions are made where possible.

The numerical implementation of the problem is described in chapter 3. A numerical algorithm based on Liu-Masliyah numerical separation method and SIMPLE-C algorithm are briefly described. The accuracy of the developed computer code is tested by solving the creeping flow and by comparing the solutions with the literature.

The electroosmotic flow in a straight channel and the control of flow are considered in chapter 4. Velocity profiles are obtained and are used to illustrate the factors which affect the flow.

Chapter 5 deals with the electrokinetic flow in intersecting capillary channels(T-shaped channels). A systematic study of the effects of the main parameters on the flow and leakage at channels intersection is conducted.

Chapter 6 gives the conclusions and recommendations.

Chapter 2

Physical Phenomena and Mathematical Formulation

2.1 Definition of the Problem and Assumptions

The use of a planar glass chip fabricated by photolithography for capillary electrophoresis has been successfully demonstrated[16-22]. Both electrophoretic and sample injection systems have been integrated together using microlithographic technology known as micromachining. Figure 1.2 shows the layout of a typical glass device that consists of three capillary channels intersecting at right angle to form a T-junction. In the study of CE on a chip, the channels were 10 μm deep and 30 μm wide. By alternating the electrical potential in the three reservoirs, it is possible to control the electroosmotic flow in each channel.

The problem is to predict the steady electroosmotic flow in the three channels under different conditions, with the potential at one of the reservoirs either fixed or left uncontrolled while an electric potential is applied across the remaining two reservoirs. It has been shown that electroosmotic flow in such capillaries requires a few hundred microseconds to develop after the potential has been applied to a capillary[26]. In this analysis the electroosmotic flow delay is not taken into consideration. Due to the high thermal mass and conductivity of the glass chips, experimental results showed that an electric field up to 2500 V/cm with a power dissipation of 2.3 W/m did not result in Joule

heating effects[19]. Therefore, thermal effects will not be considered here. The study of electroosmotic flow in a capillary channel then consists of solving the Poisson-Boltzmann, mass conservation and the Navier-Stokes transport equations coupled with the Nernst-Planck equation. The electrolyte solution is idealized as a fluid with a constant bulk concentration, n_∞ , viscosity, μ , density, ρ , and dielectric constant, ϵ . The use of the Nernst-Planck equation can be avoided once the bulk ionic concentration is taken as constant along the channel.

Following Henry's [27] classical analysis of electrokinetic flow, it is assumed that the total electrostatic potential can be expressed as a linear superposition of the potential due to the electrical double layer (ψ) which would exist in the absence of the applied electric field and the potential that arises from the applied external field (ϕ). Figure 2.1 shows the coordinates of the T-shaped channels for which we ultimately will obtain the total potential. It is assumed that $\phi_{\text{total}} = \phi + \psi$. ϕ_1 , ϕ_2 and ϕ_3 are electric potentials applied at each reservoir. ψ_s and ψ'_s are the surface potentials in the main and side channel respectively. According to the Guoy-Chapman model, the surface potential is identicalized as zeta potential when the ions are taken as point charges.

Assuming equilibrium, the Poisson - Boltzmann equation for Debye double layer and the Laplacian equation for the external electric potential distribution can be decoupled from the transport

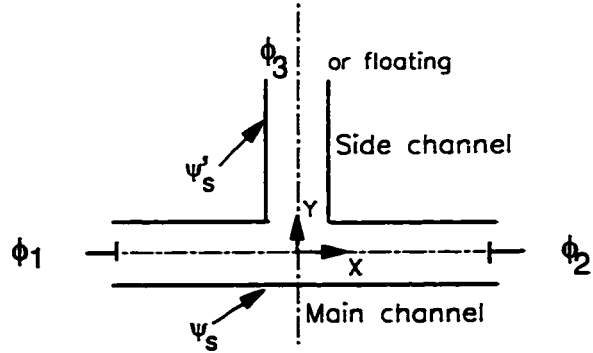


Figure 2.1 Arrangement of coordinates and boundary conditions for electric potential solution.

equation. The electrical potential distribution due to the Debye double layer and the electric field are obtained first, and the velocity and pressure profile can be obtained by solving the Navier-Stokes equation. The numerical method used to solve the Poisson-Boltzmann and the Laplacian equation is straight forward, Therefore, some results of the electric potential distributions due to the electric Debye layer and an external electric field

will be given in this chapter. A numerical implementation to the transport equation will be described in Chapter 3.

2.2 Electric Potential Distribution due to Electric Double Layer

The electric potential distribution within the diffuse electric double layer is given by the Poisson equation as

$$\nabla^2 \psi = -\frac{\rho}{\epsilon \epsilon_0} \quad (2.1)$$

For a 2-D problem for the case shown in figure 2.1, we have,

$$\frac{\partial^2 \psi}{\partial x^2} + \frac{\partial^2 \psi}{\partial y^2} = -\frac{\rho}{\epsilon \epsilon_0} \quad (2.2)$$

The charge density is given by

$$\rho = \sum_{i=1}^N n_i z_i e \quad (2.3)$$

Where n_i is the ionic number concentration of the i th species, m^{-3}

z_i is the valence of the i th species

e is the fundamental charge, $1.602 \times 10^{-19} C$

N is the number of ionic species in the electrolyte solution.

ϵ is the dielectric constant of the electrolyte solution that is assumed to be a constant.

ϵ_0 is the permittivity of vacuum, $\epsilon_0 = 8.85 \times 10^{-12} C/Vm$.

The assumption of thermal equilibrium leads to the Boltzmann's equation, that is

$$n_i = n_{i\infty} \exp\left[-\frac{z_i e \psi}{kT}\right] \quad (2.4)$$

Where $n_{i\infty}$ is the ionic number concentration at the neutral state where $\psi = 0$, k is the Boltzmann constant, and T is the absolute temperature. Combining equations. (2.3) and

(2.4) leads to

$$\rho = \sum_{i=1}^N z_i n_{i\infty} e \exp\left[-\frac{z_i e \psi}{kT}\right] \quad (2.5)$$

Substitution of equation (2.5) into the Poisson equation (2.2) leads to the well-known Poisson-Boltzmann(PB) equation for a 2-D configuration,

$$\frac{\partial \psi^2}{\partial x^2} + \frac{\partial \psi^2}{\partial y^2} = -\frac{1}{\epsilon \epsilon_0} \sum_{i=1}^N n_{i\infty} z_i e \exp\left[-\frac{z_i e \psi}{kT}\right] \quad (2.6)$$

For a symmetric electrolyte solute (z:z), equation (2.6) can then be written as

$$\frac{\partial \psi^2}{\partial x^2} + \frac{\partial \psi^2}{\partial y^2} = \frac{2 n_{\infty} z e}{\epsilon \epsilon_0} \sinh\left[\frac{z e \psi}{kT}\right] \quad (2.7)$$

The boundary conditions for equation (2.7) includes the surface potential at the walls and the potential distributions at three channel ends. At the walls of the main channel, $\psi = \psi_s$, ψ_s is the surface potential of the main channel wall; at the walls of the side channel, $\psi = \psi'_s$, ψ'_s is the surface potential of the side channel wall. When electrolytes in both the main and side channel are the same, ψ_s will be equal to ψ'_s . The boundary conditions for the potential distributions at three channel ends are concerned with three one-dimensional equations. For the left and right ends (for $x = -l_1$, and $x = l_2$), the potential is a function of y , which is given by the following equations,

$$\frac{d^2 \psi}{dy^2} = \frac{2 n_{\infty} z e}{\epsilon \epsilon_0} \sinh\left(\frac{z e \psi}{kT}\right) \quad (2.8)$$

$$\psi = \psi_s \quad \text{at } y = a \quad (\text{channel wall}) \quad (2.9)$$

$$\psi = \psi_s \text{ at } y = -a \quad (\text{channel wall}) \quad (2.10)$$

For the side channel end ($y = l_s$), the potential is a function of x ,

$$\frac{d^2\psi}{dx^2} = \frac{2n_\infty z e}{\epsilon \epsilon_0} \sinh\left(\frac{ze\psi}{kT}\right) \quad (2.11)$$

$$\psi = \psi_s \text{ at } x = a \quad (\text{channel wall}) \quad (2.12)$$

$$\psi = \psi_s \text{ at } x = -a \quad (\text{channel wall}) \quad (2.13)$$

Equations (2.7) through (2.13) form a set of equations and boundary conditions to solve the electric potential due to the electrical double layer. The following dimensionless parameters are introduced,

and they lead to normalized equations. Equation (2.7) becomes

$$\frac{\partial^2 \Psi}{\partial X^2} + \frac{\partial^2 \Psi}{\partial Y^2} = (\kappa a)^2 \sinh \Psi \quad (2.14)$$

where κ is the reciprocal of Debye double layer thickness defined by

$$\kappa = \left[\frac{2n_\infty z^2 e^2}{\epsilon \epsilon_0 kT} \right]^{1/2} \quad (2.15)$$

and the normalized boundary conditions are given by,

(a) The main channel wall conditions

$$\Psi = \zeta \quad \begin{cases} \text{at } Y = -1 & \text{for all } X, \\ Y = 1 & \text{for } X \leq -1 \text{ and } X \geq 1 \end{cases} \quad (2.16)$$

(b) The side channel wall conditions

$$\Psi = \zeta' \quad \text{at } X = \pm 1 \quad \text{for } Y \geq 1 \quad (2.17)$$

(c) The boundary conditions of the ends of the main channel (for $X = -L_1$ and $X = L_2$), equations(2.8) through (2.10) become

$$\frac{d^2\Psi}{dY^2} = (\kappa a)^2 \sinh\Psi \quad (2.18)$$

$$\Psi = \zeta \quad \text{at } Y = 1 \quad (2.19)$$

$$\Psi = \zeta \quad \text{at } Y = -1 \quad (2.20)$$

(d) The side channel end conditions (for $Y=L_s$), equations(2.11) through (2.13) become

$$\frac{d^2\Psi}{dX^2} = (\kappa a)^2 \sinh\Psi \quad (2.21)$$

$$\Psi = \zeta' \quad \text{at } X = 1 \quad (2.22)$$

$$\Psi = \zeta' \quad \text{at } X = -1 \quad (2.23)$$

The electrical potential distribution due to the Debye double layer can be obtained by solving equation (2.15) with above boundary conditions (a) to (d).

2.3 Electrical Potential Distribution due to External Field

2.3.1 Laplacian Equation

Now consider the T-shaped channel (figure 2.1) with a charge-free dielectric in it. The electric potential associated with the external (applied) electric field ϕ , satisfies the Laplacian equation,

$$\nabla^2 \phi = 0 \quad (2.24)$$

for 2-D the Laplacian equation can be written as,

$$\frac{\partial^2 \phi}{\partial x^2} + \frac{\partial^2 \phi}{\partial y^2} = 0 \quad (2.25)$$

Similar dimensionless parameters are introduced as follows

$$\Phi = \frac{ze\phi}{kT}, \quad X = x/a, \quad Y = y/a \quad (2.26)$$

The dimensionless Laplacian equation becomes

$$\frac{\partial^2 \Phi}{\partial X^2} + \frac{\partial^2 \Phi}{\partial Y^2} = 0 \quad (2.27)$$

The boundary conditions are,

(a) wall and floating conditions

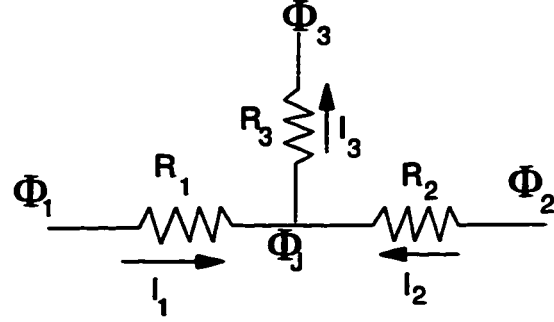
$$\frac{\partial \Phi}{\partial Y} = 0 \quad \text{or} \quad \frac{\partial \Phi}{\partial X} = 0 \quad (2.28)$$

(b) end conditions

$$\left. \begin{aligned} \Phi &= \Phi_1 \quad \text{at } X = -L_1 \\ \Phi &= \Phi_2 \quad \text{at } X = L_2 \\ \Phi &= \Phi_3 \quad \text{at } Y = L_s \end{aligned} \right\} \quad (2.29)$$

2.3.2 Kirchhoff's Rule

If the potential variation across the channel at intersection is not taken into account, the three intersecting channels with potentials applied to the reservoirs can be modelled as a simple network of three resistors, as illustrated in figure



2.2. With three potential sources connected to the channel ends, the current in each channel and the potential at the intersection are readily expressed using Kirchhoff rules,

Figure 2.2 Equivalent circuit for the device of figure 1.2 [17].

$$I_3 = (\Phi_J - \Phi_3) / R_3 \quad (2.30)$$

$$I_1 = (\Phi_1 - \Phi_J) / R_1 \quad (2.32)$$

$$I_2 = (\Phi_2 - \Phi_J) / R_2 \quad (2.33)$$

$$I_3 = I_1 + I_2 \quad (2.34)$$

The assumed direction of electric currents I_1 , I_2 and I_3 are shown in figure 2.2. The sign of the electric current depends on the values of the potentials. The potential at the intersection can be obtained by solving the above equations, leading to

$$\Phi_J = \frac{\Phi_1 R_2 R_3 + \Phi_2 R_1 R_3 + \Phi_3 R_1 R_2}{R_1 R_2 + R_1 R_3 + R_2 R_3} \quad (2.35)$$

It has been shown that the resistances are proportional to the equivalent channel length [31]. Consequently, Kirchhoff rule will be used to obtain the initial guess for the numerical solution.

2.4 Electrokinetic Transport Equations

Consider the steady flow of an incompressible aqueous solution of a symmetrical electrolyte through the T-shaped channel (figure 2.1). In the presence of the electric field the equation of motion for creeping flow through the channel is given by the modified Navier-Stokes equation:

$$\vec{\nabla} p = \mu \nabla^2 \mathbf{u} - \rho \vec{\nabla}(\psi + \phi) \quad (2.36)$$

and the continuity equation,

$$\vec{\nabla} \cdot \mathbf{u} = 0 \quad (2.37)$$

Where \mathbf{u} is the velocity vector, μ is the electrolyte viscosity, and p is the pressure. The free charge density, ρ , for symmetrical electrolyte is given by,

$$\rho = -2 n_{\infty} z e \sinh\left(\frac{ze\psi}{kT}\right) \quad (2.38)$$

The following dimensionless parameters are introduced :

$$\Psi = \frac{ze\psi}{kT}, \quad \Phi = \frac{ze\phi}{kT}, \quad X = \frac{x}{a}, \quad Y = \frac{y}{a} \quad (2.39)$$

$$U = \frac{u}{\langle u \rangle}, \quad V = \frac{v}{\langle u \rangle}, \quad P = \frac{ap}{\mu \langle u \rangle} \quad (2.40)$$

where $\langle u \rangle$ is a characteristic velocity defined by

$$\langle u \rangle = \frac{2 n_{\infty} a k T}{\mu} \quad (2.41)$$

The normalized transport equation becomes

$$\frac{\partial P}{\partial X} = \frac{\partial^2 U}{\partial X^2} + \frac{\partial^2 U}{\partial Y^2} + \sinh \Psi \frac{\partial(\Psi + \Phi)}{\partial X} \quad (2.42)$$

$$\frac{\partial P}{\partial Y} = \frac{\partial^2 V}{\partial X^2} + \frac{\partial^2 V}{\partial Y^2} + \sinh \Psi \frac{\partial(\Psi + \Phi)}{\partial Y} \quad (2.43)$$

$$\frac{\partial U}{\partial X} + \frac{\partial V}{\partial Y} = 0 \quad (2.44)$$

Here Ψ and Φ are given in 2.2 and 2.3, respectively. The above governing partial differential equations for motion are subject to the following boundary conditions:

(1) Uniform inlet condition:

$$U = U_m, V = 0, \quad \text{at } X = -L_1, \quad -1 \leq Y \leq 1 \quad (2.45)$$

$$V = V_m, U = 0, \quad \text{at } Y = L_s, \quad -1 \leq X \leq 1 \quad (2.46)$$

(2) Fully developed outlet condition:

$$\frac{dU}{dX} = 0, V = 0, \quad \text{at } X = L_2, \quad -1 \leq Y \leq 1 \quad (2.47)$$

(3) No-slip wall boundaries: $U=V=0$.

Here U_m and V_m are determined iteratively.

The boundary condition for the pressure can be obtained by solving a one dimensional transport equation. For both ends of the main channel, the Y-momentum equation leads to,

$$\frac{\partial P}{\partial Y} = \sinh \Psi \frac{\partial \Psi}{\partial Y} \quad (2.48)$$

The above equation is obtained because the transverse velocity is assumed to be zero at the ends due to the presence of a flat velocity profile or fully-developed velocity profile, and Φ does not vary in the transverse directions. Integration of equation (2.48) leads to,

$$P = \cosh \Psi + P_0 \quad (2.49)$$

P_0 is the pressure at the channel ends, i.e. the pressure in the reservoirs. Ψ is the function of Y for the main channels.

For the side channel end, the pressure is given by the similiar equation as equation (2.48),

$$\frac{\partial P}{\partial X} = \sinh \Psi \frac{\partial \Psi}{\partial X} \quad (2.50)$$

$$P = \cosh \Psi + P_0 \quad (2.51)$$

but here Ψ is the function of X .

The physical explanation for the pressure boundary condition at the ends of the channel is that the electric potential due to the Debye double layer varies in the transverse direction. The transverse dependence of the electric potential results in electric force acting on the fluid which will only be balanced by a hydrodynamic force, that is, a non-uniform pressure distribution is present.

The numerical solution to the governing equations for the motion will be given in Chapter 3. The solution to the electric potential distribution is straight forward and will be discussed in this chapter.

2.5 Solution to the 1-D Poisson-Boltzmann Equation

2.5.1 Debye-Hückel Approximation and Exact Solution for a Flat Plate

Linearization of the $\sinh\Psi$ term for small dimensionless values of the potential, $ze\psi/kT$, leads to the Debye-Hückel approximation, viz. $\sinh\Psi \approx \Psi$. For a single channel,

$$\frac{d^2\Psi}{dY^2} = (\kappa a)^2 \Psi \quad (2.52)$$

$$\Psi = \zeta \quad \text{at } Y = 1 \quad (2.53)$$

$$\Psi = \zeta \quad \text{at } Y = -1 \quad (2.54)$$

Solution to the above equations gives,

$$\Psi = \frac{\zeta \cosh(\kappa a Y)}{\cosh(\kappa a)} \quad (2.55)$$

For the diffuse layer near a flat plate, the electric potential can be obtained analytically. The governing equation is given by

$$\frac{d^2\Psi}{dY'^2} = (\kappa a)^2 \sinh\Psi \quad (2.56)$$

where Y' is the distance from a wall. The boundary conditions for a flat plate are, $Y' \rightarrow \infty$, $\Psi = 0$, and $\Psi = \Psi_s$, at $Y' = 0$. The exact solution to equation (2.56) follows upon multiplying both sides by $d\Psi/dX$ to obtain exact differentials that, after integrating twice and applying the boundary conditions, yields,

$$\Psi = 2 \ln \left\{ \frac{1 + \exp(-\kappa a Y') \tanh(\frac{1}{4} \Psi_s)}{1 - \exp(-\kappa a Y') \tanh(\frac{1}{4} \Psi_s)} \right\} \quad (2.57)$$

The above solution can be used to predict the potential distribution across channel for large κa ($\kappa a \geq 10$), in which case, the potential, Ψ , at the centre of the channel is zero.

2.5.2 Numerical Solution to the 1-D P-B Equation and Comparison with Analytical Solutions

Equations (2.19)-(2.21) specify a 1-D problem for a straight capillary channel. However, the hyperbolic sine

term in the Poisson Boltzmann equation (2.19) makes the second-order differential equation exponentially non-linear. For large κa , the solution will be very steep near the wall, which suggests a 'stiff' equation[28]. Recently, Bowen and Jenner [29] introduced a position function $M(R)$ and transformed the original equation to a fourth order differential equation in terms of M . It is claimed that such a transformation reduces the stiffness of the equation, but the resulting equation is still non-linear and it is more complicated.

Here, we use a finite difference approximation of second order accuracy for nonuniform grid size. The three points quadratic interpolation formula is given by:

$$f = f_i + \frac{(f_{i+1} - f_i)(h_1 + x)h_1 - (f_{i-1} - f_i)(h_2 - x)h_2}{h_1 h_2 (h_1 + h_2)} x \quad (2.58)$$

Where h_1 and h_2 are the two grid spacings of the node of interest (see figure 2.2). f is any general variable of interest. It should be noted that equation (2.58) is quadratic in the parameter x (i.e. location).

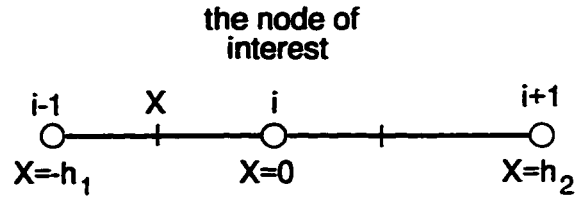


Figure 2.3 The nodal arrangement for one dimensional problem.

Equation (2.19) is discretized using the formula (2.58) and the resulting difference equations were solved iteratively using the Thomas algorithm[48]. The solution is facilitated by relaxing the hyperbolic term with the Taylor formula, that is,

$$\sinh \Psi \approx \sinh \Psi^* + (\Psi - \Psi^*) \cosh(\Psi^*) \quad (2.59)$$

Where Ψ^* is a currently available value during an iteration. It is found that the convergence is very fast even for large κa in which case the variation of Ψ is very steep near the wall, and for large surface potential ζ in which case the Poisson-Boltzmann equation can not be linearized.

Numerical results and their comparison with the analytical solution are given in figures 2.4 through 2.7.

Figures 2.4-2.7 compare the potential calculated from the exact solution for large κa and the Debye-Hückel approximation with the numerical solutions. It is shown that the numerical solution agrees well with both the analytical solution for large κa and all surface potential values and Debye-Hückel solution for small ζ values and all κa values.

It is also shown that Debye-Hückel approximation may be satisfactorily applied to small surface potentials (figures 2.4 and 2.6 for $\zeta=0.1, 1.0$ respectively) except for very small κa , but for large surface potential (figure 2.5, $\zeta =6.0$) the Debye-Hückel errs substantially. Figure 2.7 shows that for large surface potentials there still exist differences between the exact solution and the Debye-Hückel approximation even for very large κa .

2.6 Numerical Solution to Electric Potentials for the T-shaped Channels

2.6.1 Electric Potential due to Debye Double Layer

For the case of a T-shaped channel as shown in figure 2.1, equation (2.15) with boundary conditions (2.17) through (2.24) was solved using a finite difference method. The method is straight forward, therefore, the solution algorithm will not be discussed here in detail. The results are shown in figure 2.8 and 2.9 for $\kappa a = 20$, $\zeta = \zeta' = 1.0$, $L_1 = L_2 = L_s = 50$, here, L_1 , L_2 and L_s represent the length of the left, right and side channel, respectively.

Figure 2.8 shows the electric potential distributions due to the electrical double layer at the intersection region in the main channel. It shows a big gap at the intersection due to the presence of the side channel. The presence of a side channel influences the potential distributions only in the region close to the intersection (about $-1.2 \leq X \leq 1.2$). The electric potentials due to the double layer do not vary axially in the main channel for $X \leq -1.2$ or $X \geq 1.2$.

Figure 2.9 shows the electric potential distributions due to the electric double layer at the intersection region in the side channel. For $Y \geq 1.2$, the potential does not change along the side channel.

2.6.2 Electric Potential due to External Electric Field

The numerical formulae to solve equation (2.28) through (2.30) are the same as that of the potential due to the Debye layer. The results are shown in figures 2.10 and 2.11 for $L_1 = L_2 = L_s = 50$. It is shown that the potential distribution due to the external electric field is linear except at the junction area where a potential perturbation is expected. Figure 2.10 shows the electric potential distribution in both the main and side channel with three potentials applied at three reservoirs, respectively. Plots a) and b) in figure 2.10 show the electric potential distribution due to external electric field in the main channel. In particular, b) is an expanded view at the intersection. It is shown that in the intersection region ($-3 \leq X \leq 3$), there exist differences in the electric potential across the main

channel. Plots c) and d) in figure 2.10 show the electric potential distribution along the side channel. The potential perturbation at the intersection can also be observed. The electric potential will not change beyond the intersection region.

When the side channel is left floating, from figure 2.11, it is interesting to note that the potential in the side channel remains the same, except in the region close to the intersection. The perturbation occurs at the intersection region ($-3 \leq X \leq 3$ in the main channel, and $Y \leq 3$ in the side channel).

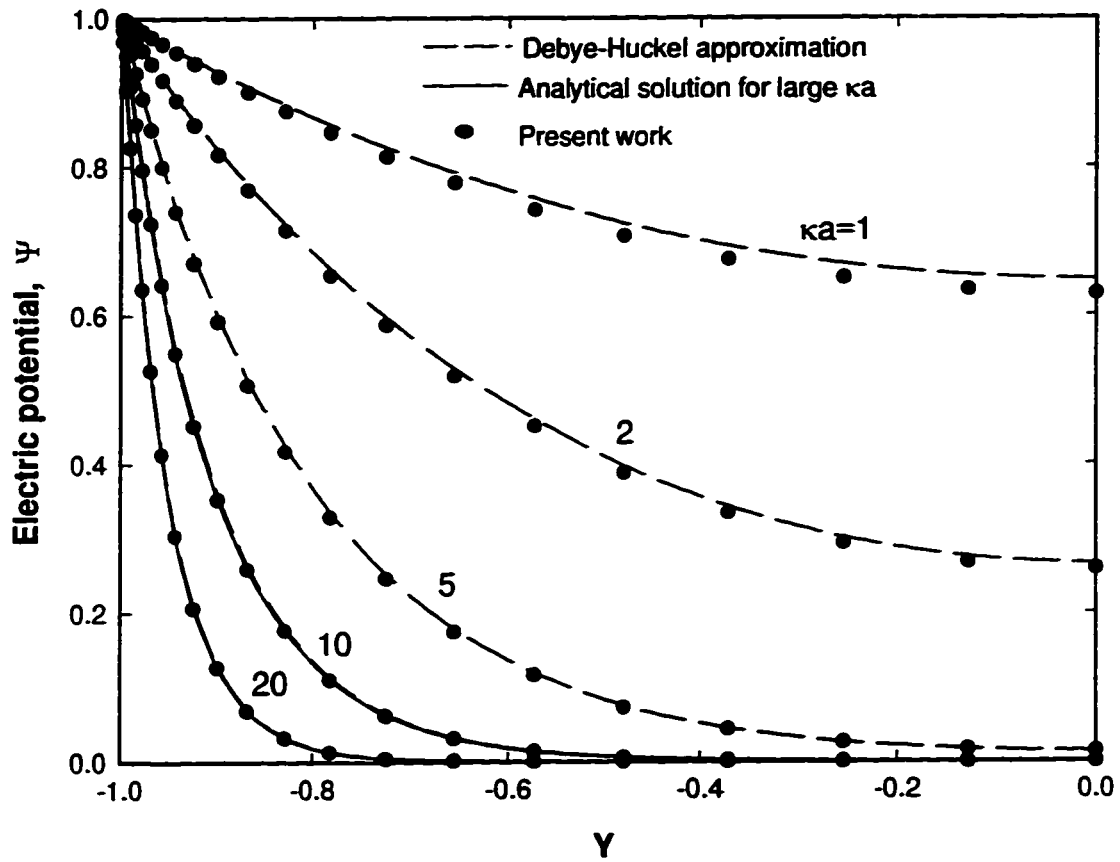


Figure 2.4 Dimensionless transverse electrostatic potential distribution across a channel for different κa values at a fixed wall potential ($\zeta=1$) using three different methods.

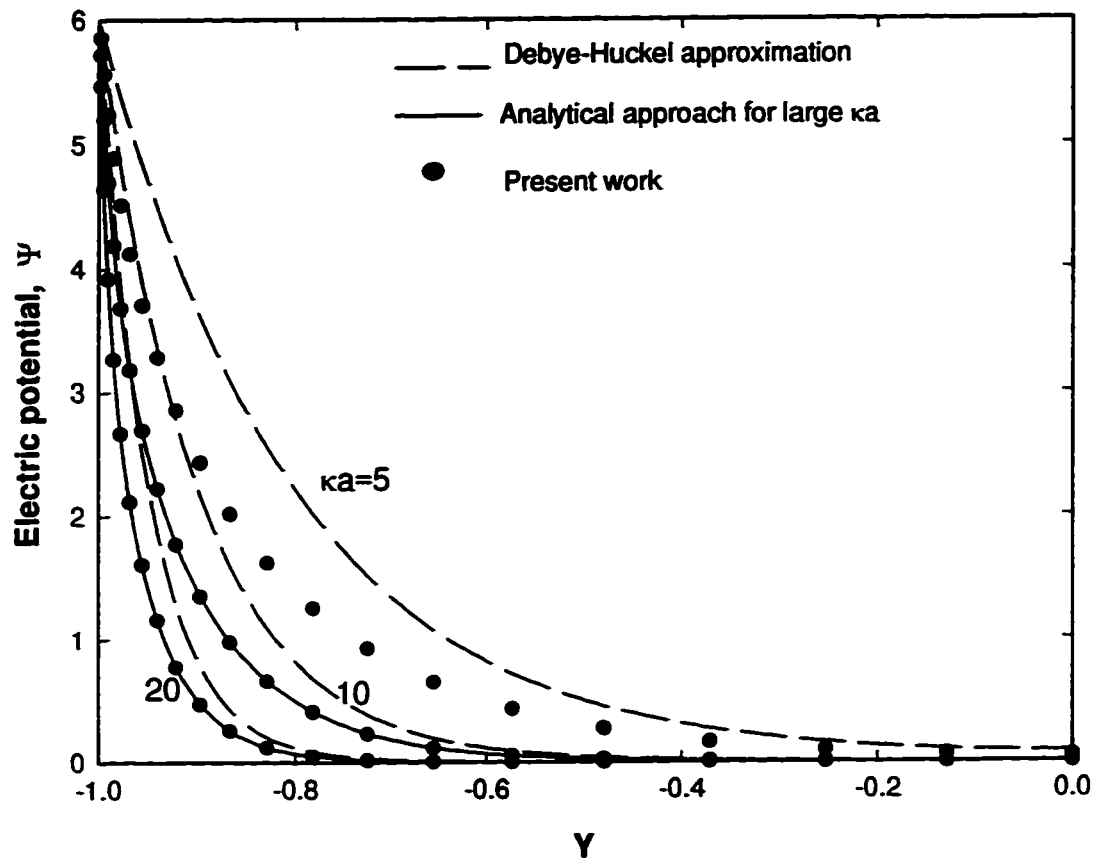


Figure 2.5 Dimensionless transverse electrostatic potential distribution across a channel for different κa values at a fixed wall surface potential ($\zeta=6$) using three different methods.

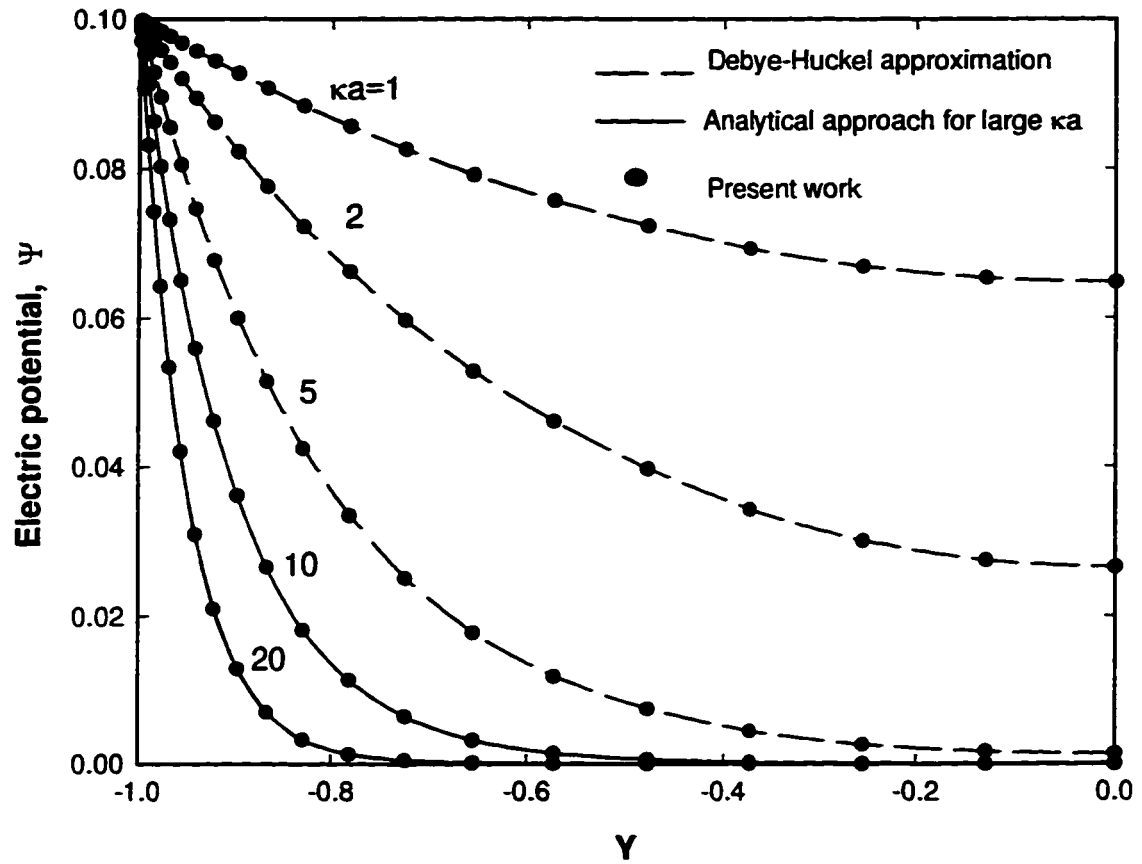


Figure 2.6 Dimensionless transverse electrostatic potential distribution across a channel for different κa value at a fixed wall potential ($\zeta=0.1$) using three different methods.

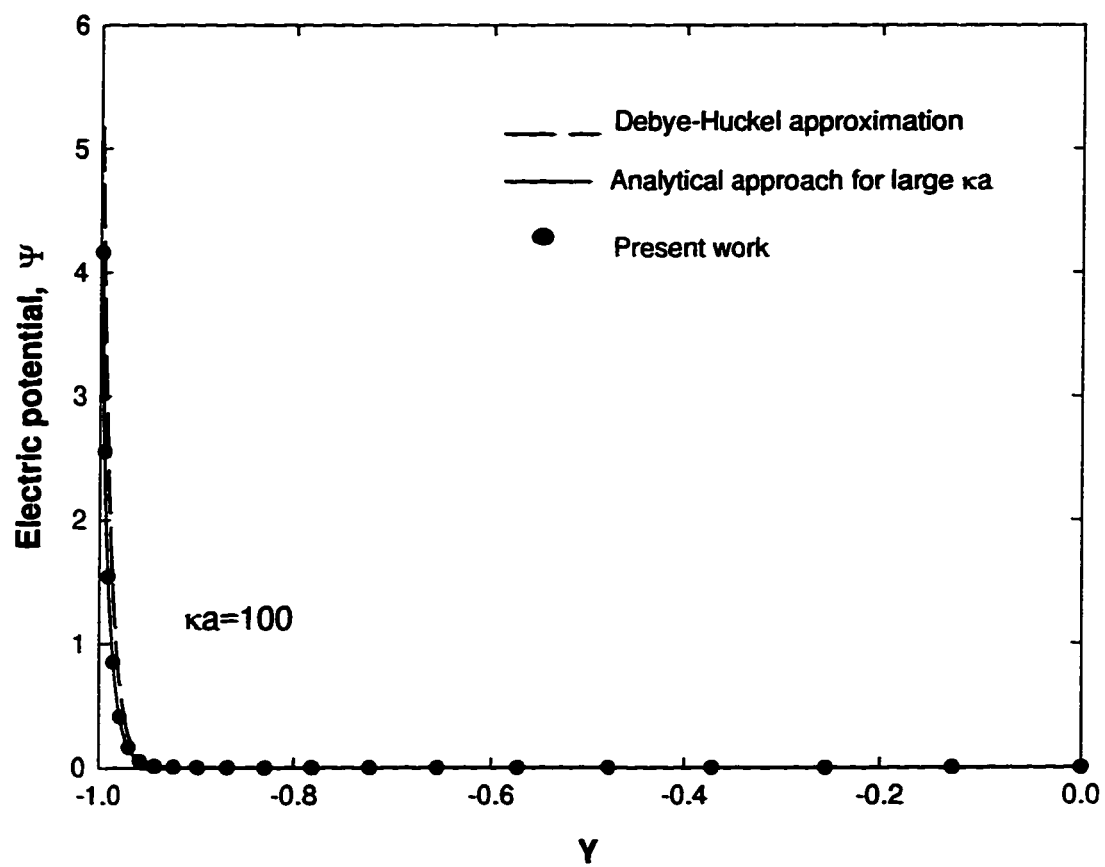


Figure 2.7 Dimensionless electrostatic potential distribution across a channel for $\kappa a = 100$ and surface potential $\zeta = 6$ using three different methods.

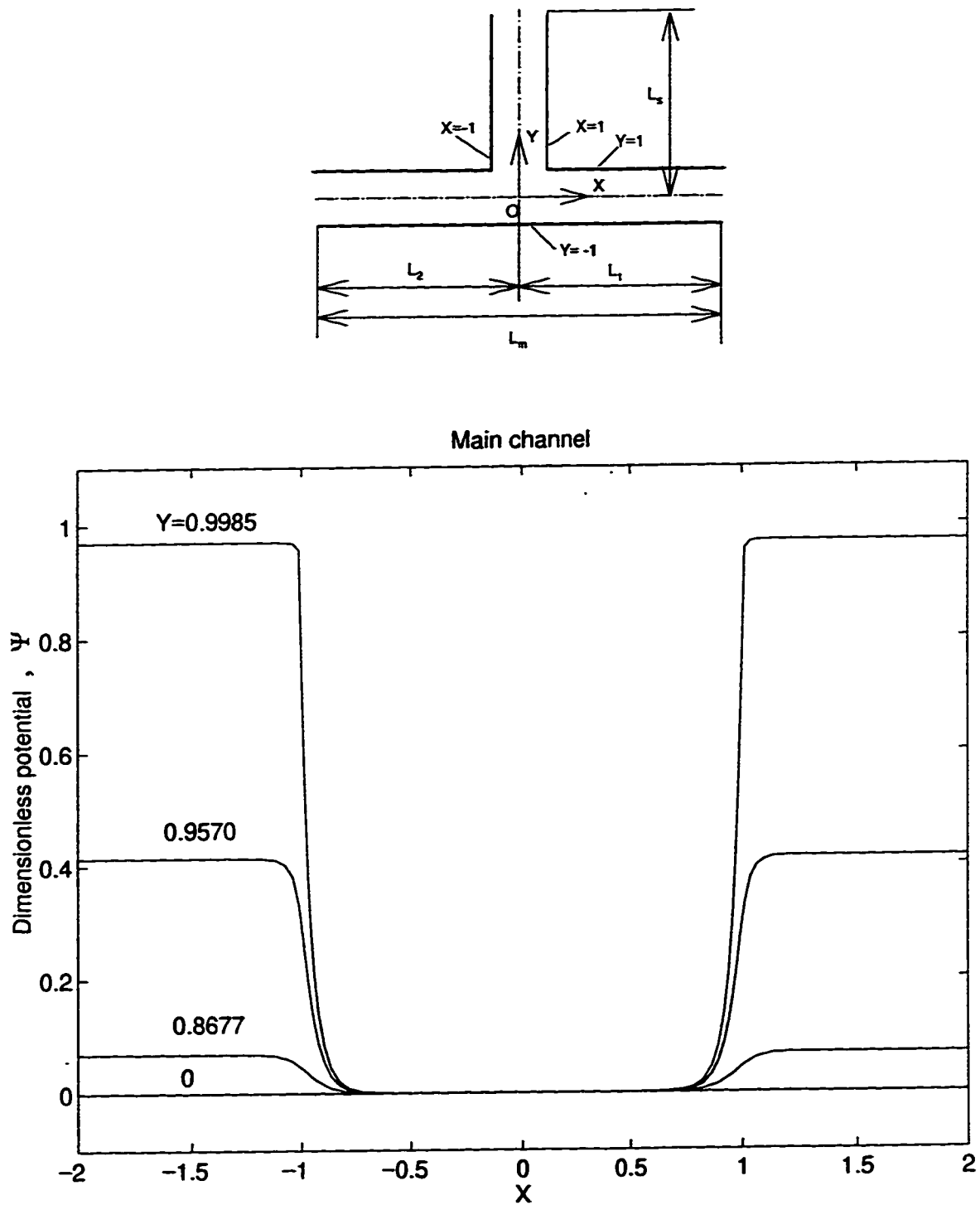


Figure 2.8 Dimensionless electric potential distribution due to Debye double layer at intersection region in main channel for $\kappa a = 20$, $\zeta = \zeta' = 1.0$, $L_1 = 50$, $L_2 = 50$, $L_s = 50$.

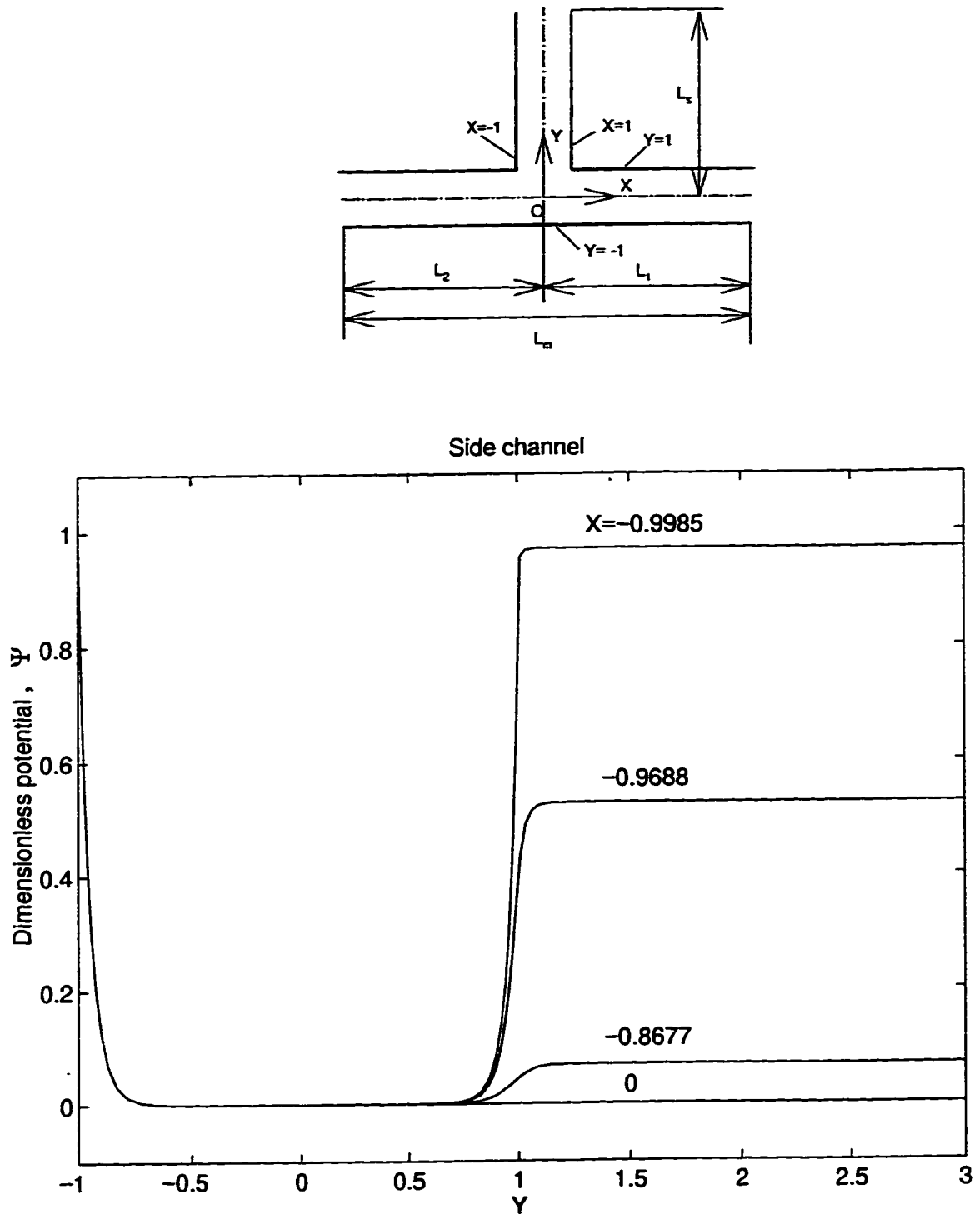


Figure 2.9 Dimensionless electric potential distribution due to Debye double layer at intersection region in side channel for $\kappa a=20$, $\zeta=\zeta'=1.0$, $L_1=50$, $L_2=50$, $L_s=50$.

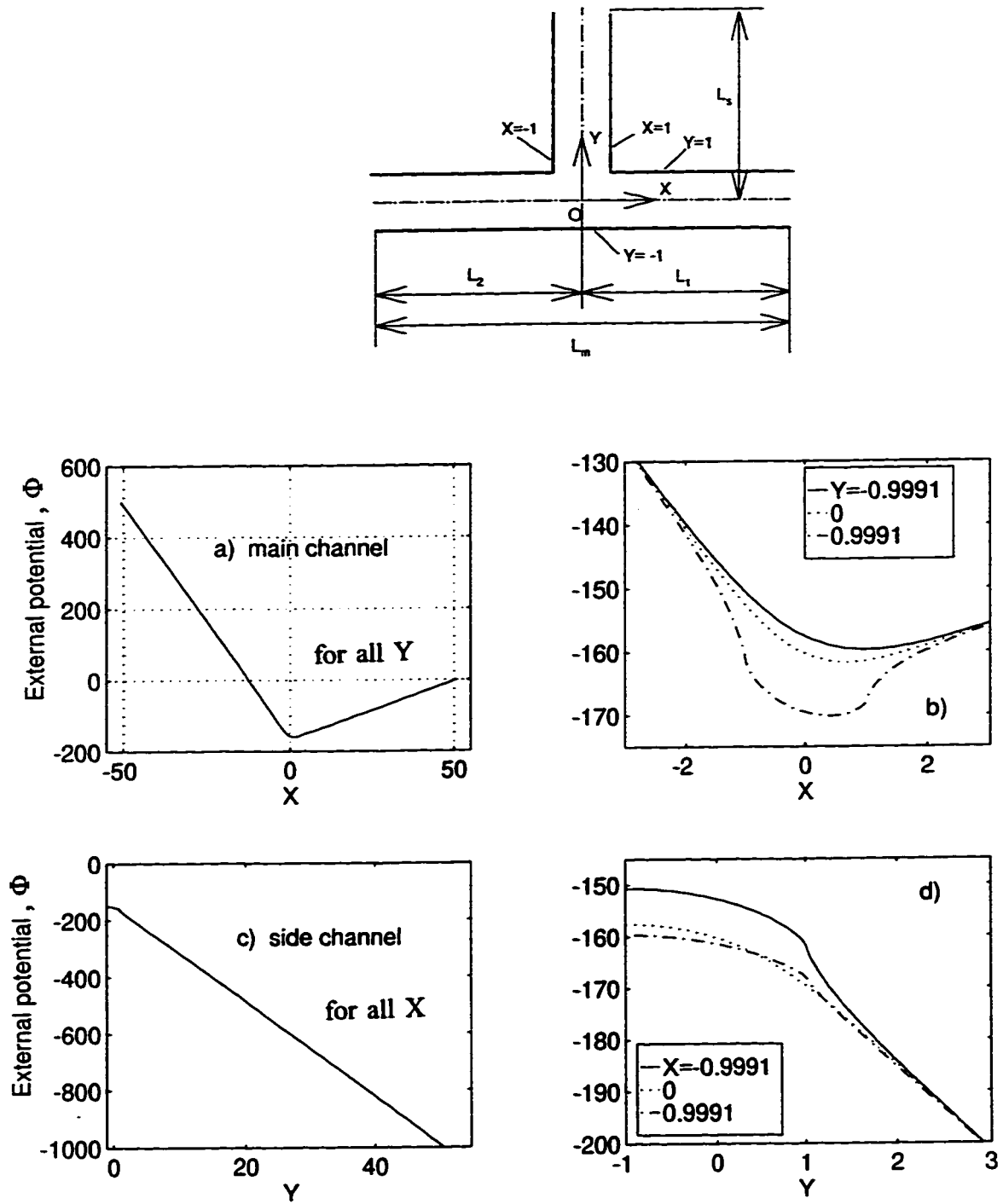


Figure 2.10 The external potential distribution along the channels ($\Phi_1 = 500$, $\Phi_2 = 0$, $\Phi_3 = -1000$, $L_1 = L_2 = L_s = 50$), b and d are expanded view at intersection.

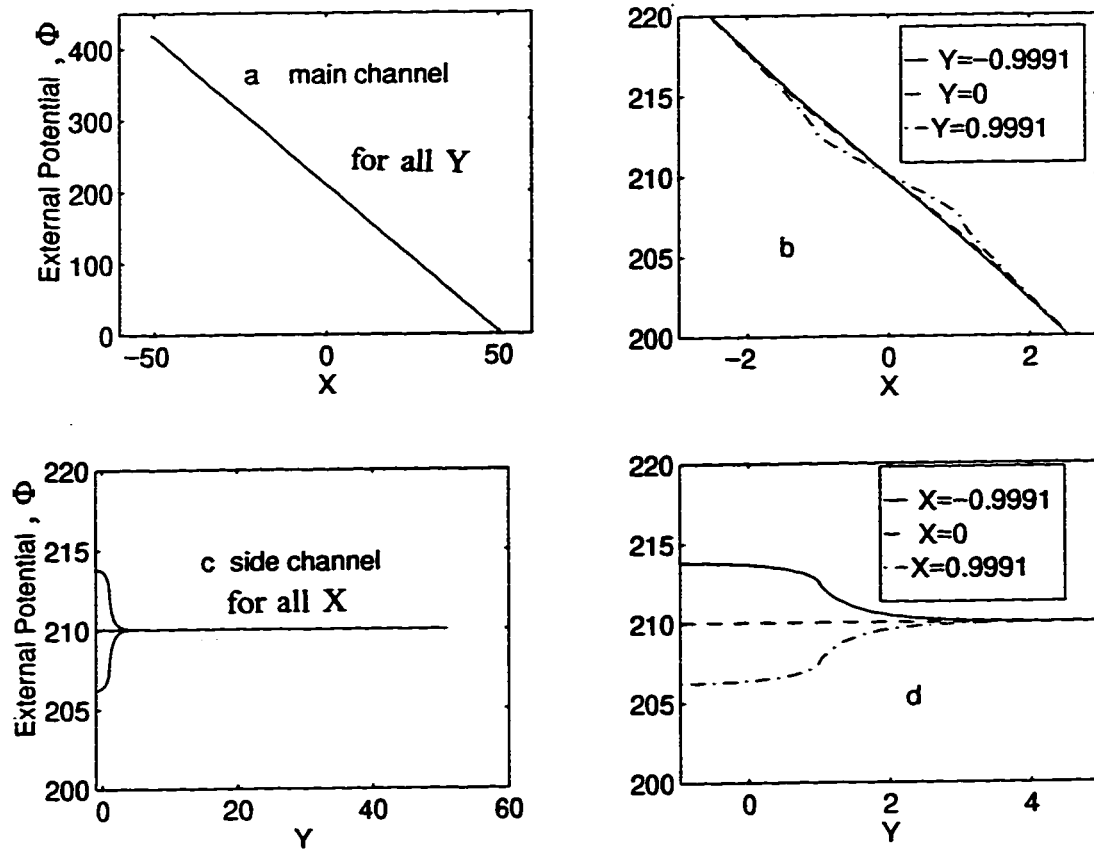
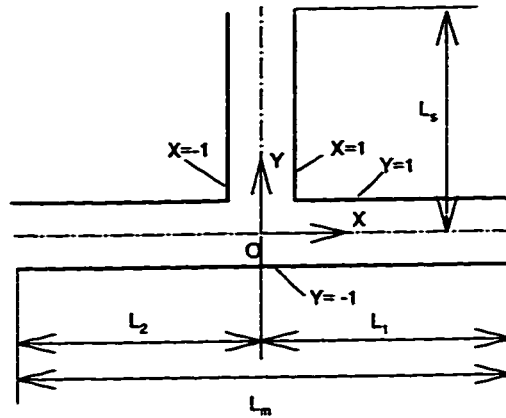


Figure 2.11 The external electric potential in the channels ($\Phi_1=420$, $\Phi_2=0$, floating side channel, $L_1=L_2=L_s=50$), b and d are expanded view at intersection.

Chapter 3

Numerical Implementation of Flow Equations

3.1 Introduction

The governing equations (2.42) to (2.48) form a set of elliptic partial differential equations. They cannot be solved analytically in a closed form and hence they must be solved numerically. Based on the assumption that the flow is in the creeping flow regime and that the Boltzmann distribution can be invoked, the potential distribution can be decoupled from the transport equations. Once the electrical potential distributions are obtained, the major calculation step is the solution of the transport equations as presented by the modified Navier-Stokes and the continuity equations.

Current techniques for the solution of incompressible viscous flows can be categorized as (a) primitive variable (b) vorticity - stream function (c) vorticity - velocity methods[31]. A literature review reveals an on-going concern with the primitive variable approach. The so-called primitive variables are the velocity components and pressure. By transforming the continuity equation into a pressure-Poisson equation, the approach led to the development of the SIMPLE (Semi-Implicit Method for the Pressure Linked Equations) algorithm[32-35]. This method proved to be a remarkably successful implicit

method over the last two decades in resolving the pressure -velocity coupling in incompressible flow problems. As with any other algorithm, the application of algorithm SIMPLE is not without its difficulties. The SIMPLE-C[35] and SIMPLER[33] have been developed as enhancement to the SIMPLE algorithm. Based on the SIMPLE algorithm, a Separation Method of Liu and Masliyah [30] was developed which is a first order non-conforming numerical scheme with a 3-point exponential interpolation. They decoupled the multi-dimensional problem into multiple one-dimensional sub-problems upon discretizing. The velocity and pressure are decoupled at each iteration using Patankar's pressure correction method. The separation method has been shown to possess the property of good convergence and improved economy. The following algorithm will mainly depend on the Separation Method, as well some concepts of the SIMPLE-C will also be applied for this electrokinetic flow problem.

3.2 Finite Difference Equations

3.2.1 Grid Definition

The staggered grid, figure 3.1, shows the nodal arrangement in the calculation domain for a 2-dimensional problem. The spacing between the grid lines is non-uniform with a fine grid near the wall and the entrance region where the velocity gradient is steep, and a coarser grid at the centre of the tube and far away from a perturbed region. The purpose of the non-uniform mesh is to minimize the total number

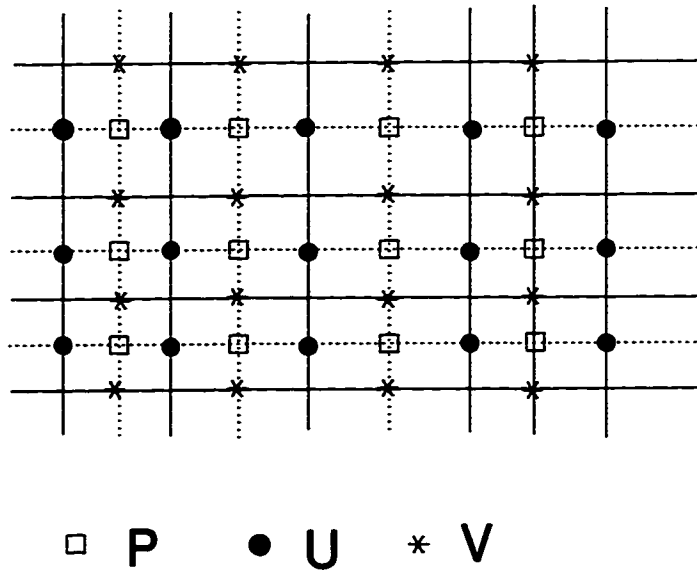


Figure 3.1. Staggered grid

of nodes in the calculation domain.

In this study, U and V grid lines are first determined in the x and y directions, respectively. P grid points are then placed at the centre of the cell formed by adjacent U and V grids. The electric potential shares the same grid as P.

The quadratic interpolation function (equation 2.58) in a nonuniform one-dimensional grid will be used to obtain finite difference equations.

3.2.2 Discretization of the Momentum Equation

Using equation (2.58) as a quadratic approximation for the velocity, the diffusion term of equation (2.42) can be discretized as a finite difference term,

$$\frac{\partial^2 U}{\partial X^2} = \frac{2(U_{i+1,j} - U_{i,j})}{(X_{i+1} - X_j)(X_{i+1} - X_{i-1})} + \frac{2(U_{i-1,j} - U_{i,j})}{(X_i - X_{i-1})(X_{i+1} - X_{i-1})} \quad (3.1)$$

$$\frac{\partial^2 U}{\partial Y^2} = \frac{2(U_{i,j+1} - U_{i,j})}{(Y_{j+1} - Y_j)(Y_{j+1} - Y_{j-1})} + \frac{2(U_{i,j-1} - U_{i,j})}{(Y_j - Y_{j-1})(Y_{j+1} - Y_{j-1})} \quad (3.2)$$

$$\frac{\partial P}{\partial X} = \frac{P_{i,j} - P_{i-1,j}}{X_i - X_{i-1}} \quad (3.3)$$

$$\frac{\partial \Phi}{\partial X} = \frac{\Phi_{i,j} - \Phi_{i-1,j}}{X_i - X_{i-1}} \quad (3.4)$$

Note that equation (3.3) implies a linear approximation for the pressure dependence on X. Substitution of equations (3.1-3.4) into (2.42) leads to

$$au U_p = eu U_E + wu U_w + nu U_N + su U_s + b + S \quad (3.5)$$

or more simply

$$au U_p = \sum a_{nb} U_{nb} + b + S \quad (3.6)$$

where the summation is over the appropriate neighbour points (e.g. $i-1$ to $i+1$, $j-1$ to $j+1$).

The coefficients are given as

$$eu = \frac{2}{(X_{i+1} - X_i)(X_{i+1} - X_{i-1})} \quad (3.7)$$

$$wu = \frac{2}{(X_i - X_{i-1})(X_{i+1} - X_{i-1})} \quad (3.8)$$

$$nu = \frac{2}{(Y_{j+1} - Y_j)(Y_{j+1} - Y_{j-1})} \quad (3.9)$$

$$su = \frac{2}{(Y_j - Y_{j-1})(Y_{j+1} - Y_{j-1})} \quad (3.10)$$

$$au = eu + wu + nu + su \quad (3.11)$$

$$b = \frac{\partial P}{\partial X} = \frac{P_{i,j} - P_{i-1,j}}{X_i - X_{i-1}} \quad (3.12)$$

$$S = \sinh \Psi \frac{\partial(\Psi + \Phi)}{\partial X} \quad (3.13)$$

The Y-momentum equation is similarly discretized, resulting in the same form as equation (3.6) except with minor differences in the coefficients

$$av V_p = \sum a_{nb} V_{nb} + b + S \quad (3.14)$$

$$b = \frac{\partial P}{\partial Y} = \frac{P_{ij} - P_{ij-1}}{Y_j - Y_{j-1}} \quad (3.15)$$

$$S = \sinh \Psi \frac{\partial(\Psi + \Phi)}{\partial Y} \quad (3.16)$$

3.2.3 Treatment of the Continuity Equation

The pressure correction method of Patankar [32-35] will be used to treat the continuity equation. For any guessed pressure field P^* , the velocity U^* obtained by solving the U-momentum equations satisfies equation(3.5) as seen below,

$$au U_P^* = eu U_E^* + wu U_W^* + nu U_N^* + su U_S^* + \frac{\partial P}{\partial X} + S \quad (3.17)$$

where au, eu, wu, su and nu are the coefficients for U in equation (3.17). Correction of the guessed pressure by $P' = P - P^*$ is therefore necessary to correct the U^* by $U' = U - U^*$. The relationship between U' and P' can be approximated as,

$$U' = \frac{1}{au} \frac{\partial P'}{\partial X} \quad (3.18)$$

Here the SIMPLE algorithm is applied, ie the term $\sum a_{nb} U'_{nb}$ is neglected for economic calculation. Similarly for V, the correction term is written as,

$$V' = \frac{1}{av} \frac{\partial P'}{\partial Y} \quad (3.19)$$

The continuity equation becomes a pressure-Poisson equation

$$\frac{\partial}{\partial X} \left(\frac{1}{au} \frac{\partial P'}{\partial X} \right) + \frac{\partial}{\partial Y} \left(\frac{1}{av} \frac{\partial P'}{\partial Y} \right) = -\nabla \cdot \vec{U}^* \quad (3.20)$$

Where

$$\nabla \cdot \vec{U}^* = \frac{\partial U^*}{\partial X} + \frac{\partial V^*}{\partial Y} \quad (3.21)$$

Discretizing of equation (3.20) leads to

$$a_p P'_p = e_p P'_E + w_p P'_W + n_p P'_N + s_p P'_S + b_p \quad \text{or} \quad a_p P' = \sum a_{nb} P'_{nb} + b_p \quad (3.22)$$

where

$$a_p = e_p + w_p + n_p + s_p \quad (3.23)$$

$$e_p = \frac{1}{a_u(X_{i+1} - X_i) \Delta X} \quad (3.24)$$

$$w_p = \frac{1}{a_u(X_i - X_{i-1}) \Delta X} \quad (3.25)$$

$$n_p = \frac{1}{a_v(Y_{j+1} - Y_j) \Delta Y} \quad (3.26)$$

$$s_p = \frac{1}{a_v(Y_j - Y_{j-1}) \Delta Y} \quad (3.27)$$

$$\Delta X = X_i - X_{i-1}, \quad \Delta Y = Y_j - Y_{j-1} \quad (3.28)$$

$$b_p = -\frac{\Delta U^*}{\Delta X} - \frac{\Delta V^*}{\Delta Y} \quad (3.29)$$

It is noted that a quadratic approximation of the velocity and the linear approximation for the pressure have been used in order to yield a stable scheme [30].

3.2.4 Boundary conditions

The treatment of the boundary must be consistent with the interior points. Application of the velocity boundary conditions is straightforward, however, the boundary condition for the pressure correction equation is not obvious. The general rule recommended in reference [30] is used.

1. Only when the gradient is known should one use a symmetrically extrapolated grid outside of the domain of interest. Under no other circumstances should one use a grid point outside the domain of interest.

2. For a Dirichlet velocity boundary condition, all the velocity components must have a grid point on the boundary. The pressure nodes are not necessarily placed on the boundary. $\partial p'/\partial n = 0$ becomes the boundary condition.

3. When the velocity gradient is known on a boundary, the pressure node can be placed on the boundary. However, the normal velocity components should not be placed at the boundary.

4. The pressure node must be present on a pressure-known boundary, where the normal velocity is not present. In this case, $p'=0$ should be set at the boundary.

3.3 Solution Procedure

3.3.1 Under-relaxation Factor

To moderate the changes in the consecutive solutions, under-relaxation is introduced to the momentum equations (3.6) through α as,

$$(1+\alpha)auU_p = \sum a_{nb}U_{nb} + \frac{\Delta P}{\Delta X} + S + \alpha auU^* \quad (3.30)$$

where U^* is the currently available value of U . The same factor is used for both U and V equations. The optimal value of α lies in the range of 0.1-0.25.

The relaxation factor in the pressure correction equation is different from that of the momentum equation. Since the initial value of P' is uniformly zero, the relaxation

factor is introduced to equation (3.22) in the following way,

$$(1 + \alpha_p) a_p P' = \sum a_{nb} P'_{nb} + b_p \quad (3.31)$$

We have noted that the under-relaxation factor α_p is very important for the convergence of P' equation, here $\alpha_p=0.25$ has been used.

3.3.2 Solution Procedure

- 1) Guess the pressure field and initialize the velocity.
- 2) Evaluate the coefficients of the momentum equations (such as equation(3.7) to equation(3.12)) and the source term using the local potential fields which have been obtained by solving equation (2.15) and equation(2.28).
- 3) Solve the momentum equation to obtain U^* and V^* values.
- 4) Evaluate the coefficients of the pressure correction equation and solve for P' , and correct the pressure field $P=P^*+P'$.
- 5) Repeat steps 2-4 until continuity equation is satisfied.

The accelerated TDMA-Solver proposed by (Van Doormal & Raithby)[35] was found to be effective. A θ value of 1.90 was used for both the momentum and the pressure correction equations. The accelerated TDMA-Solver was used together with an ADI technique. At each iteration, usually 5 sweeps in each direction for the momentum equations and then 5 sweeps for the pressure correction equation were found to be sufficient for fast convergence.

3.3.3 Convergence Criteria

The overall iteration procedure for the momentum and pressure correction equations was terminated when the relative grid average error in continuity equation was less than 10^{-5} . Hence the momentum equations are satisfied as long as the pressure field is correct. The average relative error for the continuity equation is given by[30],

$$RSD = \frac{\sum \frac{|PRH_{ij}|}{|FLOWIN_{ij}| + |FLOWOUT_{ij}|}}{\sum 1} \quad (3.32)$$

where PRH_{ij} is the error in the flow in and out of the conservational domain of P_{ij} and $FLOWIN$ and $FLOWOUT$ are the flow into and out of the conservational domain, respectively. This algorithm has been embodied in a computer program using Fortran-77 language.

3.4 Test of Flow Program

In developing a possible new numerical scheme for solving the Navier-Stokes equation, the channel entrance problem has often been regarded as a standard problem for comparison. There are numerous investigations of the entrance flow in a channel made of two parallel plates. Previously reported contributions [36-45] deal with different versions of the classical finite difference and finite element methods as well as with approximate analytic-type solutions obtained through linearization of the inertia term. Various inlet flow conditions were considered, with particular emphasis on uniform

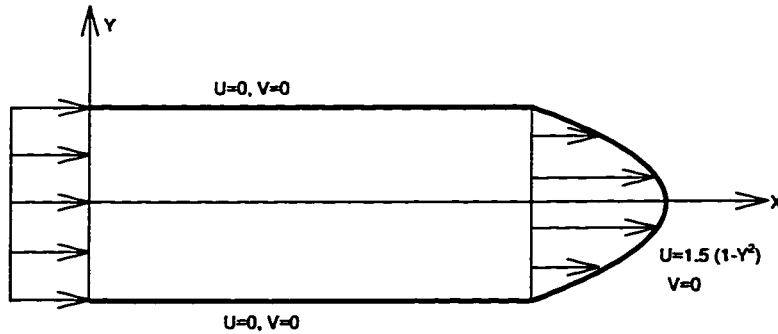


Figure 3.2. Geometry and coordinate system for developing duct flow

parallel flow. The outflow boundary condition is in general handled via consideration of a fully developed velocity profile at a sufficiently large truncated channel length. Recently, a hybrid numerical-analytical approach (the generalized integral transform

technique, GITT) for incompressible steady state Navier-Stokes equation was employed to solve this problem[44,45]. The creeping flow regime ($Re=0$) in the developing region is considered here, the results will be compared with the literature data.

Consider creeping flow of a Newtonian fluid inside a parallel plates channel with a uniform parallel inlet axial velocity distribution as shown in figure 3-2. The pressure at outlet is specified as $P=0$. The solution was obtained on a Risc6000 main frame computer using a 50×21 unequal spaced grid system with a fine grid size near the entrance region and near the wall, and a coarser grid as the fully developed region is approached. A typical CPU time for a converged solution is about 150 seconds.

Figure 3.3 shows the development of the axial velocity profile for creeping flow. It is noted that for small X values (in the entrance region) the velocity profile includes a local minimum at the axis, $Y=0$, and symmetrically located maxima on either side of the center line near the wall. The velocity overshoots have also been reported by other investigators [40-42, 45]. The physical explanation for this phenomena is that, due to the no-slip condition at the walls, the core flow must be accelerated in order to satisfy the continuity equation. However, the flow acceleration does not instantaneously reach the center line, therefore such bulges appear near the walls for small X . This type of velocity profile has been observed up to $Re=2000$ [40].

Figure 3.4 compares the center line velocities computed by various researchers. It is shown that the present solution agrees well with the solution due to integrated transform techniques[45] and the solution of a finite element method[38]. Figure 3.5 shows the development of the axial velocity along the channel at various values of Y . The flow development is not sensitive to the transverse location.

Figure 3.6 illustrates the development of the transverse velocity components along the duct entry region, showing the expected migration of the relative maximum towards the duct center line as the flow develops.

The distribution of mean pressure across the flow cross section versus the downstream distance and its comparison with literature data are shown in figure 3.7. It is seen that the value of the pressure gradient increases for decreasing values of X . It also shows that the present work agrees well with the literature data.

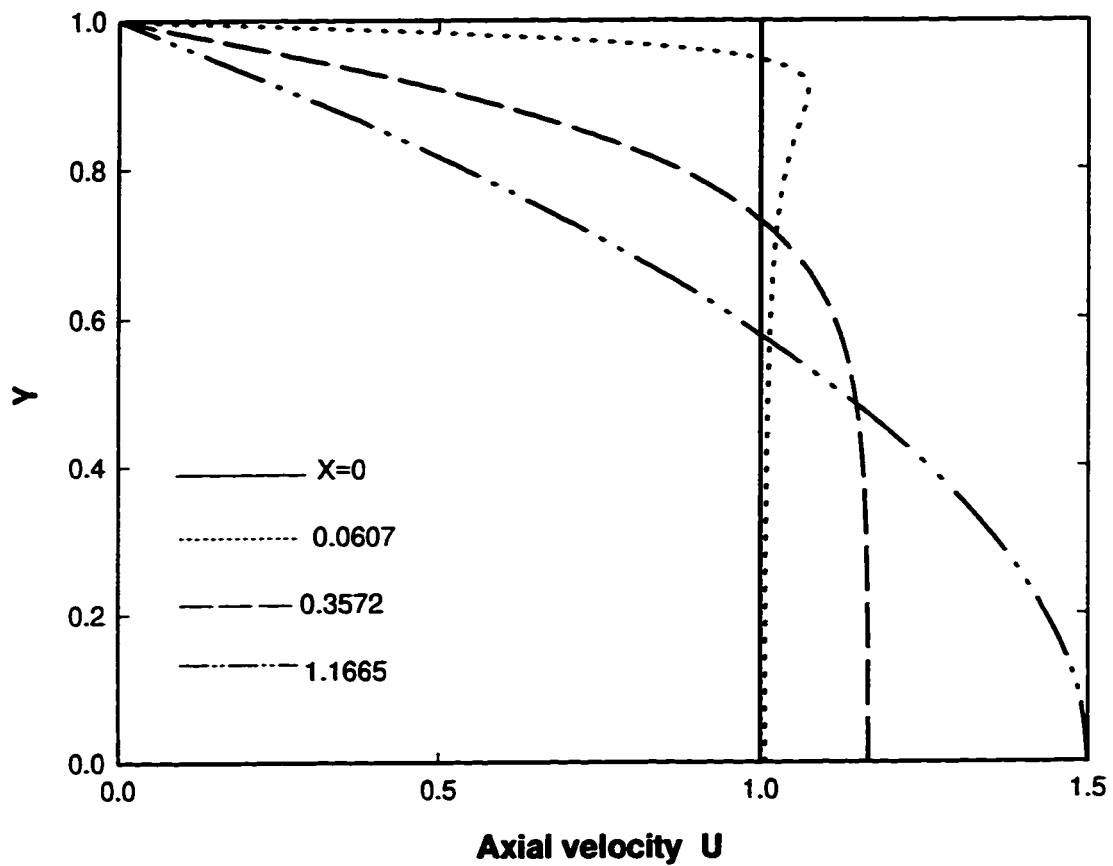


Figure 3.3 Velocity profile development between parallel plates for the creeping flow regime

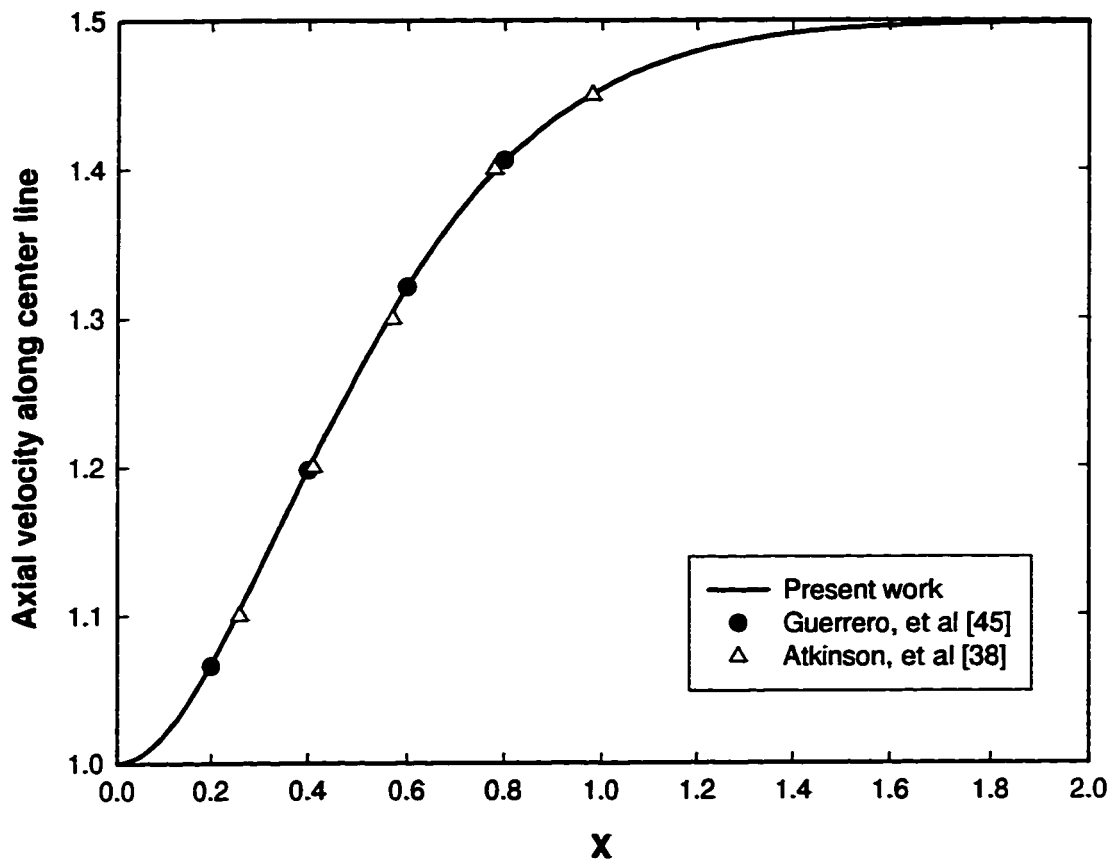


Figure 3.4 Creeping flow for axial velocity development between two parallel plates

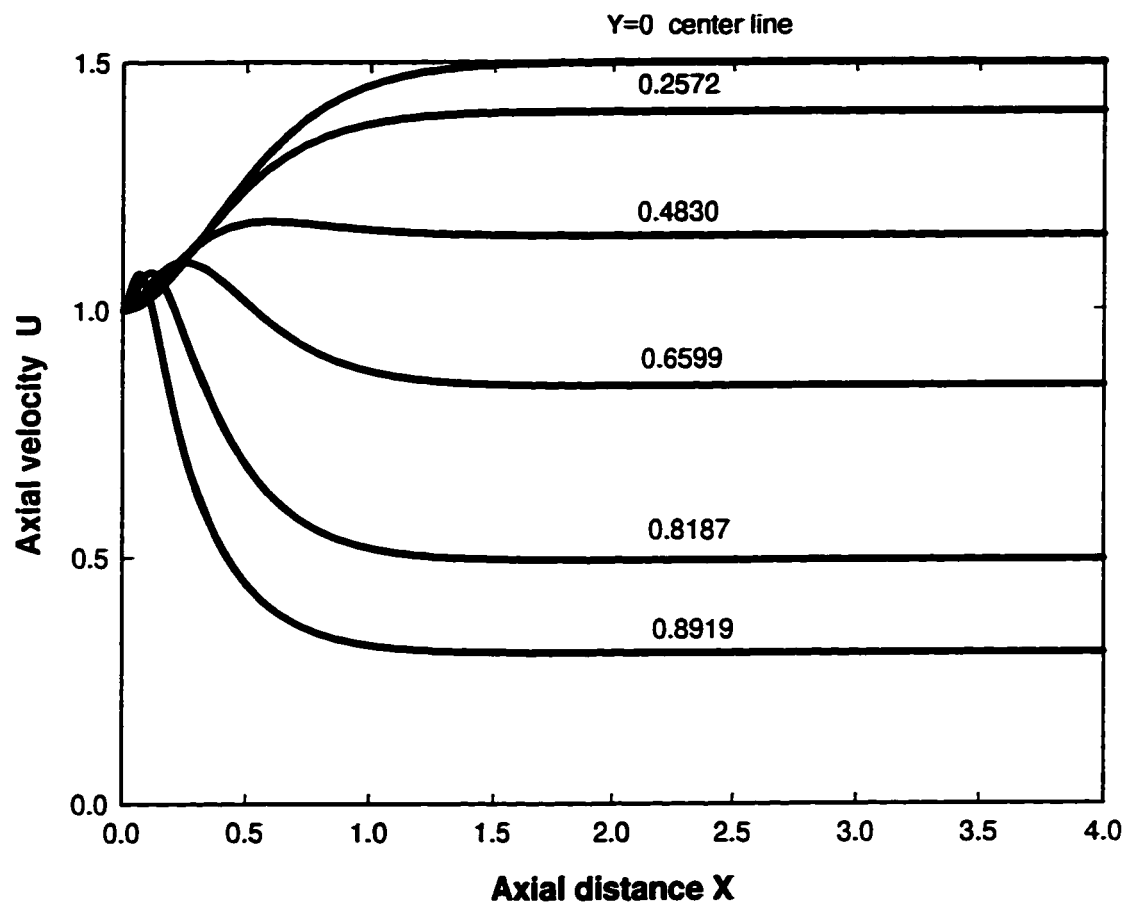


Figure 3.5 Development of axial velocity, U in the creeping flow regime.

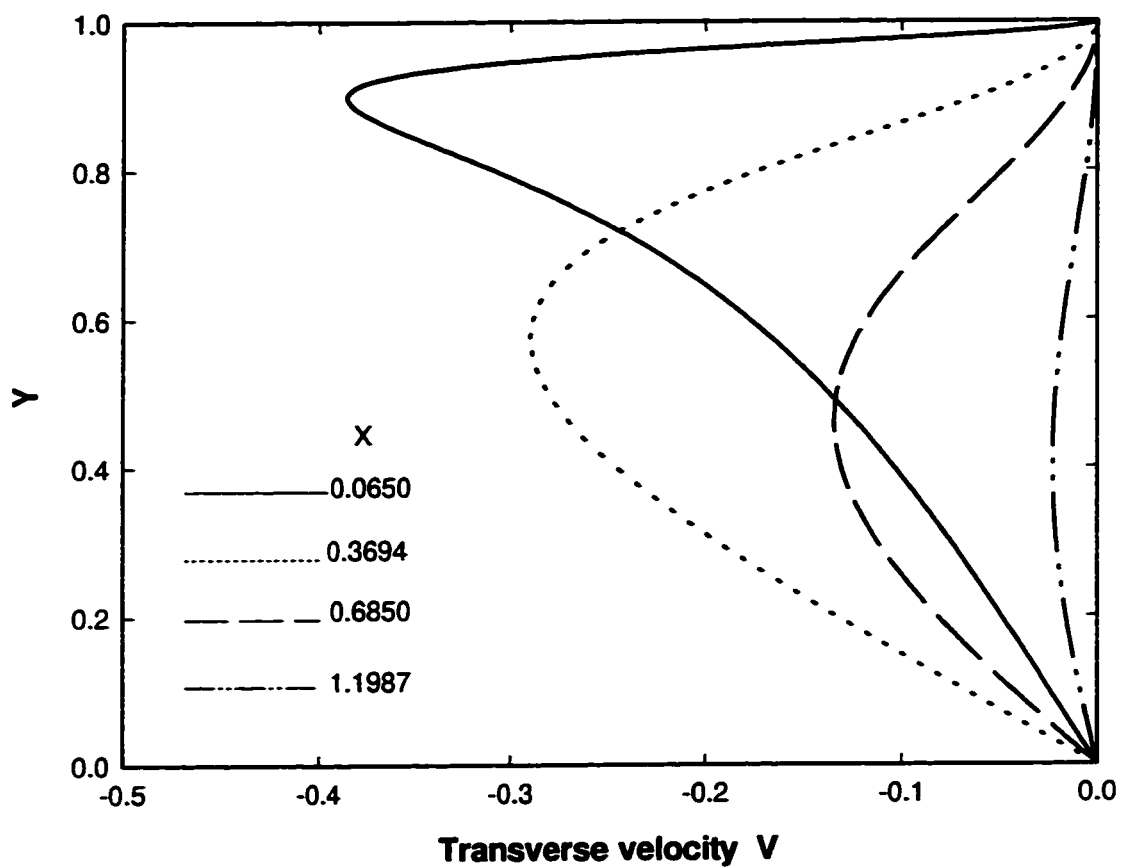


Figure 3.6 Transverse velocity profile development between parallel plates in creeping flow regime

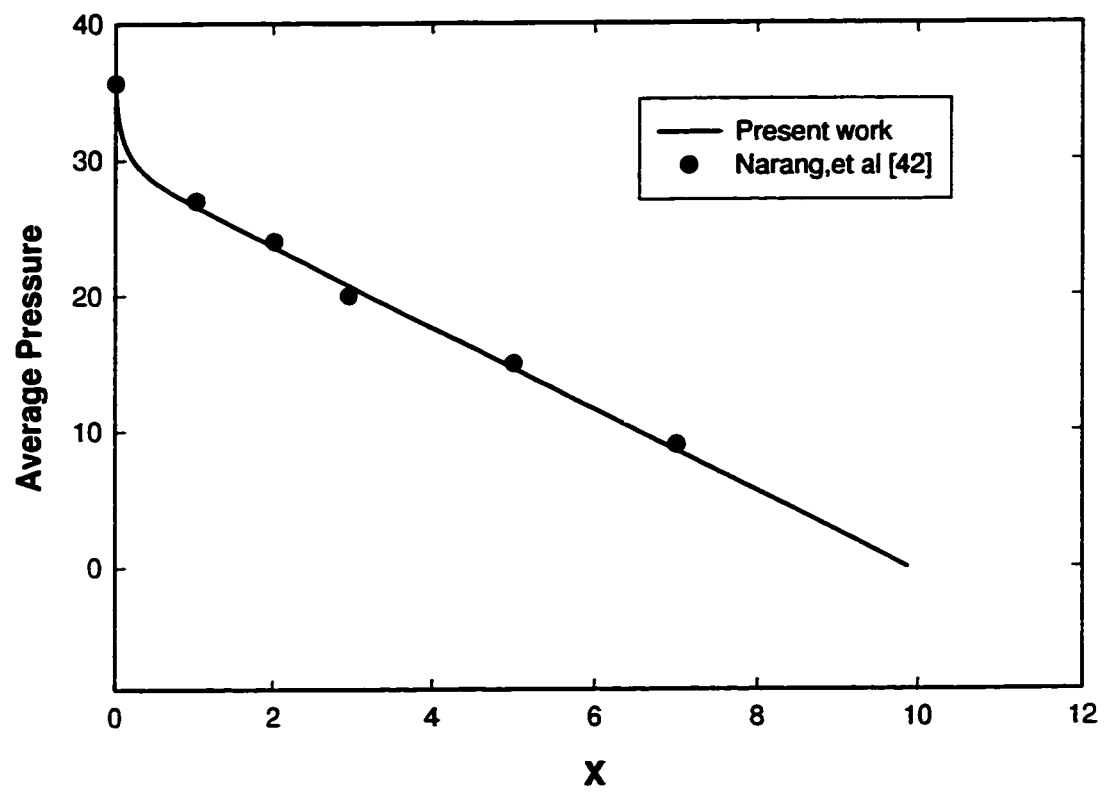


Figure 3.7 Average pressure variation along a two-dimensional channel

Chapter 4

Electroosmotic Flow in a Straight Channel

4.1 Introduction

For a surface zeta potential of less than 25 mV, the Debye-Hückel approximation can be invoked and the analytical solution for the fully developed flow can be obtained.

Consequently, the study of electroosmotic flow in a single channel can be used to test the numerical code developed here.

In this chapter, the electroosmotic flow in a straight

channel formed by two

parallel plates is studied. The velocity and pressure profiles will be obtained for a straight channel with a portion of its wall having different surface potentials. The mechanism of auxiliary electroosmotic pumping in CE will also be considered.

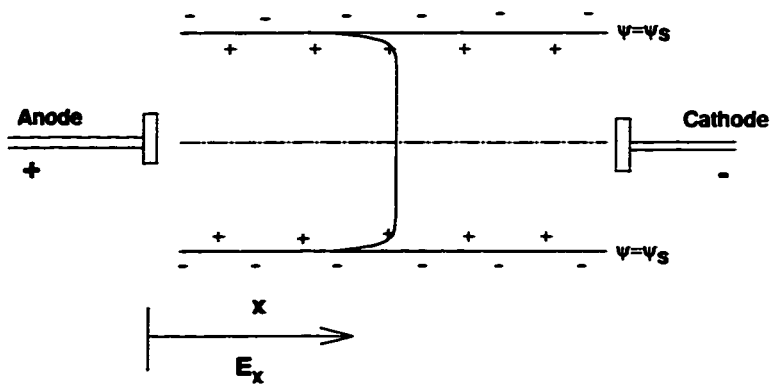


Figure 4.1 Electroosmotic flow in capillary channel.

The problem considered here is sketched in figure 4.1. The walls are negatively charged with a surface potential of ζ . The fluid enters the channel with either a flat profile or a fully developed velocity profile. The parameters involved are κa , ζ , and the electric field strength E_x . The effect of varying these parameters on the flow will be studied.

4.2 Fully Developed and Developing Electroosmotic Flow in a Capillary Channel

4.2.1 Fully Developed Electroosmotic Flow

For small surface potentials ($\zeta < 25$ mV), the Debye-Hückel approximation can be invoked. For fully developed flow, equation (2.42) leads to,

$$-P_x = \frac{d^2U}{dY^2} - E_x \zeta \frac{\cosh(\kappa a Y)}{\cosh(\kappa a)} \quad (4.1)$$

where $P_x = -dP/dX$, $E_x = -d\Phi/dX$. The boundary conditions are:

$$\frac{\partial U}{\partial Y} = 0 \quad \text{at } Y = 0 \quad (4.2)$$

$$U = 0 \quad \text{at } Y = \pm 1 \quad (4.3)$$

The velocity field U can be obtained by solving equation (4.1), leading to,

$$U = -\frac{1}{2} P_x (Y^2 - 1) - \frac{E_x \zeta}{(\kappa a)^2} \left[1 - \frac{\cosh(\kappa a Y)}{\cosh(\kappa a)} \right] \quad (4.4)$$

The right hand side of equation (4.4) consists of two terms, the first term is the Poiseuille flow due to a constant pressure gradient and the second term is the electrokinetic flow due to an applied electric field, E_x .

The average velocity in the channel can be obtained by integrating equation (4.4) from $Y=-1$ to $Y=1$. It is given by,

$$\bar{U} = \frac{1}{3} P_x - \frac{E_x \zeta}{(\kappa a)^2} \left[1 - \frac{1}{\kappa a} \tanh(\kappa a) \right] \quad (4.5)$$

Figure (4.2) compares the velocity of the fully-developed electroosmotic flow obtained by the present numerical code with equation (4.4). It shows that the present code agrees well with the analytical solution.

The dimensional velocity can be obtained from equation (4.4) for a typical electrolyte solution with parameters, $\varepsilon=78.5$, $\varepsilon_0=8.85 \times 10^{-12} \text{ C}^2/\text{N m}^2$, $\mu=1.0 \times 10^{-3} \text{ (Pa.s)}$, $k=1.381 \times 10^{-23} \text{ J K}^{-1}$, $N_a=6.022 \times 10^{23} \text{ mol}^{-1}$, $T=293 \text{ K}$, $z=1$, $e=1.602 \times 10^{-19} \text{ C}$; channel half width, $a=5 \mu\text{m}=5 \times 10^{-6} \text{ m}$. The expression for κa is given by equation (2.15),

$$\kappa a = \left(\frac{2n_\infty z^2 e^2}{\varepsilon \varepsilon_0 k T} \right)^{\frac{1}{2}} a \quad (4.6)$$

where n_∞ is the ionic number concentration, $n_\infty = N_a \times C$, C is the molar concentration of the electrolyte solution in mol/m^3 . Substituting the above data into equation (4-6) leads to,

$$\kappa = 1.0486 \times 10^8 \sqrt{C} \quad (\text{m}^{-1}) \quad (4.7)$$

Substitution of the dimensionless parameters into equation(4.4) leads to,

$$u = -\frac{a^2}{2\mu} p_x \left[\left(\frac{y}{a} \right)^2 - 1 \right] + \frac{\varepsilon \varepsilon_0 \psi_s \phi_x}{\mu} \left[1 - \frac{\cosh(\kappa y)}{\cosh(\kappa a)} \right] \quad (4.8)$$

For large κa ($\gg 1$), the Helmholtz-Smoluchowski equation gives,

$$u_e = \mu_e \phi_x \quad (4.9)$$

where μ_e is the electroosmotic mobility given by,

$$\mu_e = \frac{\varepsilon \varepsilon_0 \psi_s}{\mu} \quad (4.10)$$

$\langle u \rangle$ is defined as a characteristic velocity which is given by,

$$\langle u \rangle = \frac{2n_{\alpha}kTa}{\mu} = 24.365C \quad (\text{m/s}) \quad (4.11)$$

where C is concentration in mol/m^3 . Once the κa is determined the characteristic velocity can be calculated using equation(4.11). The dimensional velocity will be obtained using $u=U \times \langle u \rangle$ (m/s). Figure 4.3 shows how the velocity varies with κa . It can be seen that as $\kappa a \rightarrow \infty$, $u/u_e \rightarrow 1$, and at $\kappa a = 20$, $u/u_e = 0.95$ at $y=0$. For the convenience of computation, κa of 20 is chosen as a parameter in modelling.

A test of grid sensitivity to the numerical solution has been carried out by changing the grid size in both X and Y directions. Some calculations were carried out using 41×50 and 61×100 grids with different stretching parameters. In all the tests, the largest disagreement of the average velocity was smaller than two percent.

4.2.2 Developing Electroosmotic Flow

Consider electroosmotic flow of an electrolyte solution inside a parallel plate channel with an uniform parallel inlet axial velocity distribution. The pressures at both ends are of the same value. The entrance effect on the electroosmotic flow can be obtained using the present numerical code. Figure 4.4 shows the pressure profile along the centerline of the channel for different zeta potential values. One can observe that the centerline pressure undergoes a sharp drop at the entrance mouth. This is because when the electrolyte enters the capillary channel there will exist a transverse pressure distribution due to the electric double layer (see equation (2.47)). The pressure then gradually recovers to the outlet pressure, which is the same as the inlet pressure. The positive pressure gradient means that the pressure force is against electroosmotic flow, which is driven by the electric force. Therefore the electroosmotic flow is reduced due to the entrance effect for a short channel (in this case $L=10$). The velocity profiles are shown in figure 4.5. Clearly the net flow is due to both the electroosmotic flow and the pressure driven flow (as shown in equation (4.4)). For higher zeta potential, the entrance effect is more significant due to higher electroosmotic flow.

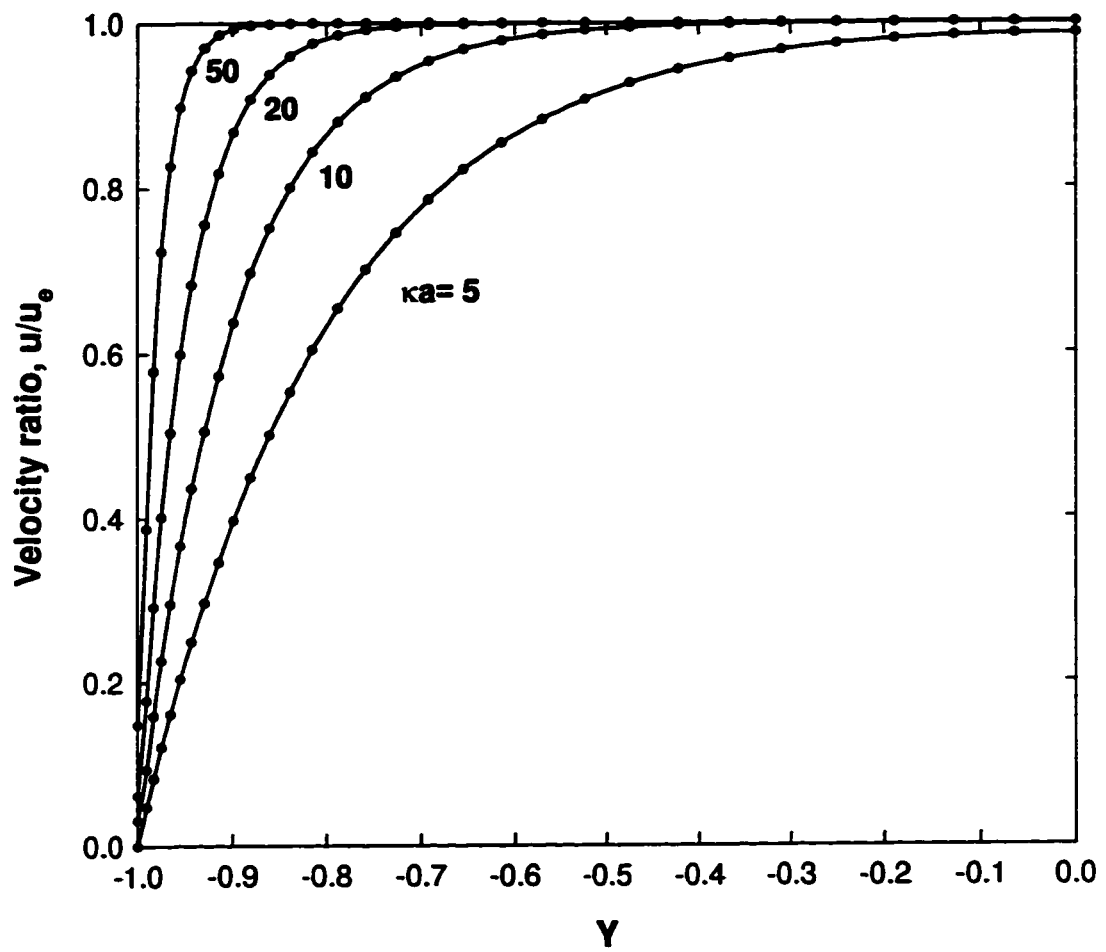


Figure 4.2 Axial velocity profile for different κa and comparison of numerical solutions (.) with analytical solution (solid line) for $\zeta = -1.0$.

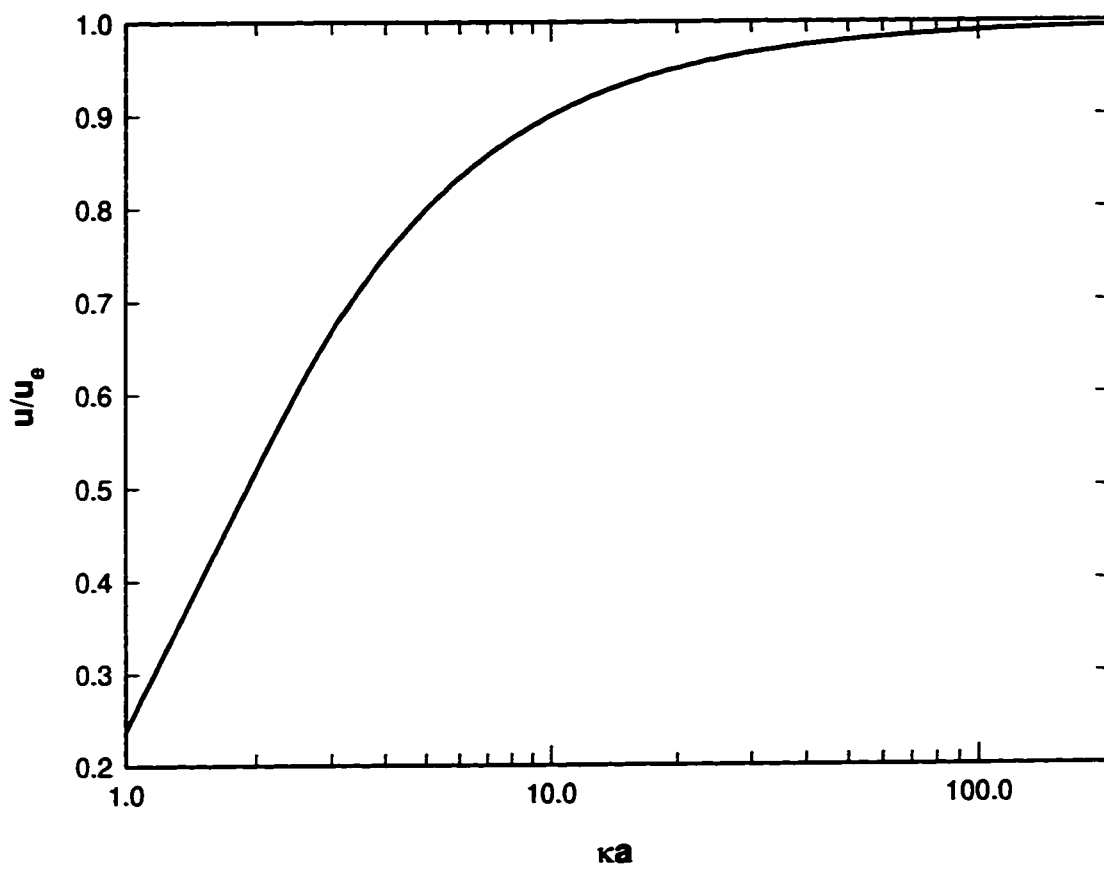


Figure 4.3 Variation of the dimensionless axial velocity ratio with ka .

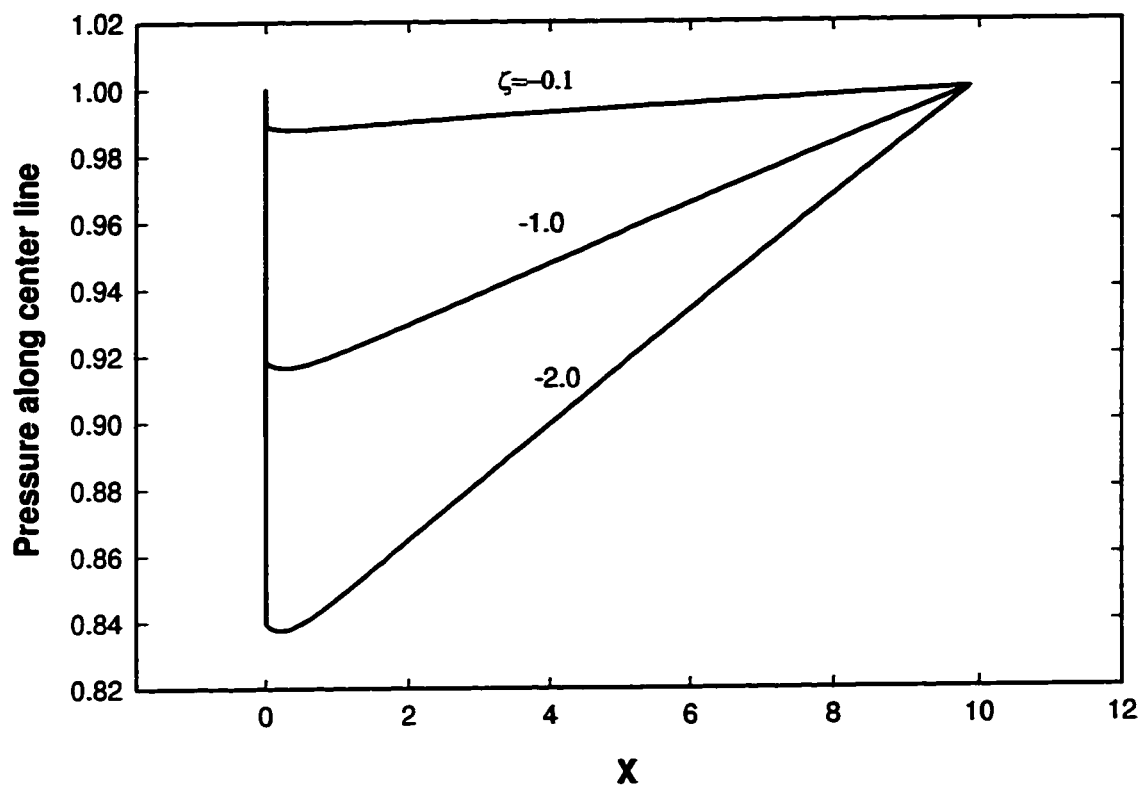


Figure 4.4 The pressure profiles along the centerline of the channel for different zeta potential values ($\kappa a=20$, $L=10$, $E_x=10$)

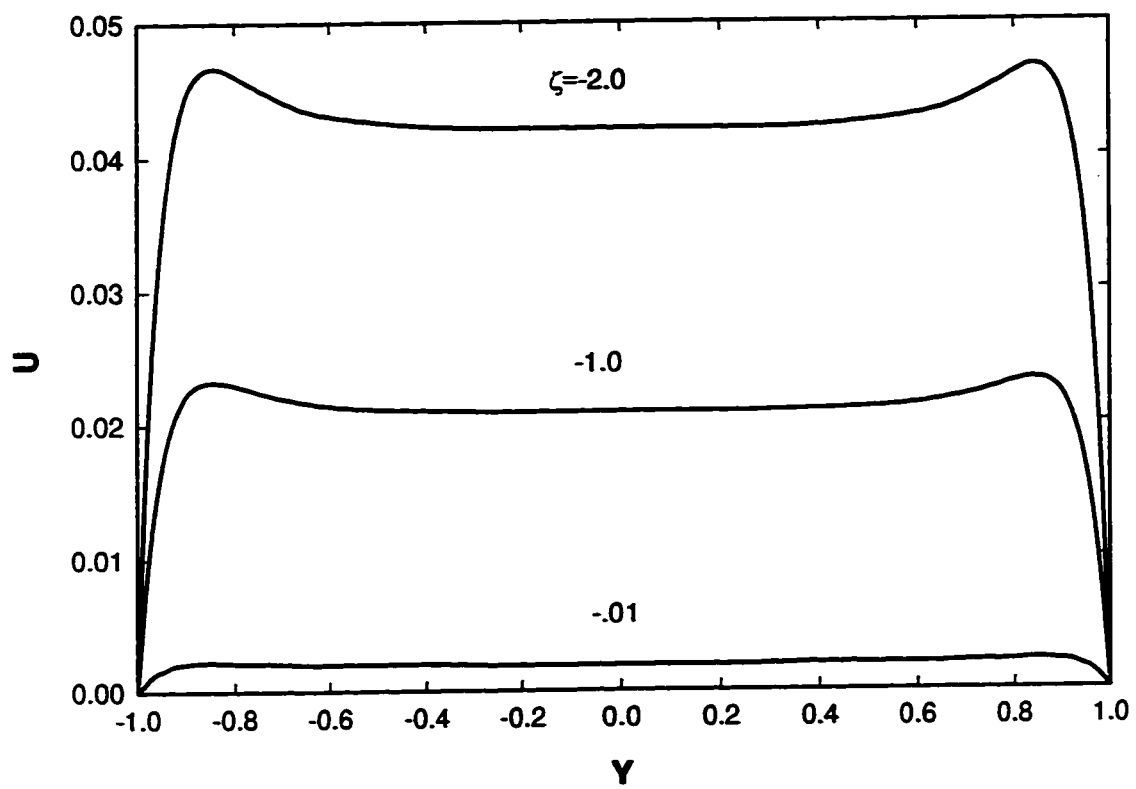


Figure 4.5 Developed velocity profiles in the channel for different zeta potential values ($\kappa a = 20$, $L = 10$, $E_x = 10$)

4.3 Controlling of Electroosmotic flow in Capillary Electrophoresis

4.3.1 Introduction

In capillary electrophoresis, it is well known that, concomitant to the electrophoretic migration, the bulk flow of the solution, i.e. electroosmosis, is dependent on the characteristics of the capillary surface as well as on the composition of the conducting medium (electrolyte). The electroosmotic flow has a substantial influence on the residence time of the analyte in the capillary. The understanding and control of electroosmotic flow has an important implication on the design of electrophoretic separation devices. In recent years, several strategies have been developed to control the electroosmotic flow. The first effective means is to alter the chemical and physical properties of the buffer solution. Changes in the pH and ionic strength of the buffer, and in the type and concentration of the inert electrolyte or organic additives [8,9], as well as changes in solvent viscosity, dielectric constant, and temperature, have been shown to affect electroosmotic flow. Another simple approach to affect the electroosmotic flow is to change the chemical composition of the capillary material by physical coating and chemical derivatization methods[7]. As well, direct control of the electroosmotic flow in capillary electrophoresis by using a radial electric potential gradient across the capillary wall [10-14] has been demonstrated. The applied radial electric potential gradient can affect the polarity and magnitude of the surface potential at the capillary-solution interface and therefore would control the direction and the flow rate of the electroosmotic flow.

Numerical modelling the control of electroosmotic flow in a straight capillary channel is investigated in this chapter. The flow control in multiple

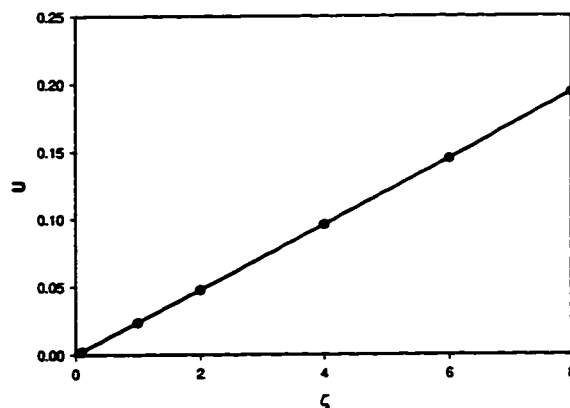


Figure 4.6 Dimensionless average velocity versus ζ potential ($\kappa a=20$, $E_x=10$).

channels within a chip will be discussed in the next chapter.

4.3.2 Effect of Surface Potential on Electroosmotic Flow

Figure 4.6 shows the variation of electroosmotic flow with zeta potential. It is shown that the velocity is linearly dependent on the surface potential. The surface potential can be easily changed by varying the solution pH.

4.3.3 The Control of Flow by Changing Surface Potential in a Portion of Capillary Wall

The use of external radial potential for controlling the electroosmotic flow can be modelled by varying the surface potential within a given position of the capillary's walls. This is possible as it was shown that the radial potential affects the zeta potential only in those portions of the capillary directly inward of the external potential field [13].

Figure 4.7 shows the arrangement used in the control of electroosmotic flow by externally applying a radial potential across a portion of a capillary [11]. Now consider a capillary channel with a portion of the wall having zero surface potential. The velocity and pressure profiles were obtained using the present numerical code. Figure 4.8 shows the velocity and the pressure profiles for the case in which the surface potential on the middle half of the wall is zero. It is observed that the velocity profile halfway within the channel becomes parabolic. This is simply due to the fact that in this region the driving force is the pressure gradient alone. Setting the surface potential to zero can be considered as coating a channel wall with a material having zero surface potential, or defect in the channel wall.

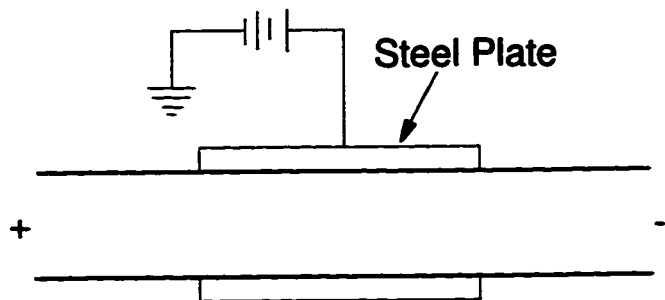


Figure 4.7 Schematic of the apparatus used to control electroosmotic flow by imposing radial potential[11].

Figure 4.9 shows the dimensionless average velocity variation with the length of the imperfect wall ($\zeta'=0$). One can observe that the flow rate is linearly dependent on the length of imperfect wall. This is to be expected. The transport equations for creeping flow show that the velocity is linearly dependent on the electric force, which is proportional to the length of the perfect wall (having non-zero surface potential).

Figure 4.10 shows the average velocity across the channel versus the surface potential of the middle portion of the capillary channel. It is demonstrated that when $\zeta=\zeta'$, the flow is solely due to electroosmotic effect. When $\zeta=-\zeta'$, there is no net flow in the channel. The flow will either be inhibited or enhanced depending on the values of ζ' and ζ .

Figure 4.11 shows the velocity and pressure profiles for the case of $\zeta=-1.0$ and $\zeta'=1.5$. It shows that the flow in the middle portion of the channel is inhibited and a positive pressure gradient exists. However, the flow in either side of the channel is enhanced. This can be observed by the velocity profiles in figure 4.11.

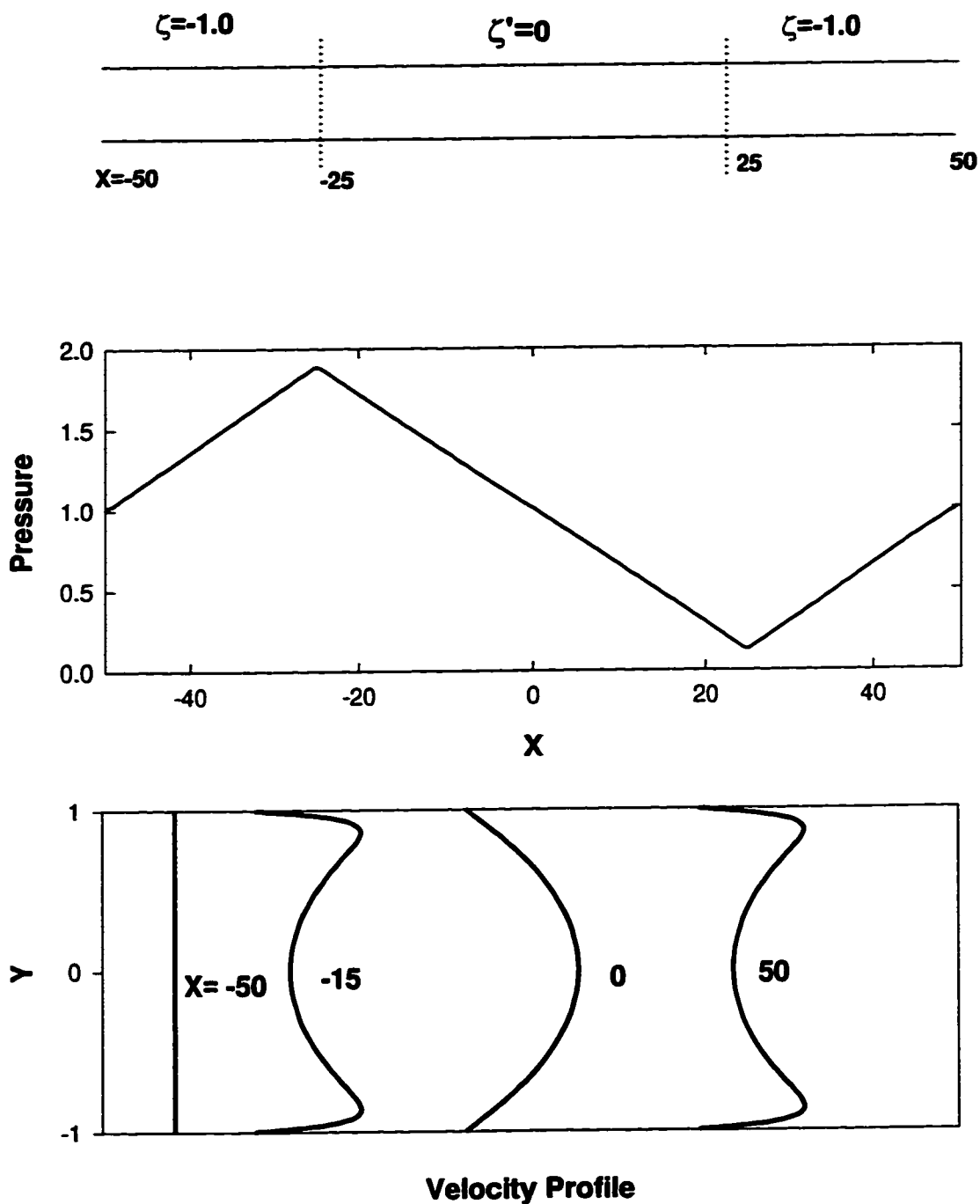


Figure 4.8 Velocity and pressure profiles in a capillary channel having the surface potential set to zero within the middle half of the channel for $\kappa a = 20$, $E_x = 10$, $L = 100$.

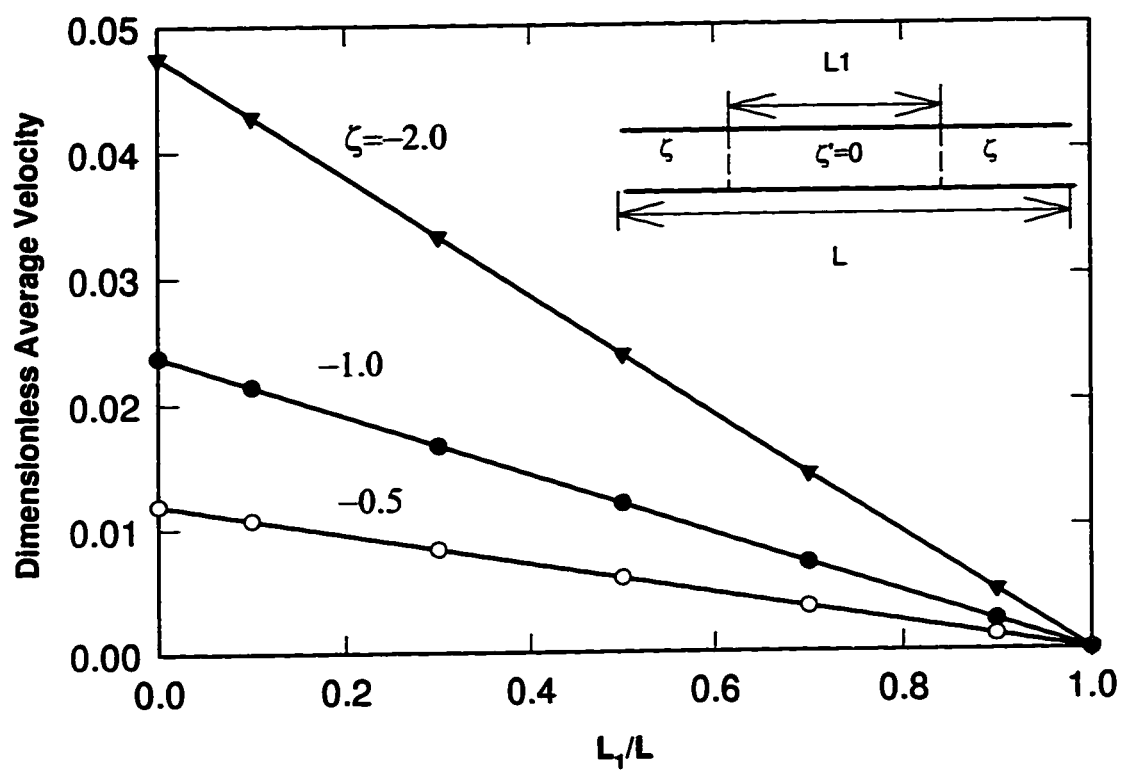


Figure 4.9 Variation of the dimensionless average velocity with the fraction of imperfect wall for different surface potentials ($\kappa a=20$, $E_x=10$, $L=100$).

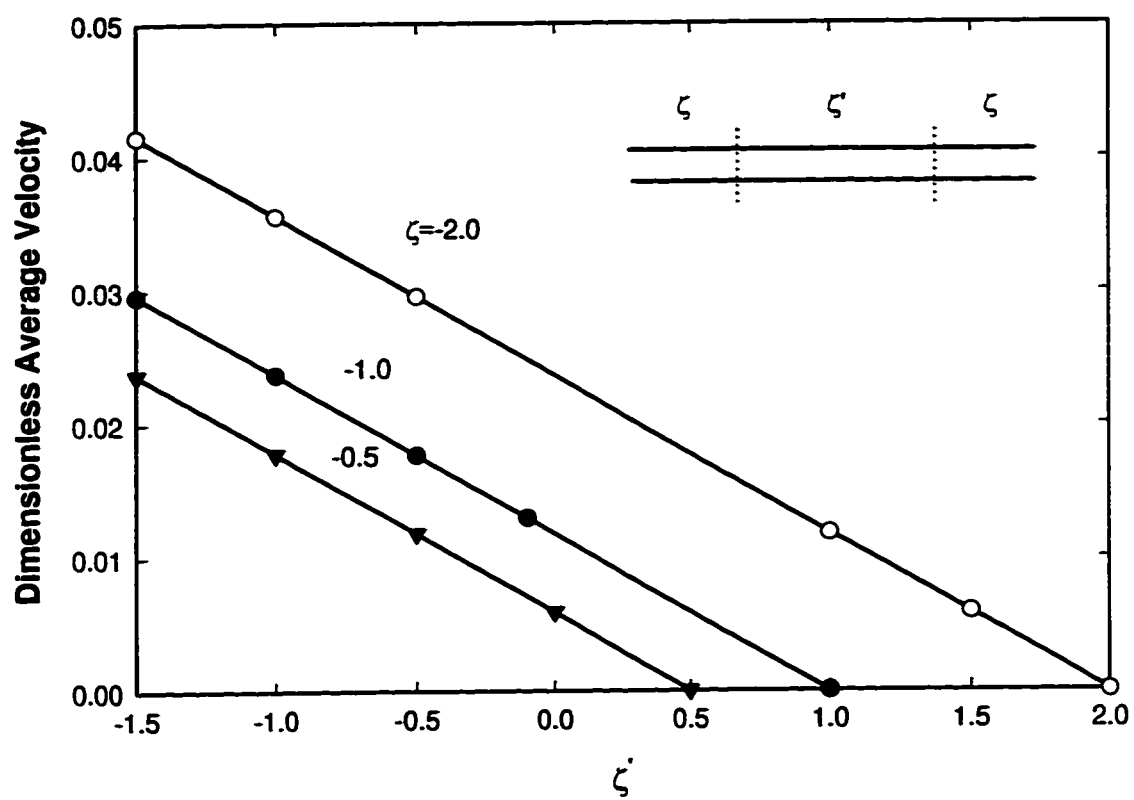


Figure 4.10 Variation of the dimensionless average velocity with the middle channel wall potential ζ' ($\kappa a=20$, $E_X=10$, $L=100$, $L'=50$).

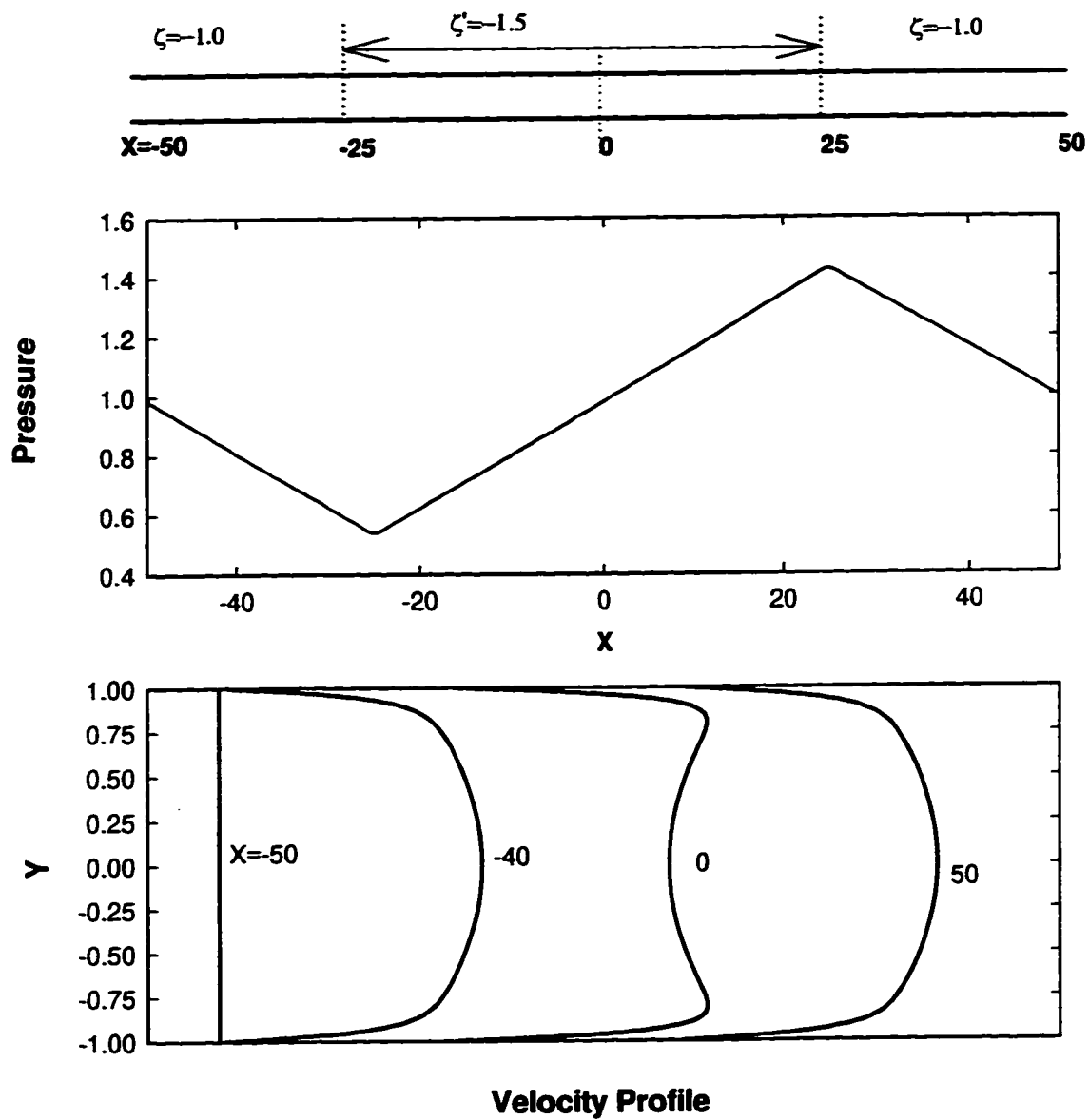


Figure 4.11 Velocity and pressure profiles in capillary channel with different ζ potential along the channel, the total length of capillary $L=100$, the middle part $L'=50$.

4.3.4 Control of Flow by Auxiliary Electroosmotic Pumping

The electroosmotic means to control electroosmosis has been developed with the application of an auxiliary capillary[15]. A conductive membrane can be used to connect a second capillary to the primary capillary, the membrane serving as the common ground for both high voltage sources. The direction and magnitude of the field applied to the second capillary controls the bulk flow in the first capillary. It may be augmented, inhibited or be unaffected by the pumping action exerted by the second capillary.

Consider the arrangement schematically shown in Figure 4.12. Capillary C1 is connected to a source vial housing a high voltage electrode HV1 and to a grounding joint J. Here no fluid can exit at point J, thus, there is no equilibration

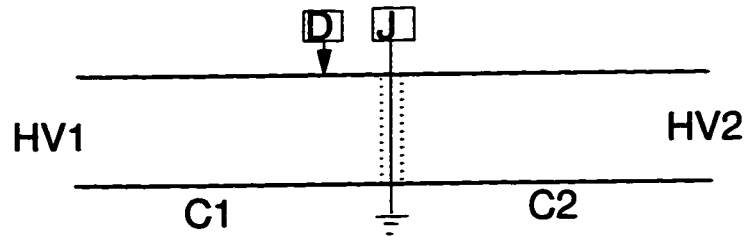


Figure 4.12 Auxiliary electroosmotic pumping scheme.

with atmospheric pressure. The joint J is connected to capillary C2, hereinafter referred to as the pump capillary. C2 terminates in an electrolyte reservoir, housing a second high voltage source electrode HV2. J is the common ground. When HV1 and HV2 are opposite in sign and the electric field strength in C2 is larger than that in C1, the electroosmotic flow generated in C2 augments the flow in C1. The flow in one channel will inhibit the other when the sign of the potential of both reservoirs is the same. It would be expected that a pressure gradient will be induced along the channel if the potential gradients in the two capillaries are different. Here the flow should include both electroosmotic and hydrostatic contributions.

Figure 4.13 shows the velocity and pressure profile along the capillary channel for the case of $\Phi_1=1700$, $\Phi_2=3000$. Φ_1 and Φ_2 are the dimensionless electric potential applied at inlet and outlet, respectively. In this case $\kappa a=100$, $\zeta=-1.0$. The boundary

conditions for flow are, uniform inlet and fully developed outlet. The plot shows that the flow in the capillary C1 is enhanced by the flow in the auxiliary capillary C2. Therefore, the velocity profile in C1 is pulled out and the flow in C2 is held back. The velocity profiles in both capillaries are not flat because of the hydrodynamic force, this may lead to band broadening in CE and affect the efficiency of electrophoresis separation due to Taylor dispersion[49]. Figure 4.14 shows the variation of the dimensionless average velocity with the dimensionless electric potential applied at the outlet of capillary C2 while the potential at the inlet of capillary C1 is kept the same value. The average velocities for different surface potentials decrease with the electric potential at outlet Φ_2 . For all cases illustrated in figure 4.14, the net flow is zero when the potential at outlet (Φ_2) is equal to that at inlet (Φ_1). This is because the electric field strength across both channels are opposite in direction and their magnitudes are same, therefore there is no net flow across the channels.

In conclusion, the velocity profile resulting from controlling the electroosmotic flow is shown to be a non plug like profile. The fluid flow consists of both Poiseuille and electroosmotic flow, the pressure driven Poiseuille flow is induced due to the differing electroosmotic flow along the capillary channel. The effect of this velocity profile on the efficiency (dispersion coefficient or plate height HETP) should be considered during the flow controlling process[46,47]. It should be recalled that a plug velocity profile leads to a zero axial dispersion.

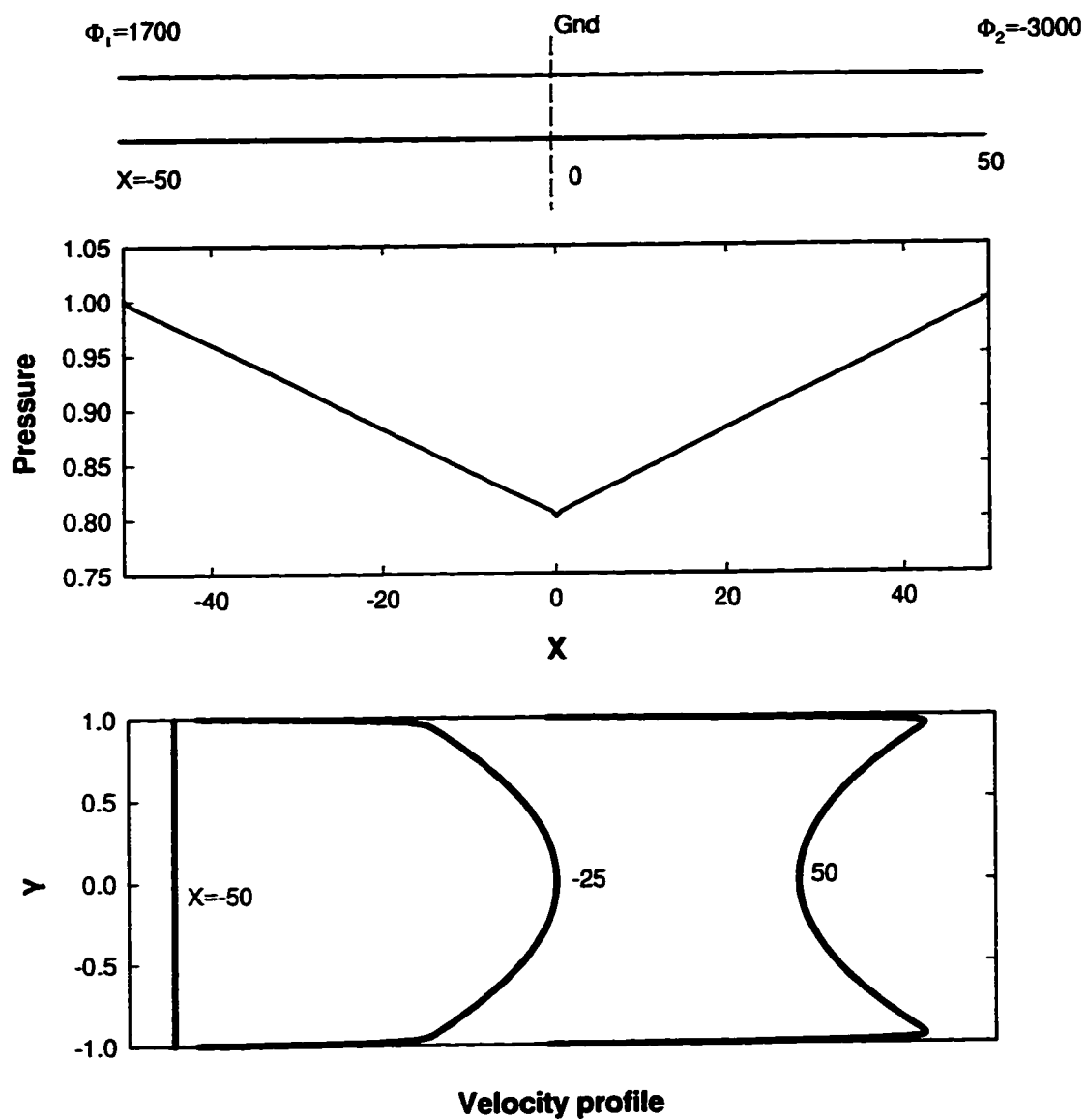


Figure 4.13 Velocity and pressure profiles in a capillary channel with different electric field in the main capillary C1 and auxiliary capillary C2 ($\kappa a=100$, $\zeta=-1.0$).

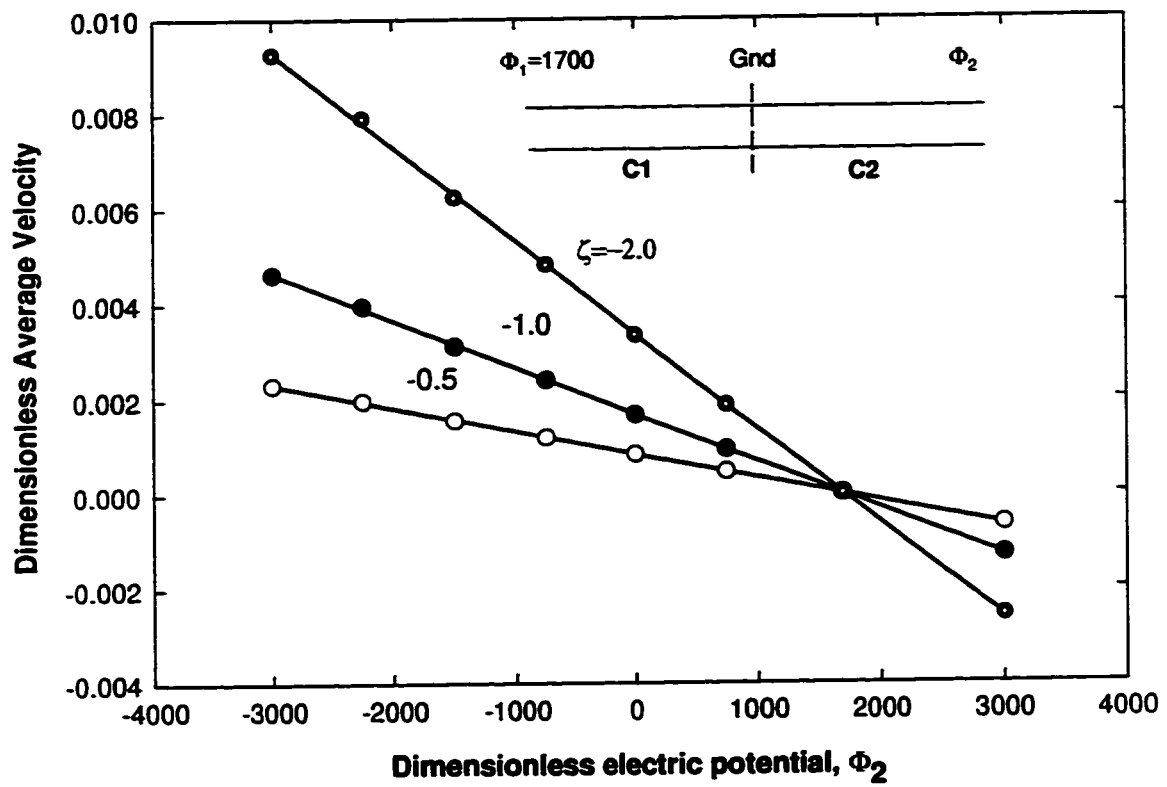


Figure 4.14 Variation of the dimensionless average velocity with the electric potential on the right reservoir for different ζ potential and fixed Φ_1 ($\kappa a = 100$, $L = 100$).

Chapter 5

Electroosmotic Flow in T-shaped Capillary Channels

5.1 Introduction

In chapter 4, the electroosmotic flow and its control in a simple straight channel were investigated. The factors which affect the electroosmotic flow, such as κa , surface potential and electric field strength were considered. The results showed that both electrokinetics and pressure can be used for the control of electroosmotic flow in a capillary electrophoresis. From these results one can expect that the hydrodynamic effects can be very important for a manifold channel system in which both sample injector and electrophoresis system are integrated together. The experimental results [18] have shown qualitatively that sample leakage from a side channel and electrolyte mixing at an intersection exist during the electrophoresis process. The control of leakage at an intersection can be achieved by controlling the potential of each connecting channel simultaneously.

The numerical study of the electroosmotic flow is carried out in a T-shaped capillary channel with a side channel which either is left floating or has a fixed potential. The governing equations were described in chapter 2. The calculation domain consists of the main channel, the side channel and three ends connected to their respective

reservoirs.

5.2 Liquid Leakage From a Floating Side Channel

It has been shown that if the potential of the side channel is left floating while a voltage is applied to cause flow in the main channel, there will be leakage of solution from the side channel, thus, contaminating the main channel [16-20]. Quantitative study of the leakage can be obtained using mathematical modelling of the electrokinetic flow in simple T-shaped capillary channels.

5.2.1 Effect of the Channel Length on the Leakage

Consider a T-shaped channel as shown in figure 5.1. L_s , L_m are the length of side channel and main channel, respectively. The side channel is located in the middle of the main channel and the electric potential at the side reservoir is left floating (FL), the ratio of the length of the side channel to the main channel is kept the same at $L_s/L_m=4/5$. The dimensionless potential gradient in the main channel is maintained at $E_x=10$. Here, $\Phi_2=0$, $E_x=(\Phi_1-\Phi_2)/L_m$, and Φ_3 is left floating.

The variation of the average velocities in both the main channel and the side channel with the channel length is shown in figure 5.2, for $L_m=100-1500$, $\kappa a=20$, $E_x=10$, and $\zeta=\zeta'=-1.0$. It

clearly shows a significant decrease in leakage from the side channel when both channel lengths are increased, even though the L_s/L_m ratio remains constant. The ratio

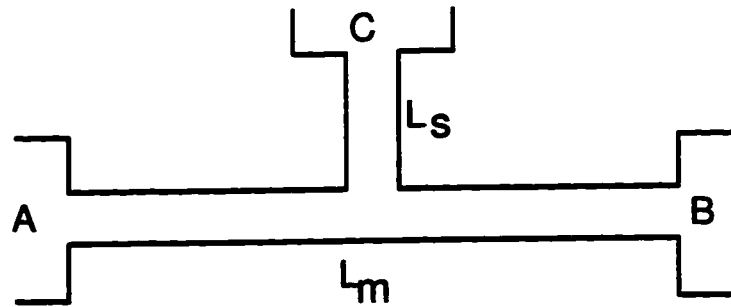


Figure 5.1 Schematic of connecting channels, A, B and C are three reservoirs. L_m and L_s are the lengths of the main and the side channel, respectively.

of leakage out of the floating side channel ranges from 14.56% (for $L_m=100$) to 1.13% (for $L_m=1500$), indicating that there is less leakage for a longer side channel.

As indicated in figure 5.3, when the side channel is left floating, the electric potential is relatively constant along the side channel. That means that there is no electric force to drive the electrolyte to flow along the side channel. The flow must be driven by a pressure gradient.

Figure 5.4 may help to understand this phenomenon. It shows the pressure profile along the center line of the main channel for different channel lengths. The center line pressure undergoes a sharp drop at the entrance mouth as observed in straight channels. This is because when the electrolyte enters the capillary channel there exists a transverse pressure distribution due to the electric double layer (See equation (2-47)). The pressure then gradually recovers to the outlet pressure, which is the same as the inlet pressure. The plot also shows that the pressure at the intersection varies little from 0.35 (for $L_m=100$) to 0.10 ($L_m=1500$). However, the pressure gradient along the side channel decreases significantly when the channel length is increased. This leads to a decrease in the leakage rate. As the driving force is solely due to the pressure gradient, the velocity profile is expected to be parabolic in the side channel. The velocity profiles both in the main channel and in the side channel are shown in figure 5.5 for $\kappa a=100$, $\zeta=\zeta'=-1.0$, $L_m=1000$, $L_s=800$, $E_x=10$. The fluid enters the main channel with a flat profile and develops along the channel due to the effect of both the electric force and the hydrodynamic force. Therefore, its fully-developed profile is the superposition of the electroosmotic flow and Poiseuille flow.

Figure 5.5 (b) shows the velocity development along the side channel. It shows that both fluid inflow and outflow occur at the intersection area because of the convective effect. However, the outflow is larger than the inflow such that the net flow results in leakage from the side channel to the main channel. As expected, the fully developed velocity profile in the side channel is parabolic. The penetration length is about 1.5 times the channel width.

Figure 5.6 shows the streamlines at the intersection for $L_m=100$, $L_s=80$. It illustrates that some of the fluid flows up into the side channel and then runs back to the

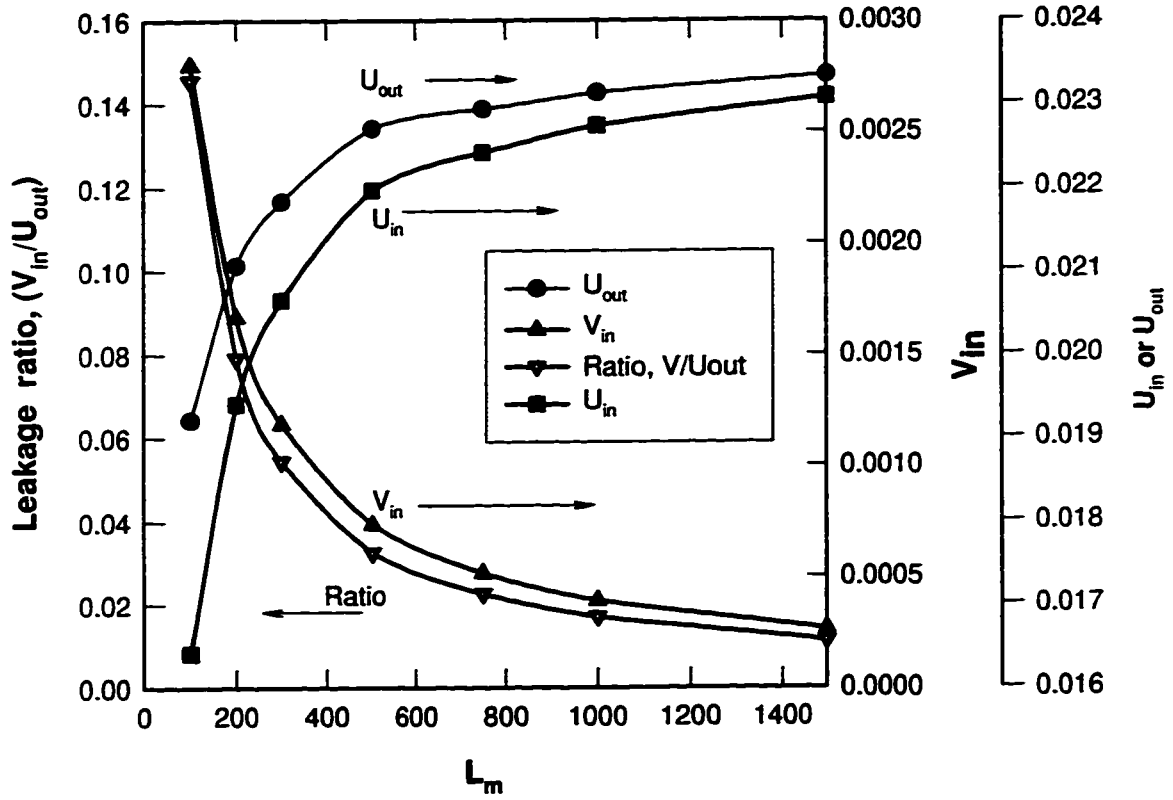
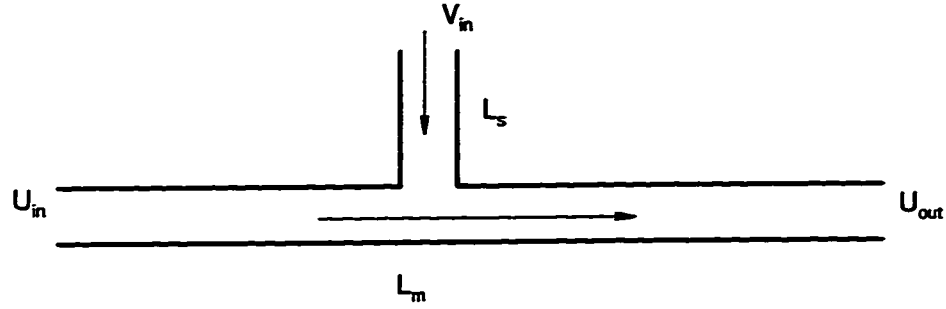


Figure 5.2. Variation of dimensionless average velocity in the channels with the length of channels for $\kappa a=20$, $\zeta=\zeta'=-1.0$, $E_x=10$, $L_s/L_m=4/5$, $\Phi_1=E_x L_m$, $\Phi_2=0$, Φ_3 is floating.

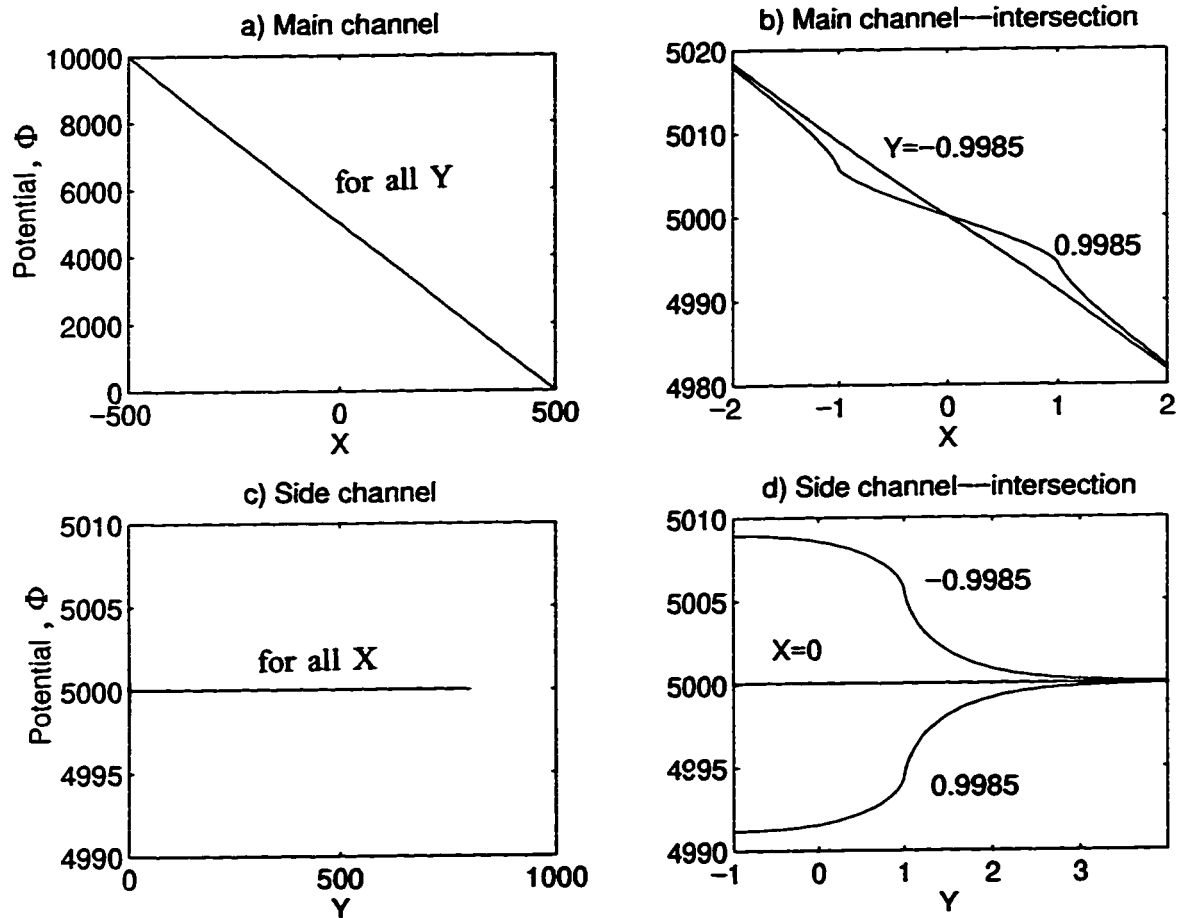


Figure 5.3. External electric potential distributions in the channels for $L_m=1000$, $L_s=800$, $\Phi_1=10000$, $\Phi_2=0$, Φ_3 is floating

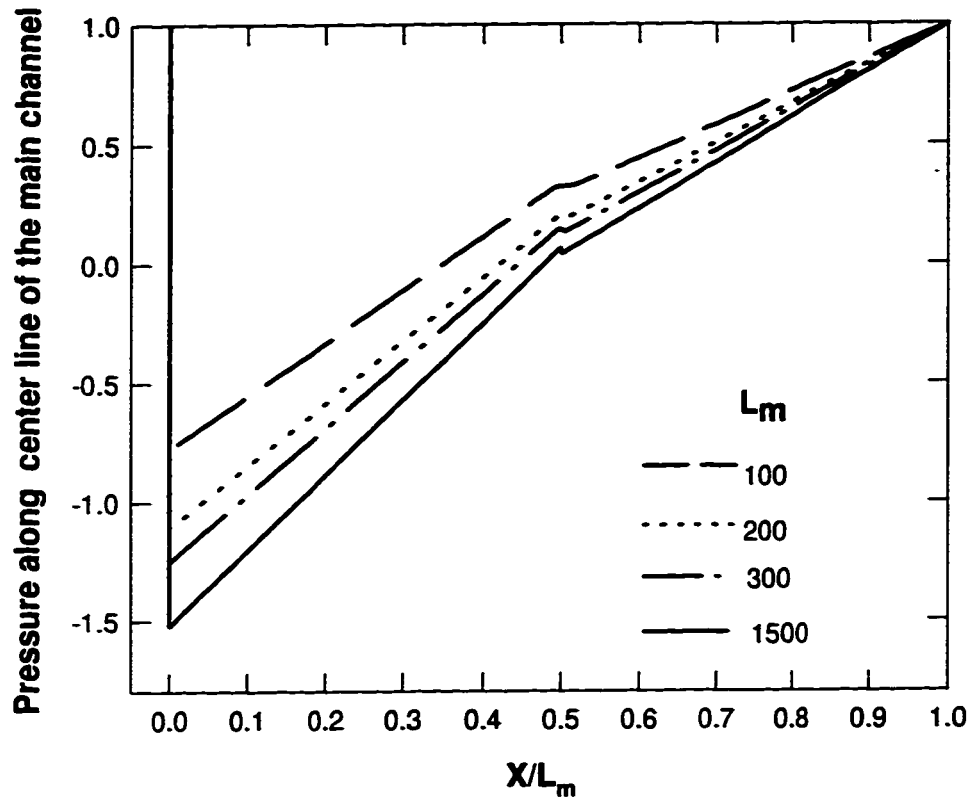
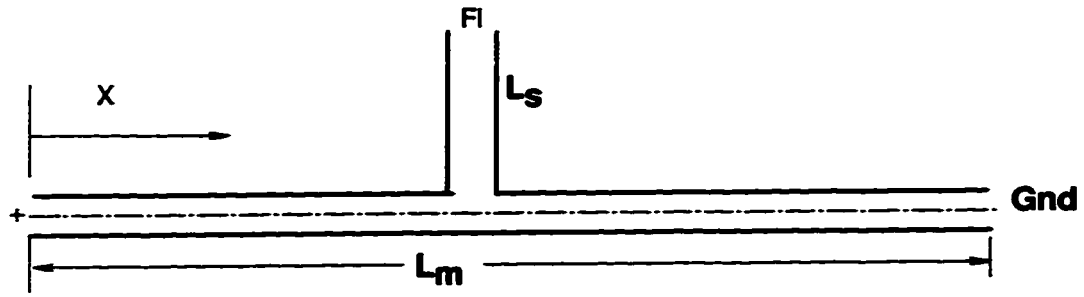


Figure 5.4. Pressure distribution along the center line of the main channel for different channel lengths for $\kappa a=20$, $\zeta=\zeta'=-1.0$, $E_x=10$, $L_s/L_m=4/5$, $\Phi_1=E_x L_m$, $\Phi_2=0$, Φ_3 is floating.

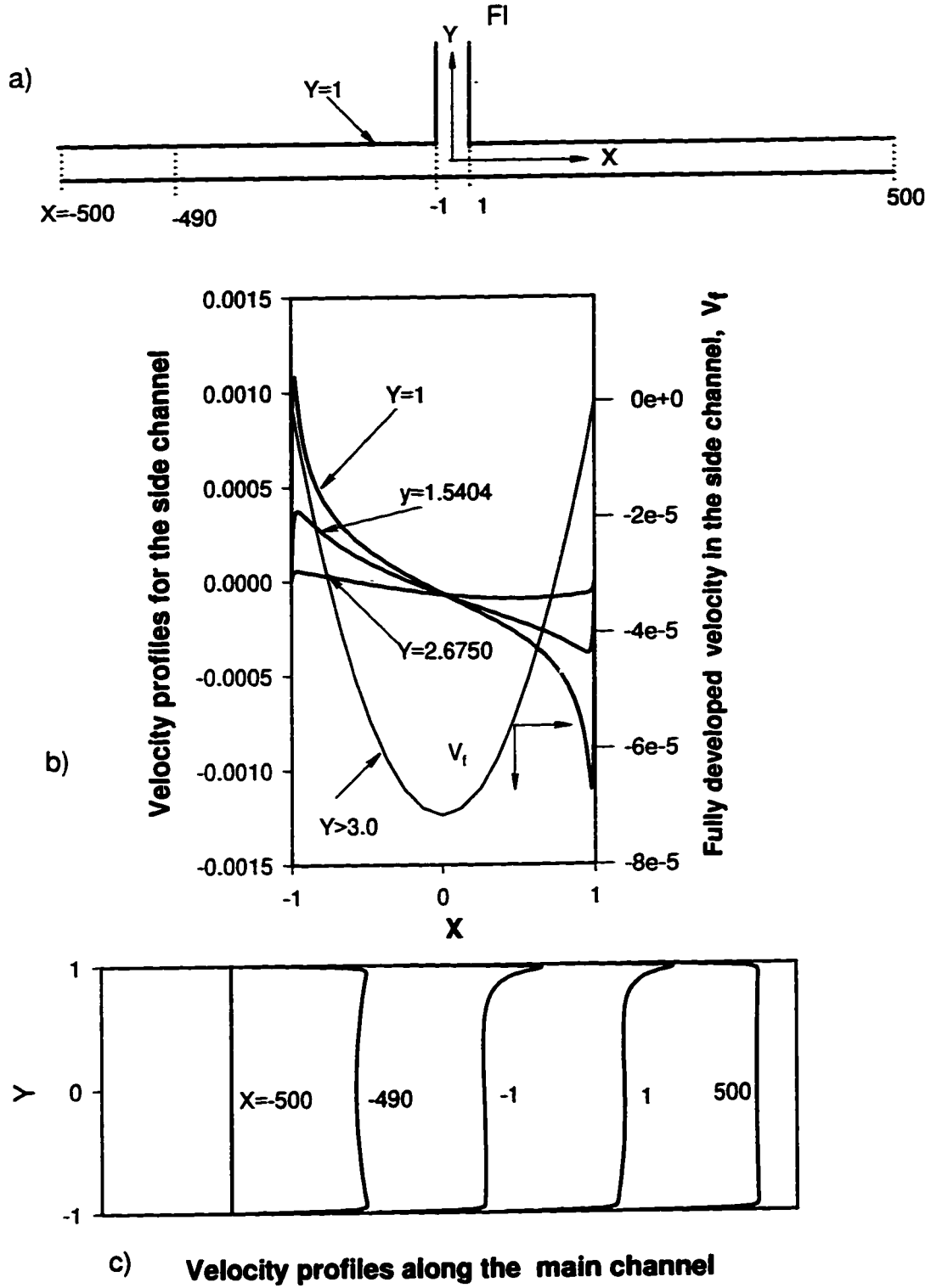


Figure 5.5. Velocity profile at different sections of the channels for $L_m=1000$, $L_s=800$, $\kappa a=100$, $\zeta=\zeta'=-1.0$, $\Phi_1=10000$, $\Phi_2=0$, Φ_3 is floating

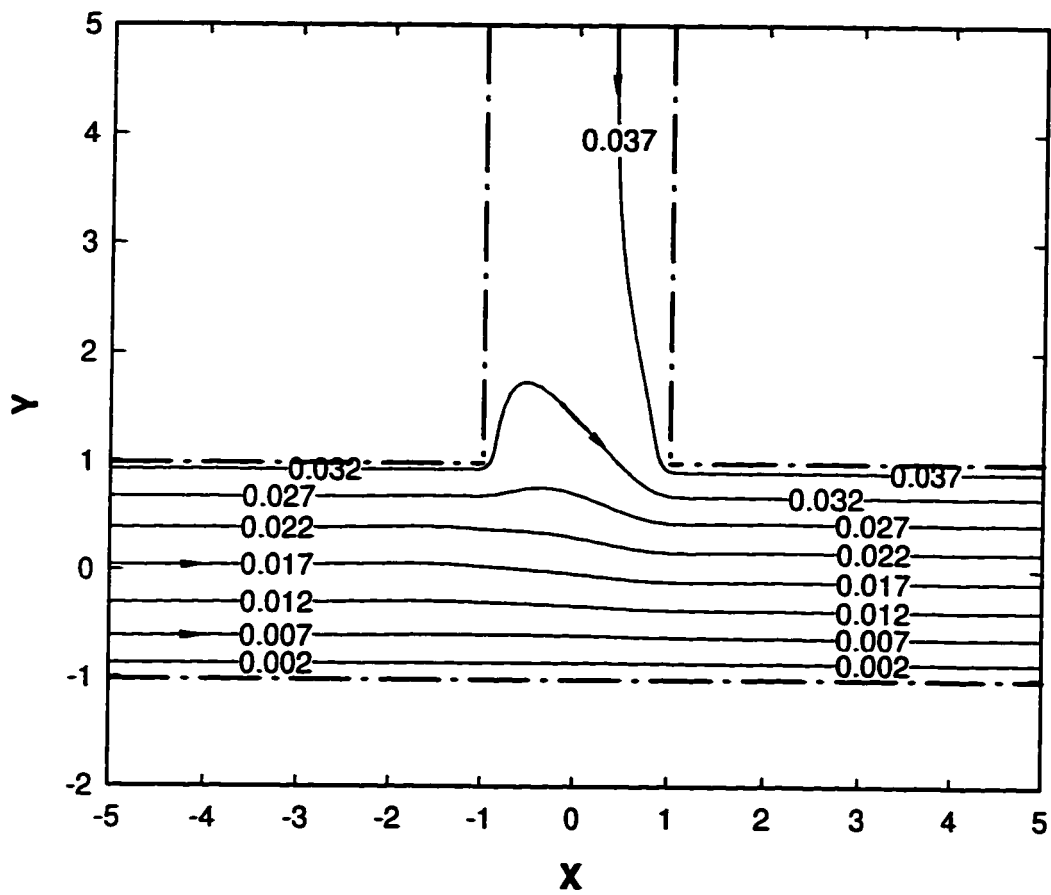


Figure 5.6. Streamlines at intersection region for $L_m=100$, $L_s=80$, $\zeta=\zeta'=-1.0$, $\kappa a=20$, $\Phi_1=1000$, $\Phi_2=0$, Φ_3 is floating.

main channel. The numbers indicated at the streamline of figure 5.6 represent the values of the stream function. The value of stream function is constant along each streamline. In steady flow the streamlines are the curves actually traced out by particles of the fluid. The stream function, $\Psi(x,y)$, is given by equations (5.1) and (5.2),

$$u = \frac{\partial \Psi}{\partial y} \quad (5.1)$$

$$v = -\frac{\partial \Psi}{\partial x} \quad (5.2)$$

On a streamline where $\Psi = \text{constant}$, we write,

$$d\Psi = \frac{\partial \Psi}{\partial x} dx + \frac{\partial \Psi}{\partial y} dy = 0 \quad (5.3)$$

Then the equation for streamline is given by

$$\frac{dy}{dx} = -\frac{\partial \Psi / \partial x}{\partial \Psi / \partial y} = \frac{v}{u} \quad (5.4)$$

One of the important property of the stream function is that the difference in the value of the stream function between two streamlines is the volumetric flow rate between the two streamlines (per unit depth). The stream function on the wall of $Y=-1$ is zero.

An experimental study due to Seiler et al.[18] demonstrated the same leakage phenomena in T-shaped channels. In figure 1.3, the buffer is driven through the main channel while the side channel of the dye sample is left floating. The photograph shows dye flow into the intersection from the side channel. The streamlines in figure 5.6 show the same profile as that of figure 1.3. The streamlines show that some liquid in the main channel flows into the side channel and then flows back to the main channel. This illustrates that the numerical model can be a useful guide for predicting the leakage phenomena in intersecting channels.

5.2.2 Effect of the Side Floating Channel Location

As illustrated in the previous section, when the side channel is left floating, the leakage flow from the side channel is solely due to hydrodynamic effects, i.e. the pressure gradient. When the side channel intersects the main channel at different positions, the flow will be different as the pressure varies with position along the main channel. The pressure variation along the main channel for different side channel locations is shown in figure 5.7. Figure 5.8 shows the variation of the dimensionless average velocity in each channel with the side channel location for $L_m=1000$, $L_s=800$, $\kappa a=20$, $\Phi_1=10000$, $\Phi_2=0$, Φ_3 is floating, $\zeta=-\zeta'=1.0$. As the pressure difference between the intersection point and the inlet of the side channel decreases for increasing L_1/L_m values, i.e. the side channel location is closer to the main channel outlet, one would expect less leakage for increasing L_1/L_m values. This is clearly observed in figure 5.8 where it is shown that the average velocity in the side channel decreases with L_1/L_m . The total flow in the main channel, U_{out} remains nearly constant.

5.2.3 Effect of the Side Floating Channel Length

Figures 5-9 and 5-10 illustrate the effect of the length of the side channel when the length of main channel is maintained at the same value ($L_m=1000$). Figure 5-10 shows that the leakage from the side channel decreases with increasing side channel length. This means that the longer the side channel is, the more the resistance to the fluid flow. The ratio of leakage out of the side channel to the flow out of the main channel ranges from 3.87% for $L_s=200$ to 1.69% for $L_s=800$. The pressure at the intersection region does not vary much with an increase in the length of the side channel (figure 5.9). Therefore, the pressure difference between the side reservoir and the intersection will change little. However, the driving force, or the pressure gradient, will decrease significantly. Therefore, leakage decreases with the side channel length.

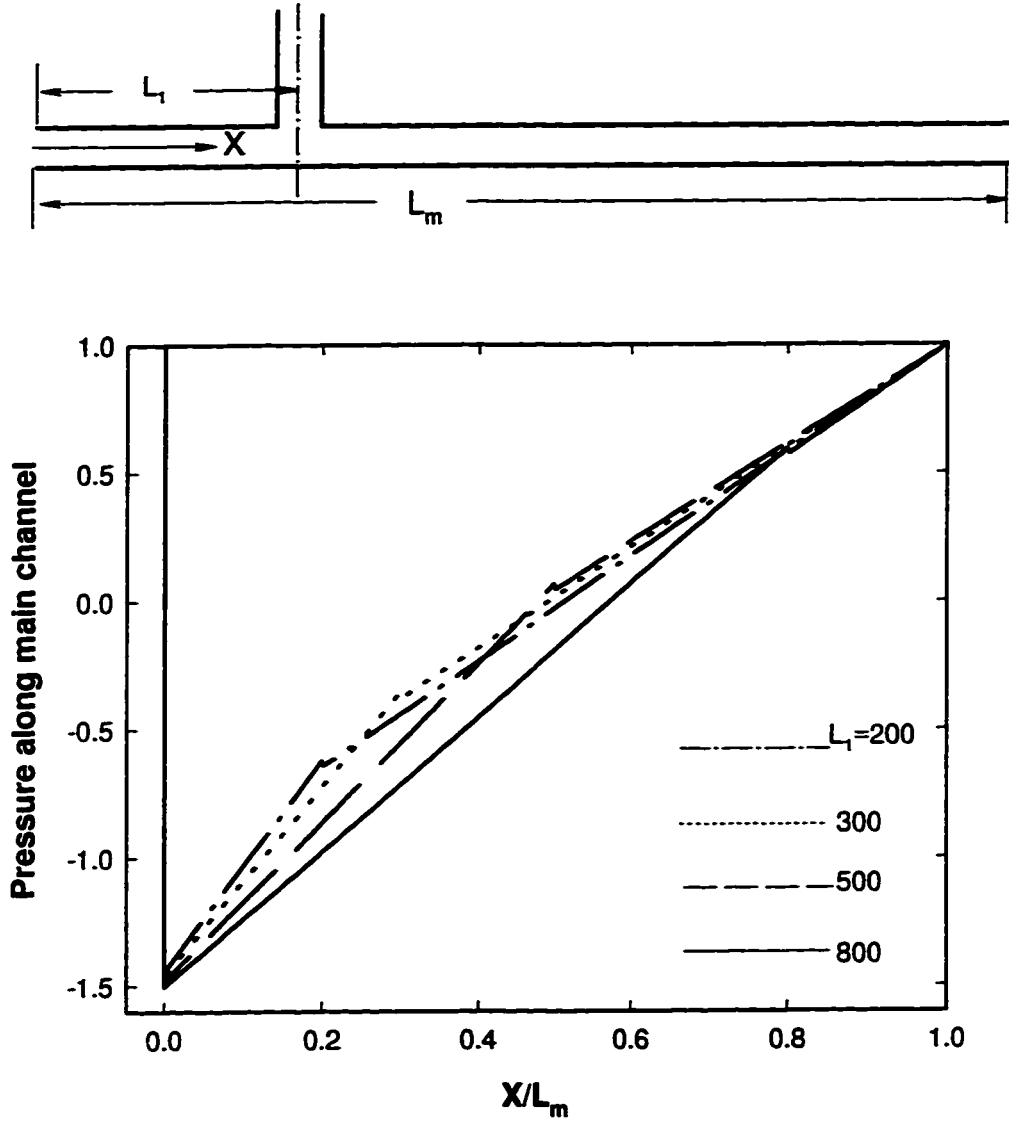


Figure 5.7. Pressure profile along the center line of the main channel for different locations of the side channel, $\kappa a=20$, $\zeta=\zeta'=-1.0$, $L_m=1000$, $L_s=800$, $\Phi_1=10000$, $\Phi_2=0$, Φ_3 is floating.

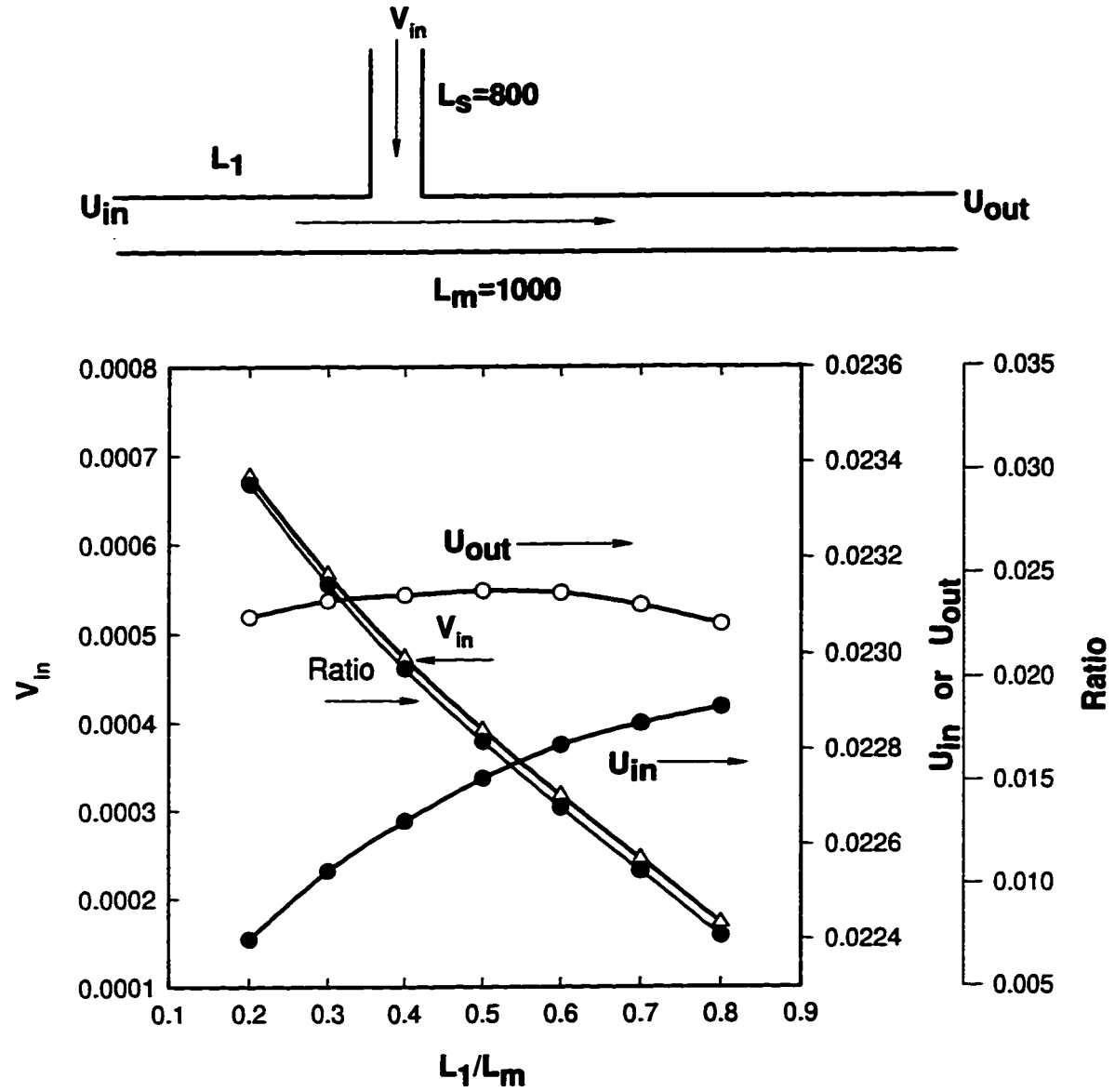


Figure 5.8. Variation of the dimensionless average velocity in the channels with the location of the side channel for $\kappa a = 20$, $\zeta = -1.0$, $L_s = 800$, $L_m = 1000$, $\Phi_1 = 10000$, $\Phi_2 = 0$, Φ_3 is floating.

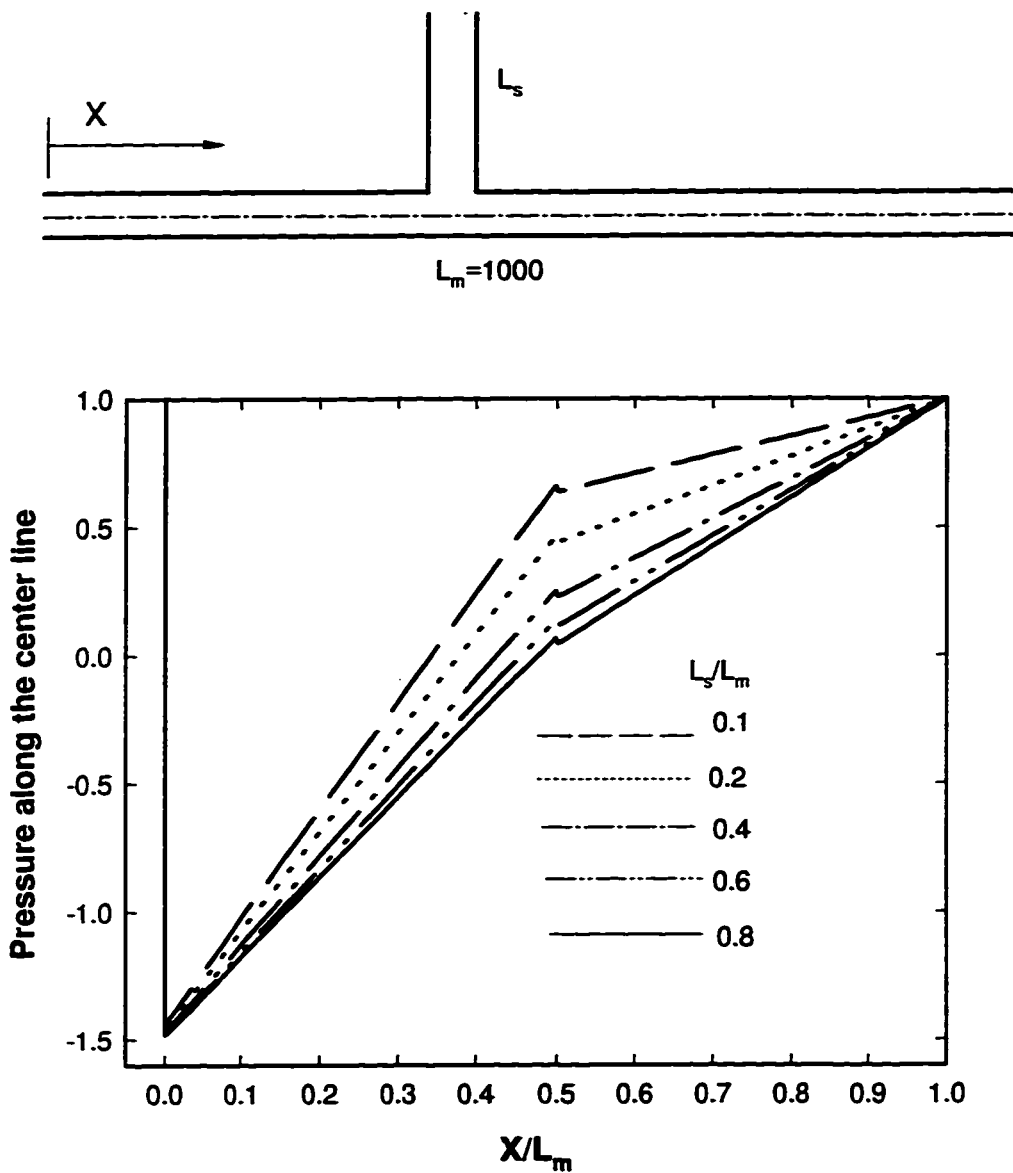


Figure 5.9. Pressure profile along the center line of the main channel for different side channel length for $\kappa a=20$, $\zeta=\zeta'=-1.0$, $L_m=1000$, $\Phi_1=10000$, $\Phi_2=0$, Φ_3 is floating.

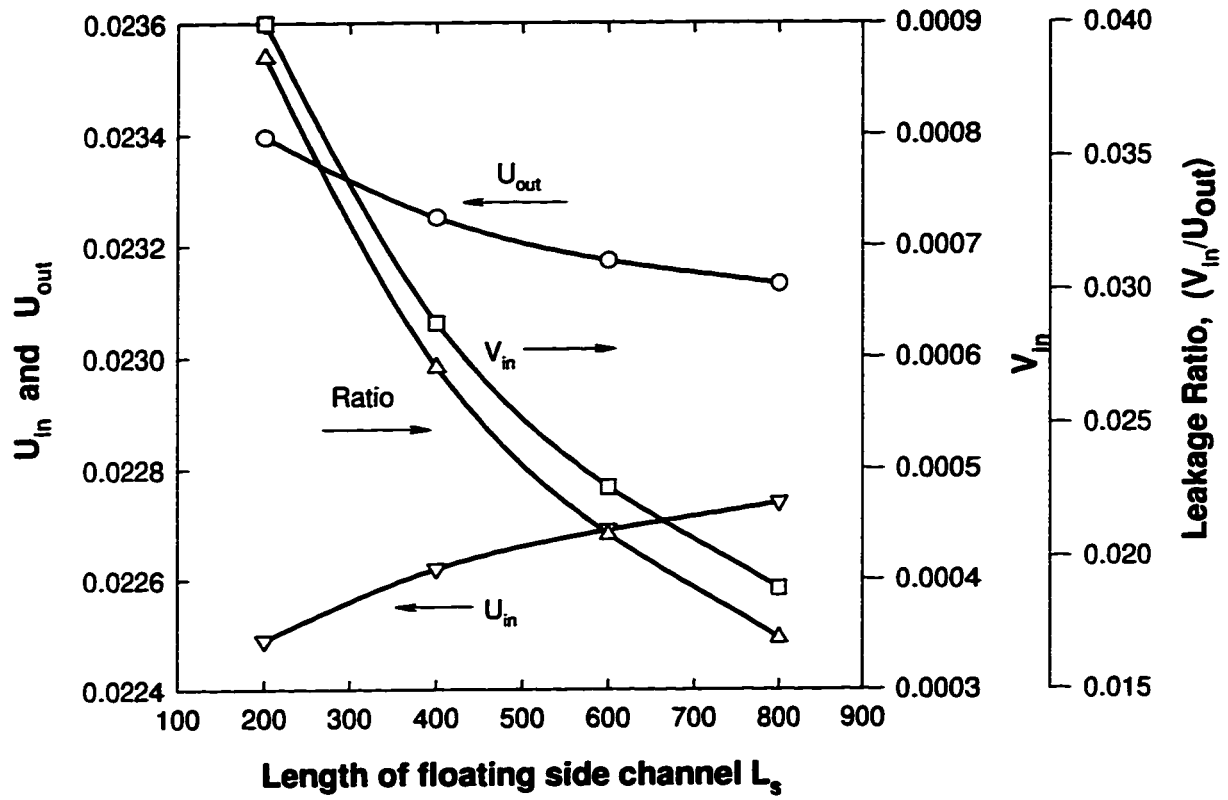
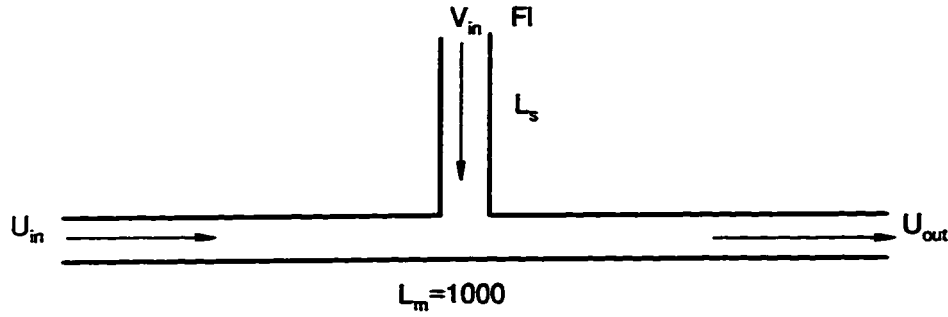


Figure 5.10. Variation of dimensionless average velocity in the channels with the length of the side channel for $\kappa a = 20$, $\zeta = \zeta' = -1.0$, $L_m = 1000$, $\Phi_1 = 10000$, $\Phi_2 = 0$, Φ_3 is floating.

5.2.4 Effect of the Surface Potential and the Electric Field

The surface zeta potential is normally influenced by both the solution composition in terms of electrolyte content and pH value and the surface characteristics [8]. Thus when the electrolytes in the side channel and the main channel are different in pH or composition, the zeta potential in each channel can in general be different as well. In turn, the surface zeta potential and the electrolyte concentration determine the channel's electroosmotic flow. Results from this study have shown that, for the case of a floating side channel, the flow in each channel will not vary with zeta potential of the side channel. This can be expected from the analysis discussed in the previous sections, that is, when the side channel is left floating, the driving force for the fluid flow in the side channel is due to the pressure difference rather than electric force. However, the zeta potential of the main channel would affect both flows in the main channel and the side channel.

From figure 5.11, one can observe that the average velocity in each channel is linearly proportional to the zeta potential in the main channel. The ratio of leakage from the floating side channel to the total flow in the main channel does not vary with zeta potential of the main channel. The relationship between the electroosmotic flow and zeta potential in manifold channels is similar to that of a straight channel. As illustrated in chapter 4, the velocity increases with zeta potential. The linear relationship between the velocity in the side channel and zeta potential can also be expected from the transport equation for creeping flow. The average velocity is proportional to the pressure difference between the side reservoir and the intersection point, while the pressure at the intersection point is linearly dependent on the flow in the main channel.

Figure 5.12 shows the variation of the average velocity in each of the channels with the electric field strength. As expected, the flow increases linearly with the electric field strength.

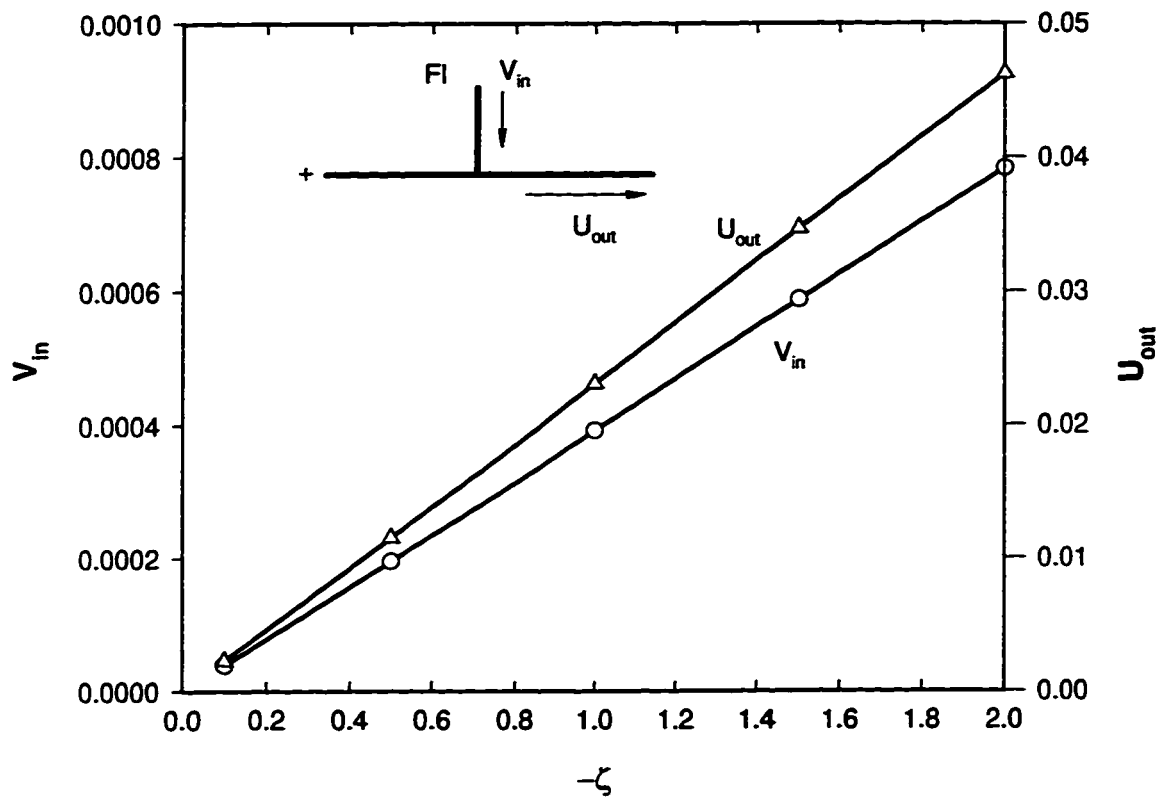


Figure 5.11. Variation of average velocity in the channels with the surface potential for $\kappa a=20$, $\zeta'=\zeta$, $L_m=1000$, $L_s=800$, $\Phi_1=10000$, $\Phi_2=0$, Φ_3 is floating.

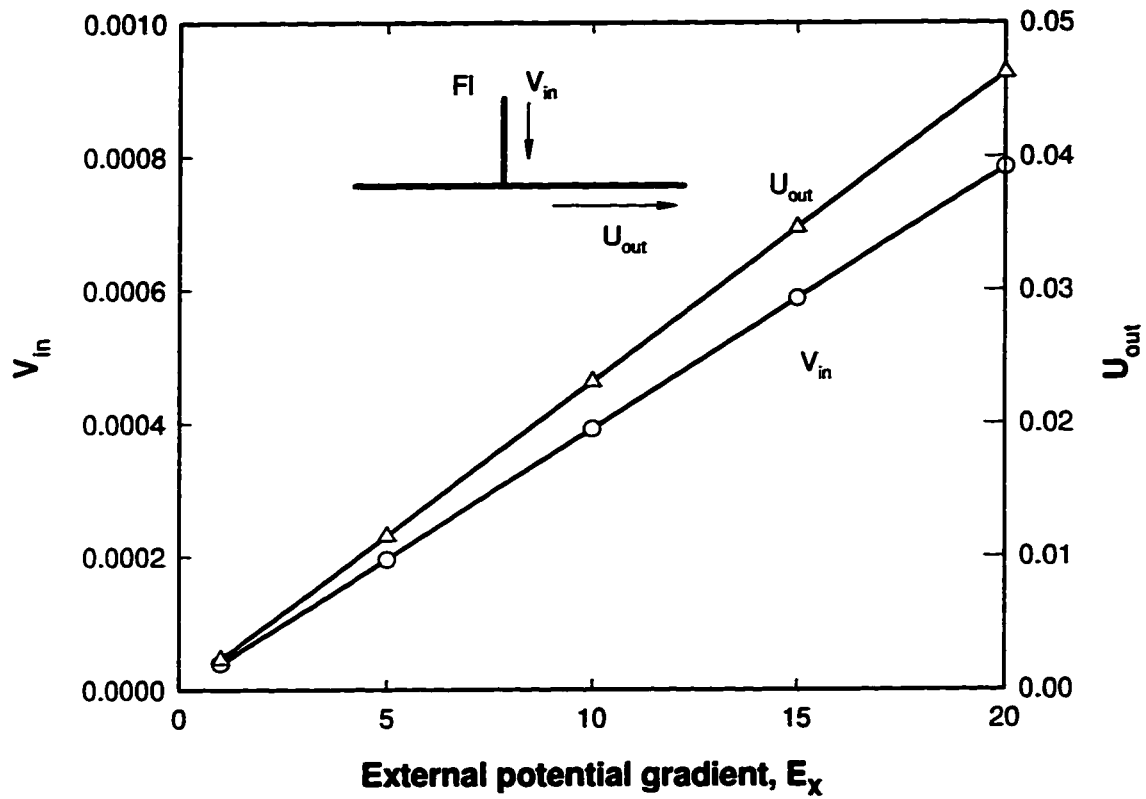


Figure 5.12. Variation of average velocity in the channels with the electric potential gradient for $\kappa a=20$, $\zeta=\zeta'=-1.0$, $L_m=1000$, $L_s=800$, $\Phi_2=0$, $\Phi_1=E_x L_m$, Φ_3 is floating.

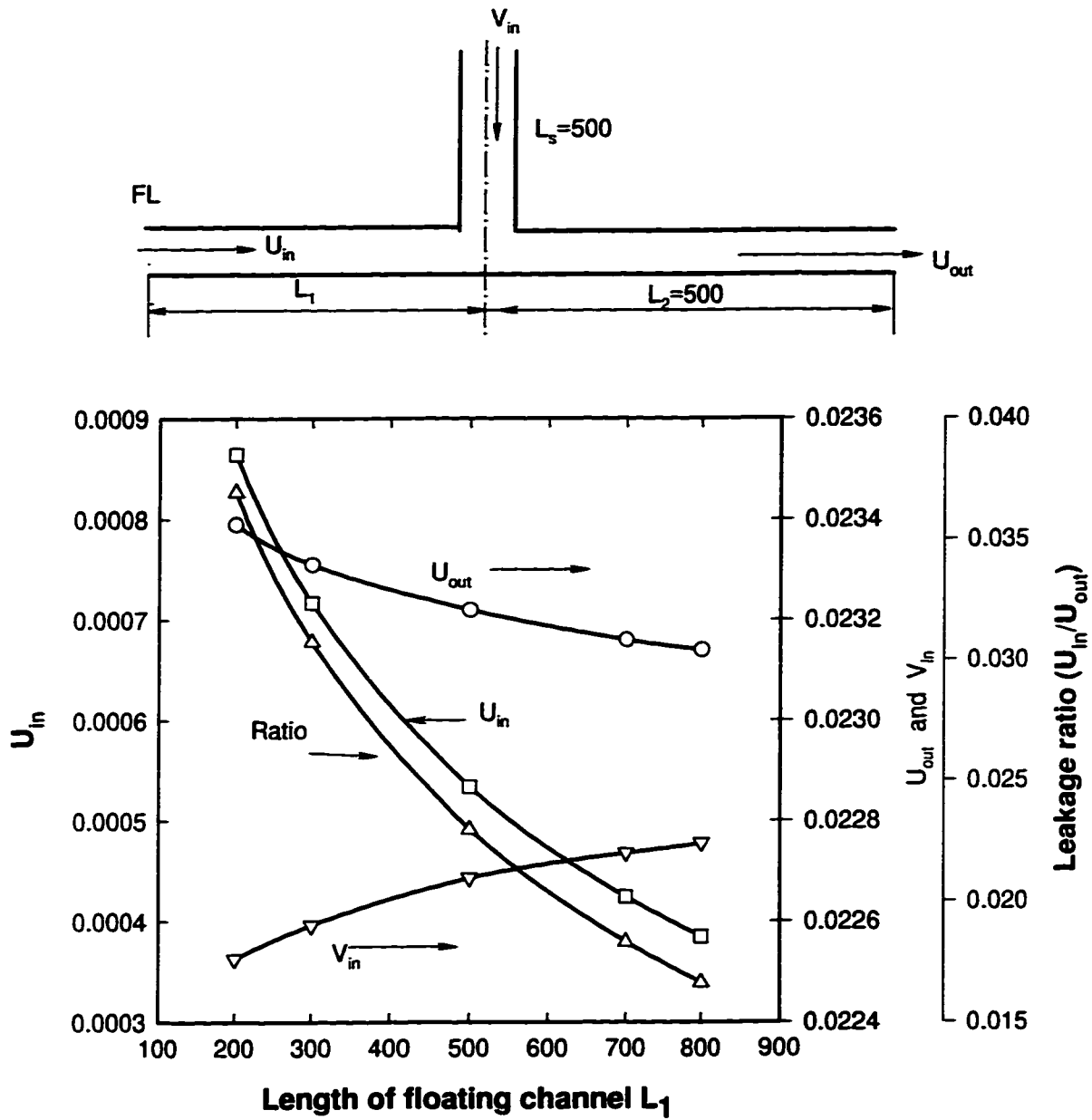


Figure 5.13. Variation of dimensionless average velocity in the channels with the length of floating channel for $\kappa a=20$, $\zeta=\zeta'=-1.0$, Φ_1 is floating, $\Phi_2=0$, $\Phi_3=10000$.

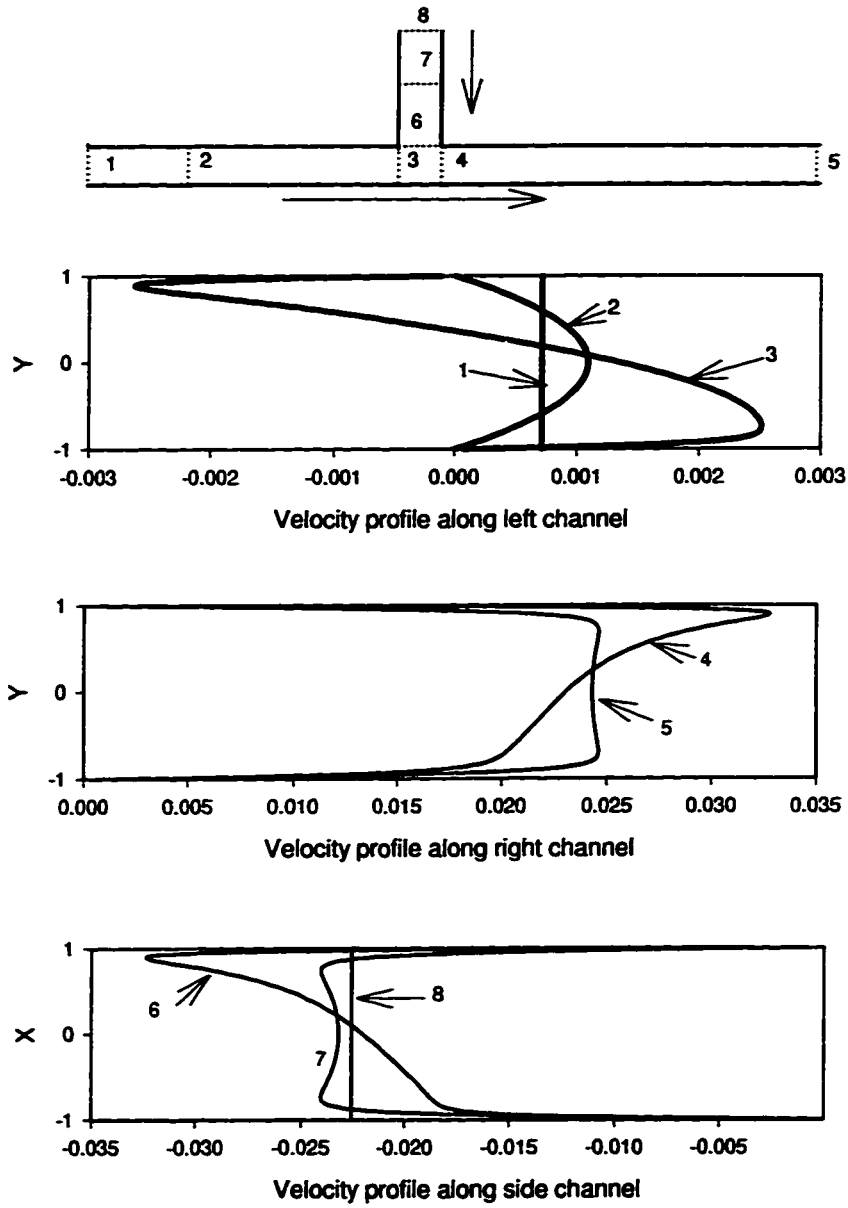


Figure 5.14. Velocity profiles at different locations for $L_1=200$, $L_2=500$, $L_3=500$, $\kappa a=20$, $\zeta=\zeta'=-1.0$, $\Phi_3=10000$, $\Phi_2=0$, Φ_1 is floating.

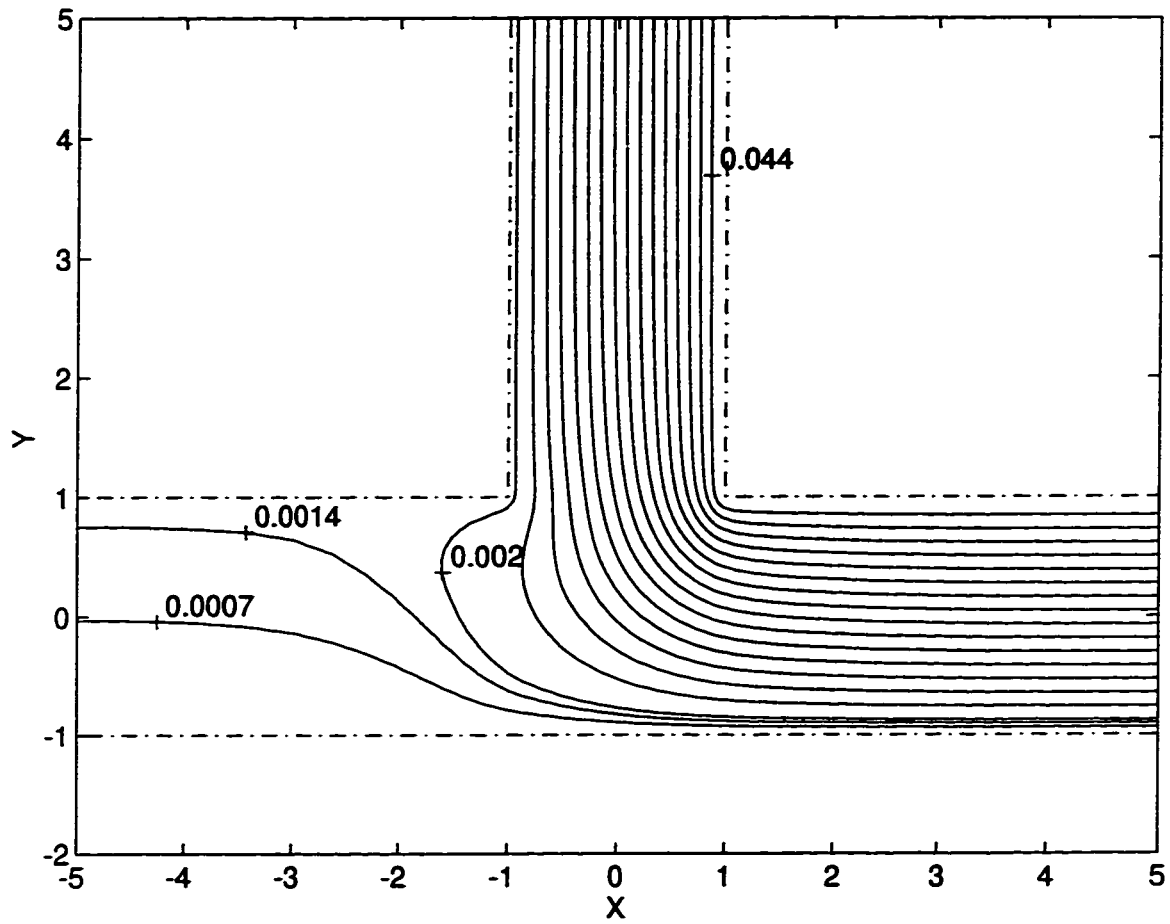


Figure 5.15 Streamline at intersection region for $L_1=200$, $L_2=500$, $L_s=500$, Φ_1 is floating, $\Phi_2=0$, $\Phi_3=10000$, $\kappa a=20$, $\zeta=\zeta'=-1.0$.

5.2.5 Effect of the Floating Channel Length When Flow is around a Corner

In figures 5.13 and 5.14, the electrolyte was directed from the side reservoir toward the right reservoir while the remaining reservoir (left side) was left floating (F1). Figure 5.13 shows the variation of the velocity in each channel with the length of the floating channel for $L_s=500$, $L_1=500$, $L_2=200\sim 800$. Taking a close look at both figures 5.10 and 5.13, one can find that the trends are similar to each other. The leakage from the floating channel decreases with increasing floating channel length. The velocities in the two active channels (side and right) varied little with an increase in the floating channel length, e.g., the average velocity in the side channel varies from 0.02252 for $L_1=200$ to 0.02276 for $L_1=800$. The ratio of leakage out of the floating side channel to the flow out of the right active channel ranges from 3.70% for $L_1=200$ to 1.66% for $L_1=800$. Comparing these values with the case in section 5.2.3, we can say that essentially no difference in the flow between both cases is present. The reason for this may be that the resistance to flow around the corner is the same as the resistance to the straight flow for creeping flow in which the inertia terms are neglected.

Figure 5.14 shows the velocity profiles in each channel. As expected, the velocity is parabolic in the floating channel. The velocity profile at cross-section 3 shows both inflow and outflow at the intersection region with a net flow from the floating channel to the active channel. The streamlines in figure 5.15 clearly show the flow near the intersection region.

5.3 Flow in Each Channel with an Electric Potential Applied to Each Reservoir

5.3.1 Control of Leakage by Use of a Potential

All of the results discussed up to now have been based on a system in which one of the intersecting channels was left floating. As indicated above, the leakage out of the floating side channel is due to convective effects. The leakage can be controlled by increasing the length of the side channel or changing the position of the side channel.

It is also possible to control the flow at the intersecting channels by controlling the potential of all reservoirs from which a channel initiates. Considering the three channels intersecting in a T shaped configuration ($L_m=1000$, $L_s=800$), three potentials are applied to the reservoirs with two potential sources and a ground potential. The potential at the left reservoir is fixed at $\Phi_1=10,000$, the right potential at ground. The problem is to predict what is the side potential Φ_3 required for zero leakage.

Figure 5.16 shows the variation of the dimensionless average velocity in the channels with the side potential Φ_3 . It shows a linear dependence of the velocity in each channel on the potential applied to the left reservoir. We also note that the leakage from the side channel is zero when the side channel potential is at 4820. As was indicated in figure 5.3, the potential at the side channel is 5000 when the side channel is left floating. This means that an electric potential difference of 180 is needed to counter the flow. The potential distributions in the channels are illustrated in figure 5.17 for $\Phi_3=4820$. It shows the electric potential distributions in both the main channel and the side channel are basically linear, see a) and c) of figure 5.17. A small perturbation at the intersection region is expected. Figure 5.18 shows the pressure profiles along the center line of the main channel for different side channel potentials. Figure 5.18 clearly shows that there exists a pressure difference between the intersection and the side channel end at which the pressure is the same as that of main channel ends. It is this pressure difference that needs to be balanced by electric force for zero leakage.

5.3.2 Effect of the Surface Potential of the Channels

In this section, the effect of surface potentials in both the main channel and the side channel will be discussed with three electric potentials applied to all reservoirs. When the surface potentials are different in each channel, the electroosmotic flow will also be different. The difference in electroosmotic flow between each channel will result in hydrodynamic effects. The flow behavior will be discussed in this section.

Figures 5.19 and 5.20 show the variation of the average velocity in both the side channel and the main channel with the side channel surface potential, for different left

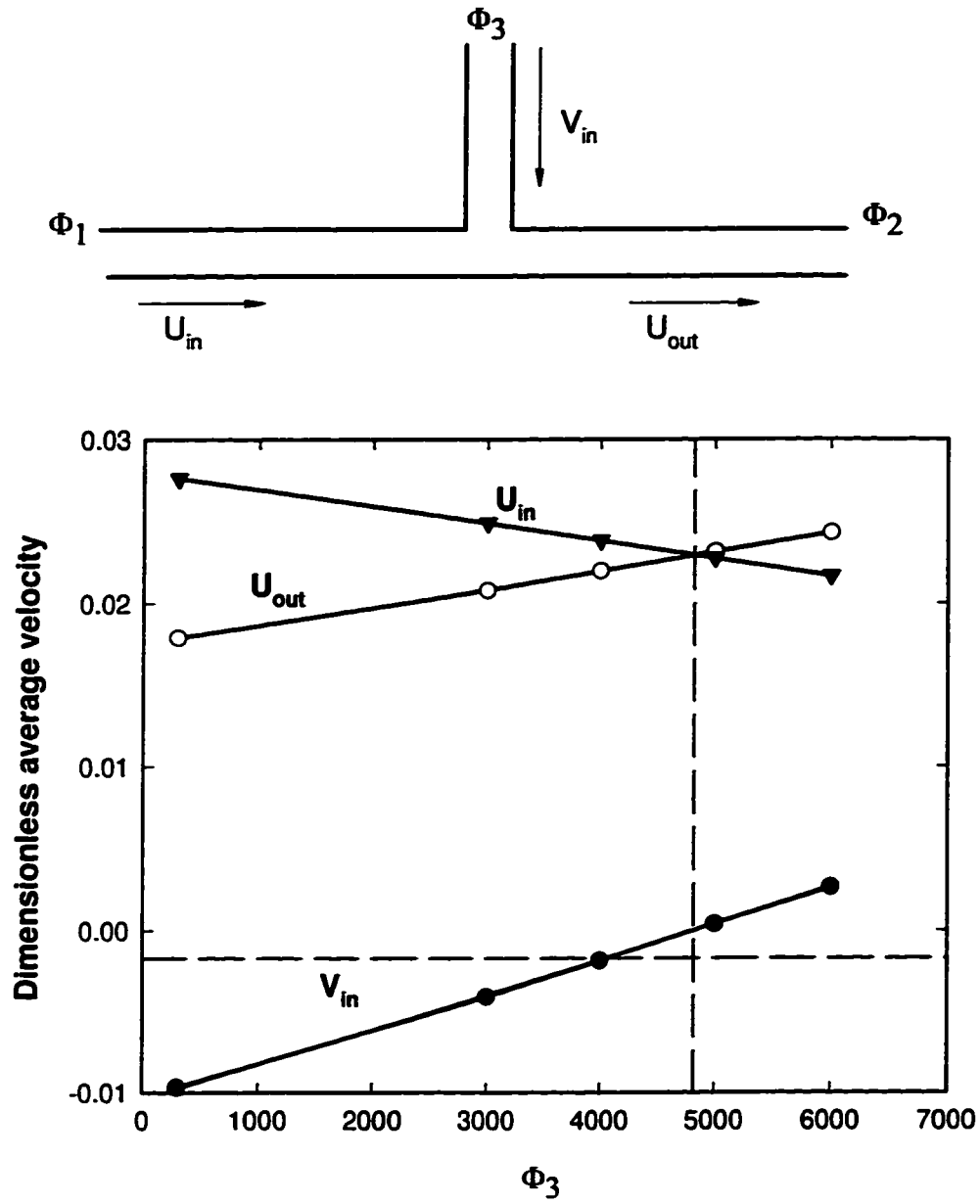


Figure 5.16. Variation of the dimensionless average velocity in the channels with the side reservoir potential for $\kappa a=20$, $\zeta=\zeta'=-1.0$, $\Phi_1=10,000$, $\Phi_2=0$, $L_m=1000$, $L_s=800$.

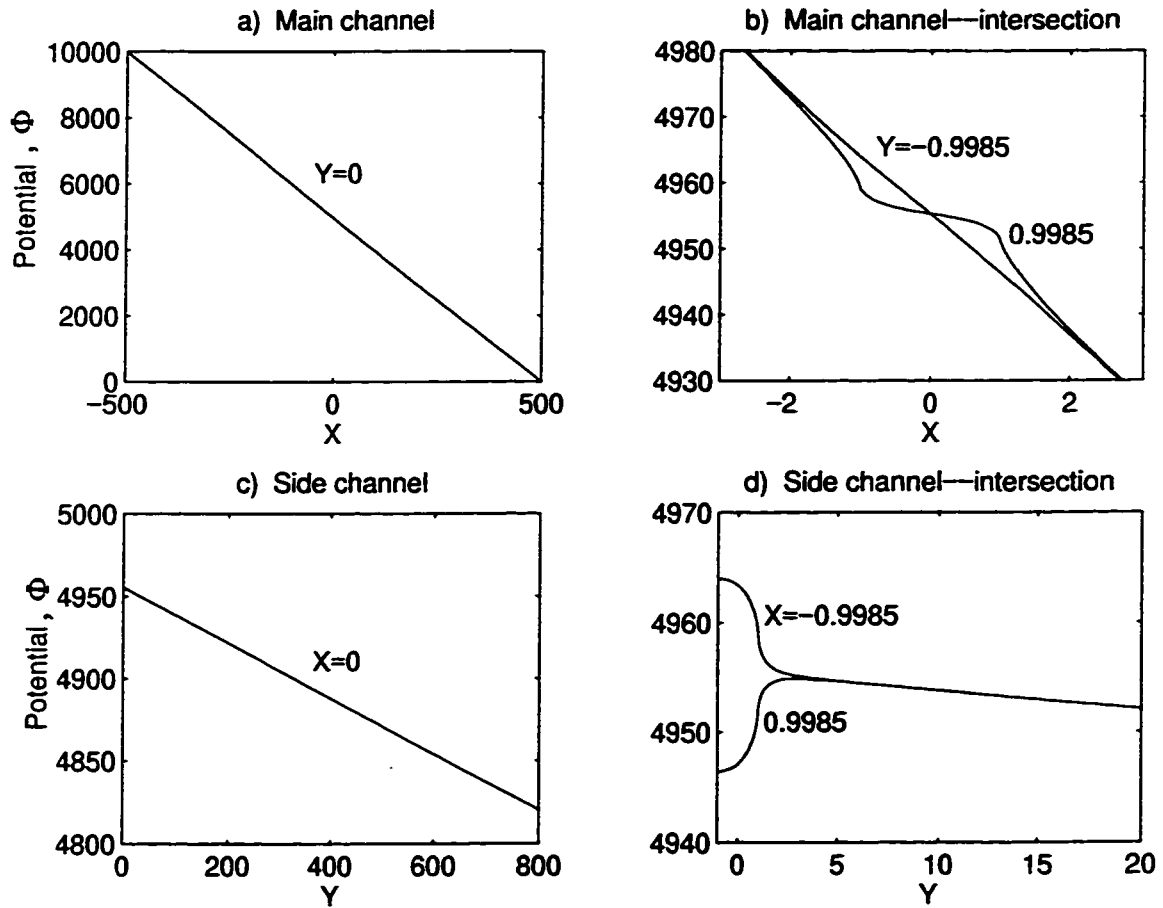


Figure 5.17 External electric potential distributions in the channels for $L_m=1000$, $L_s=800$, $\Phi_1=10,000$, $\Phi_2=0$, $\Phi_3=4820$.

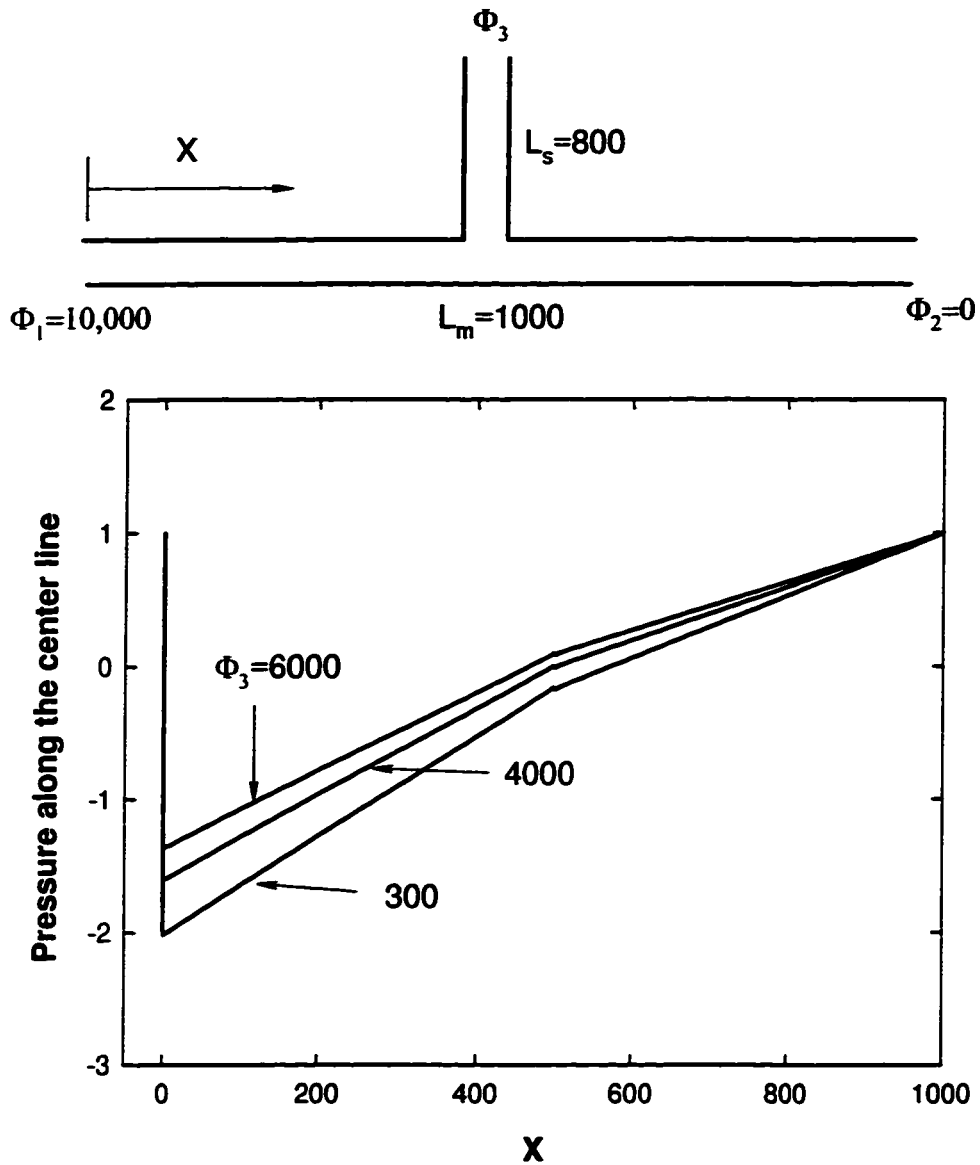


Figure 5.18. Pressure profiles along the center line of the main channel for different side reservoir potential ($L_m=1000$, $L_s=800$, $\kappa a=20$, $\zeta=\zeta'=-1.0$, $\Phi_1=10,000$, $\Phi_2=0$)

channel potential Φ_1 . From figure 5.19, one can observe that the velocity in the side channel increases with the side channel surface potential. This is straight forward as the electric force is linearly dependent on the surface potential. The plot also shows that the velocity in the side channel for $\Phi_1=5500$ is larger than that of $\Phi_1=10,000$. This can be explained by the increased electric field strength in the side channel with $\Phi_1=5500$. The potential at the intersection can be approximately obtained from equation (2.35).

Case 1: For $\Phi_1= 5500$, $\Phi_2= 0$, $\Phi_3= 5500$, $L_1 = L_2 = 500$, $L_s= 800$, one can calculate $\Phi_J= 3404.76$ from equation.(2.35); The electric field strength in the side channel is given by $E_s = (\Phi_3-\Phi_J)/L_s = 2.619$. Similarly the electric field strength in the left channel, $E_1 = (\Phi_1-\Phi_J)/L_1= 4.191$; the electric field strength in the right channel, $E_2 = (\Phi_J-\Phi_2)/L_2= 6.810$.

Case 2: For $\Phi_1=10000$, $\Phi_2=0$, $\Phi_3=5500$, $L_1 =L_2=500$, $L_s=800$, one can get $\Phi_J=5119.05$. The electric field strengths in each channel are given as, $E_s= 0.476$, $E_1=9.762$, $E_2=10.238$. Clearly, the electric field strength, E_s , for $\Phi_1=5500$ is larger than that for $\Phi_1=10,000$. Therefore the flow in the side channel for $\Phi_1=5500$ is larger than that for $\Phi_1=10,000$.

From figure 5.20, one can observe that the average velocity in the left channel decreases slightly with the side channel surface potential. This is due to the increase in the resistance to flow in the intersection region when the flow in the side channel is increased. However, the total flow, U_{out} in the right channel increases with the side channel surface potential. This means that the increase of flow in the side channel dominates over the decrease of flow in the left channel.

In order to describe the hydrodynamic effect on the flow, figure 5.21 and figure 5.22 show the variation of velocity ratio in the channels with the side channel potentials. Here $V_{e,in}$ is the dimensionless average velocity in the side channel due to electroosmotic flow alone, which can be obtained from equation (4.5) for $P_x=0$. $V_{in}/V_{e,in}$ shows the magnitude of the hydrodynamic flow relative to the electroosmotic flow. Figure 5.21 shows that the hydrodynamic effect becomes smaller when the side channel surface potential is larger. This is because the electric force becomes larger as the side channel surface potential is increased. The reason why the velocity ratio for $\Phi_1=5500$ is less than

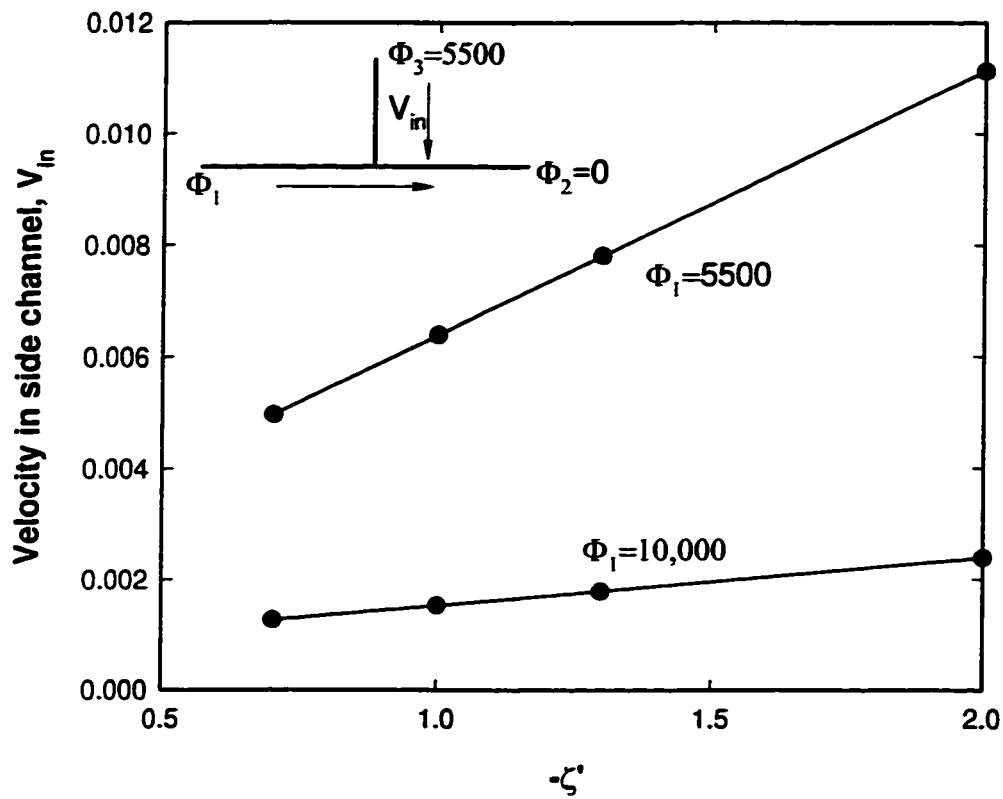


Figure 5.19. Variation of dimensionless average velocity in the side channel with side channel surface potentials for $L_m=1000$, $L_s=800$, $\zeta=-1.0$, $\Phi_3=5500$, $\Phi_2=0$.

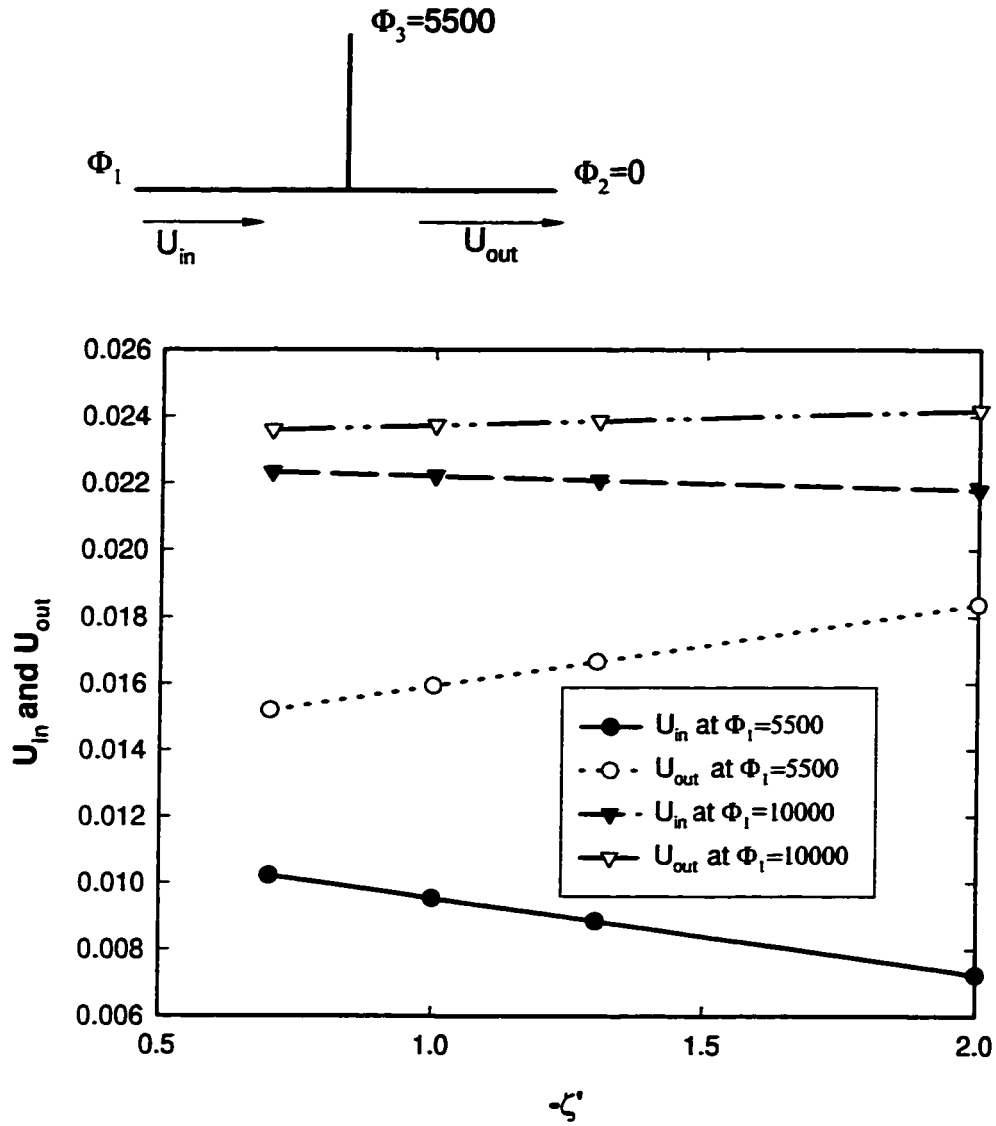


Figure 5.20. Variation of dimensionless average velocity in the main channel with side channel surface potential for $L_m=1000$, $L_s=800$, $\zeta=-1.0$, $\Phi_3=5500$, $\Phi_2=0$, $\kappa a=20$.

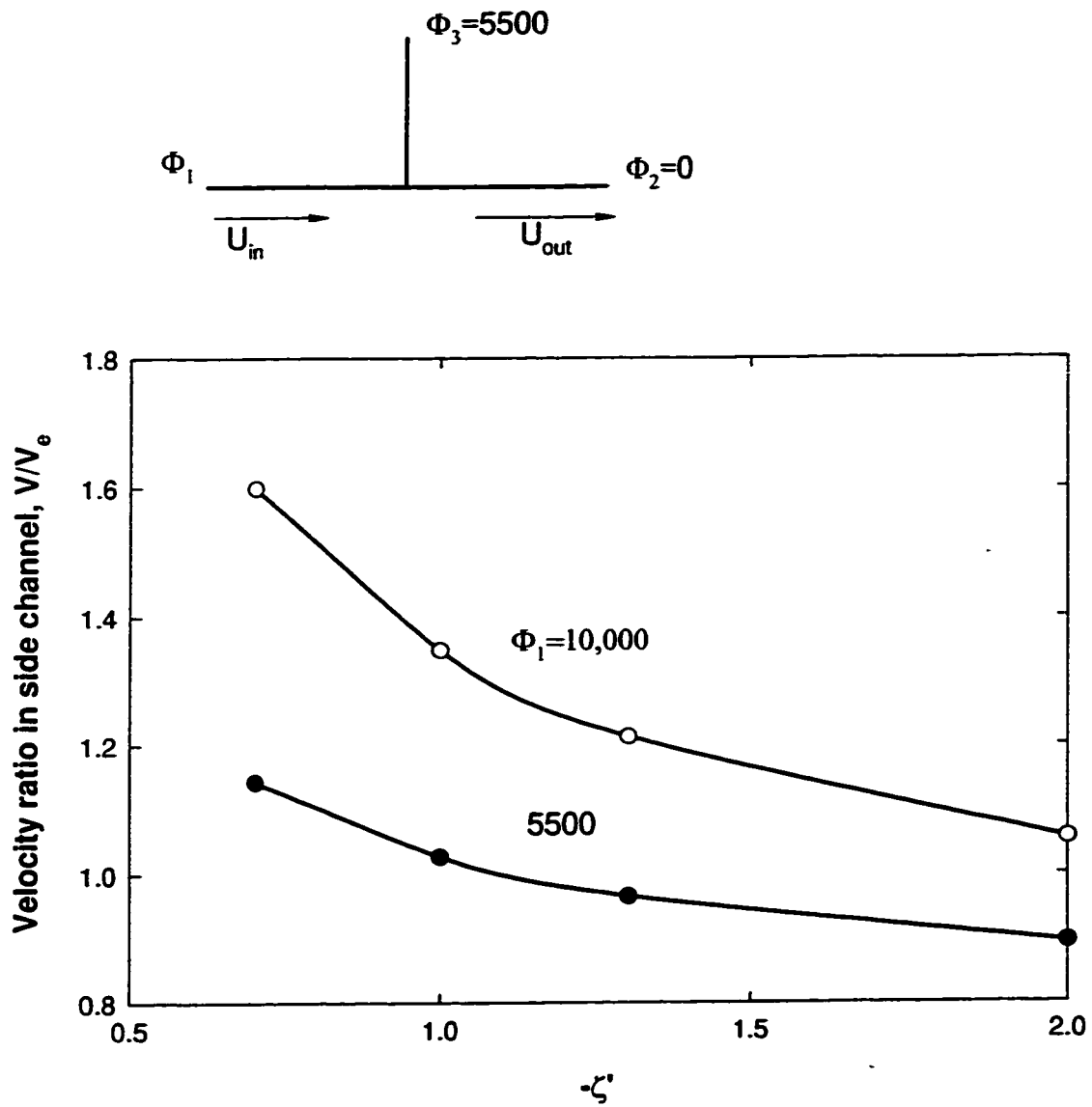


Figure 5.21. Variation of velocity ratio in the side channel with the side channel surface potential for $L_m=1000$, $L_s=800$, $\zeta=-1.0$, $\Phi_3=5500$, $\Phi_2=0$, $\kappa a=20$.

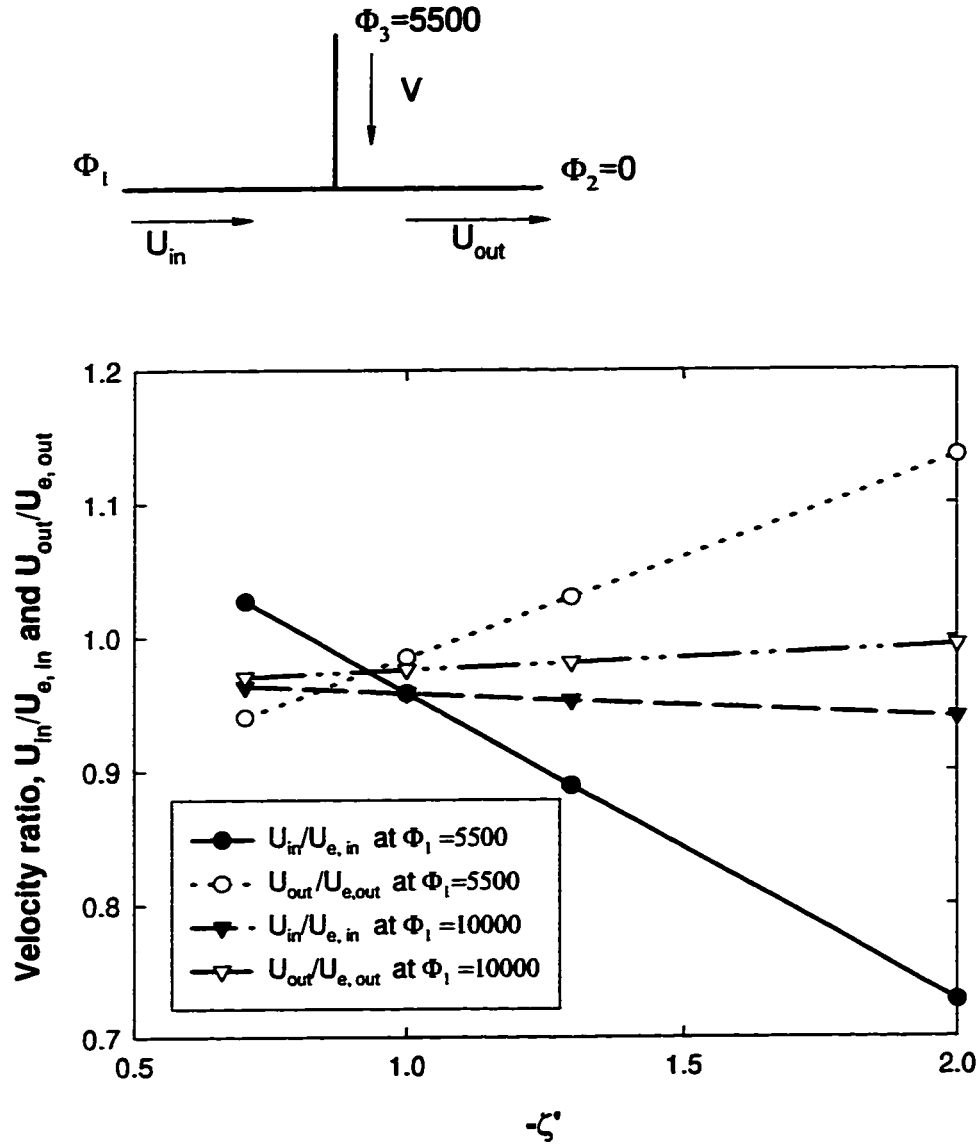


Figure 5.22. Variation of velocity ratio in the main channel with the side channel surface potential for $L_m=1000$, $L_s=800$, $\zeta=-1.0$, $\Phi_3=5500$, $\Phi_2=0$, $\kappa a=20$.

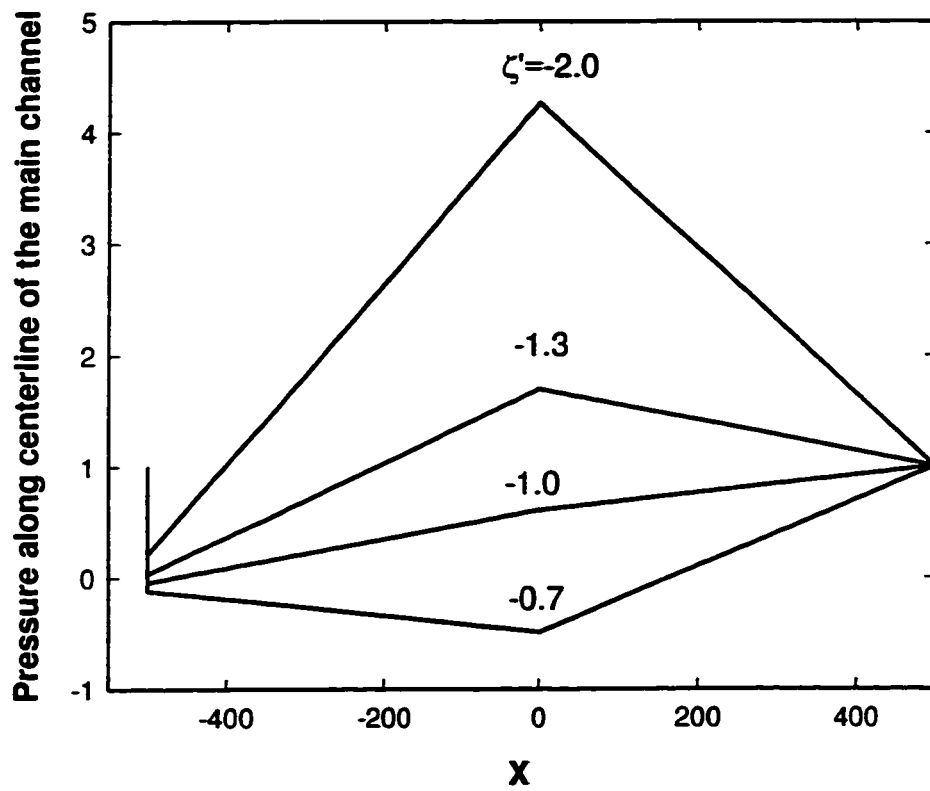


Figure 5.23. Pressure profiles along the center line of the main channel for different ζ' ($L_m=1000$, $L_s=800$, $\kappa a=20$, $\zeta=-1.0$, $\Phi_1=\Phi_3=5500$, $\Phi_2=0$).

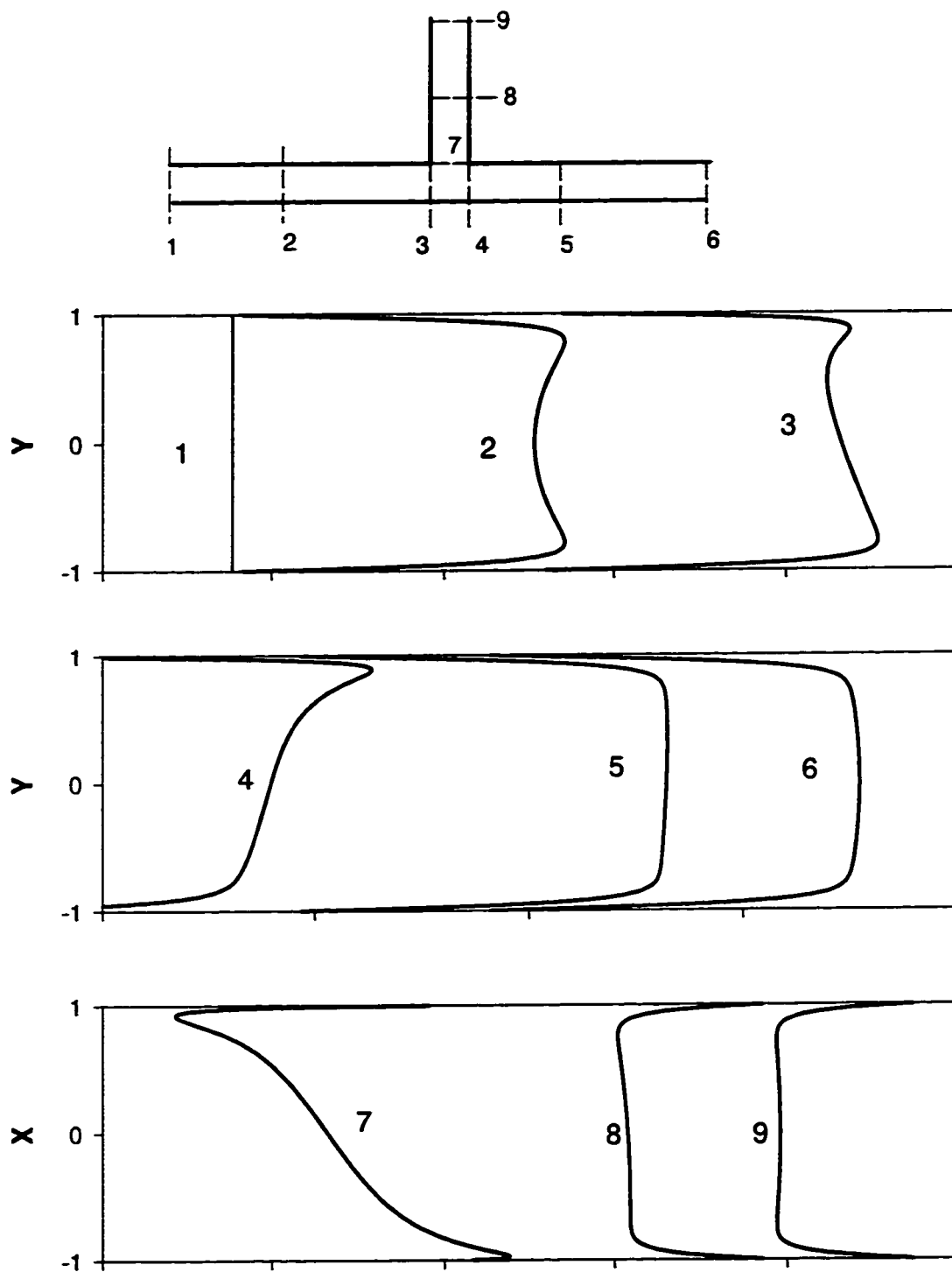


Figure 5.24. Velocity profiles at different sections for $L_m=1000$, $L_s=800$, $\Phi_1=\Phi_3=5500$, $\Phi_2=0$, $\zeta=-1.0$, $\zeta'=-1.3$.

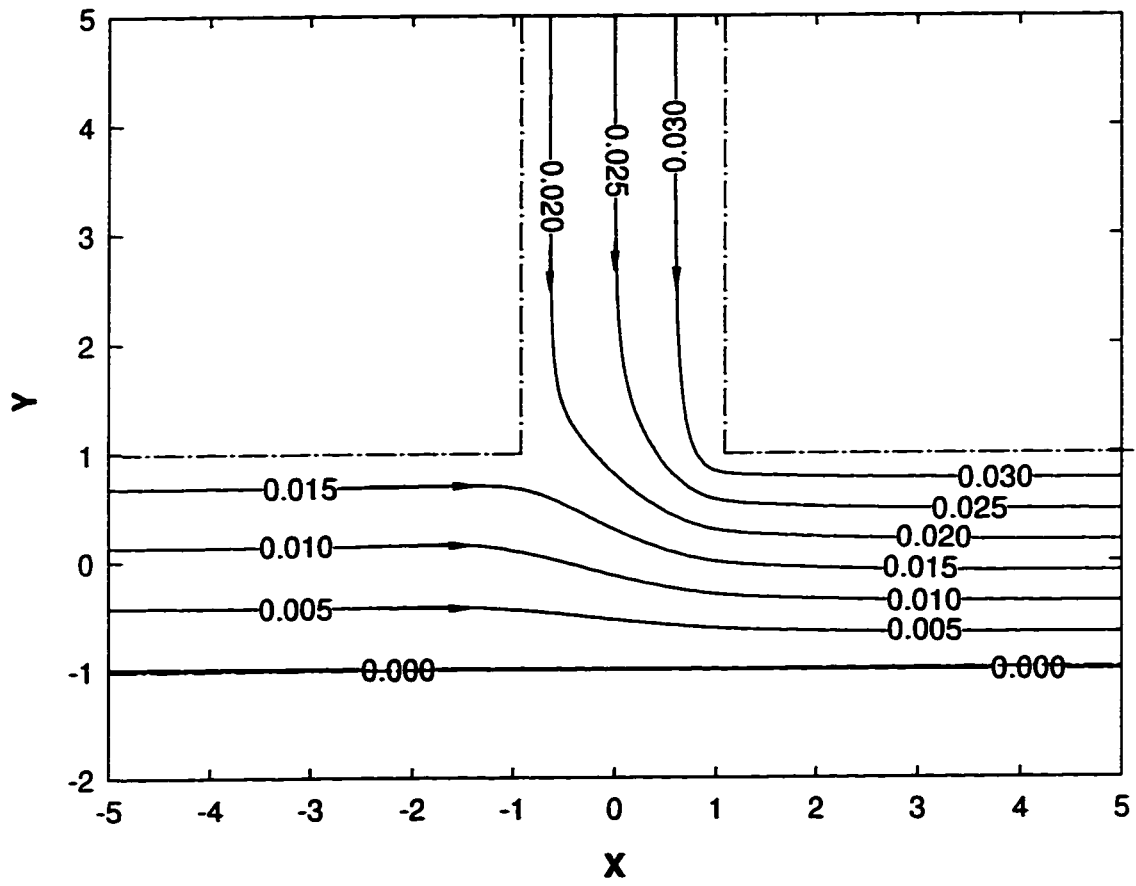


Figure 5.25. Streamlines in the channels for $L_m=1000$, $L_s=800$, $\kappa a=20$, $\zeta=-1.0$, $\zeta'=-1.3$, $\Phi_1=\Phi_3=5500$, $\Phi_2=0$.

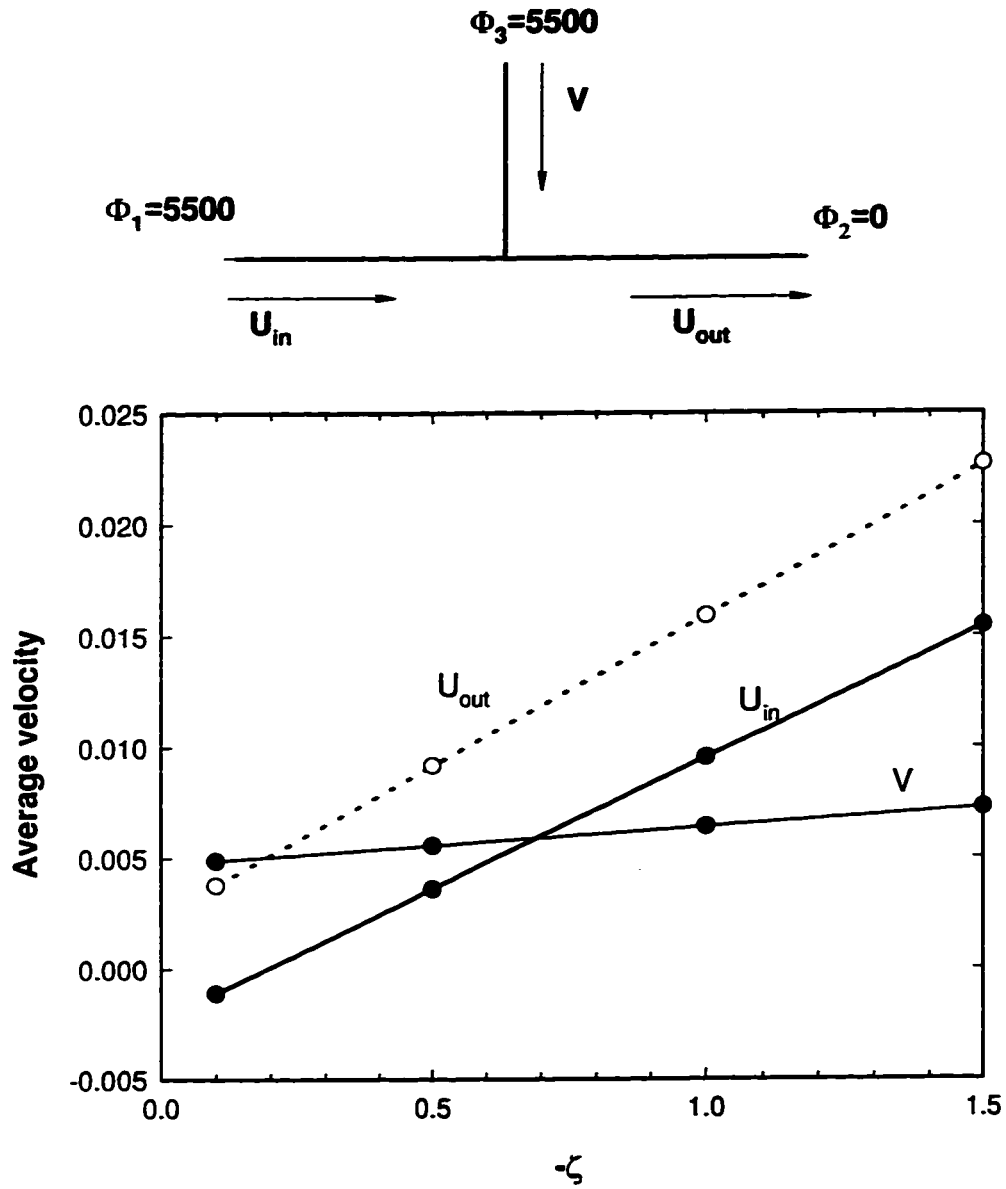


Figure 5.26. Variation of dimensionless average velocity in the channels with surface potential of the main channel for $L_m=1000$, $L_s=800$, $\zeta'=-1.0$, $\Phi_1=\Phi_3=5500$, $\Phi_2=0$

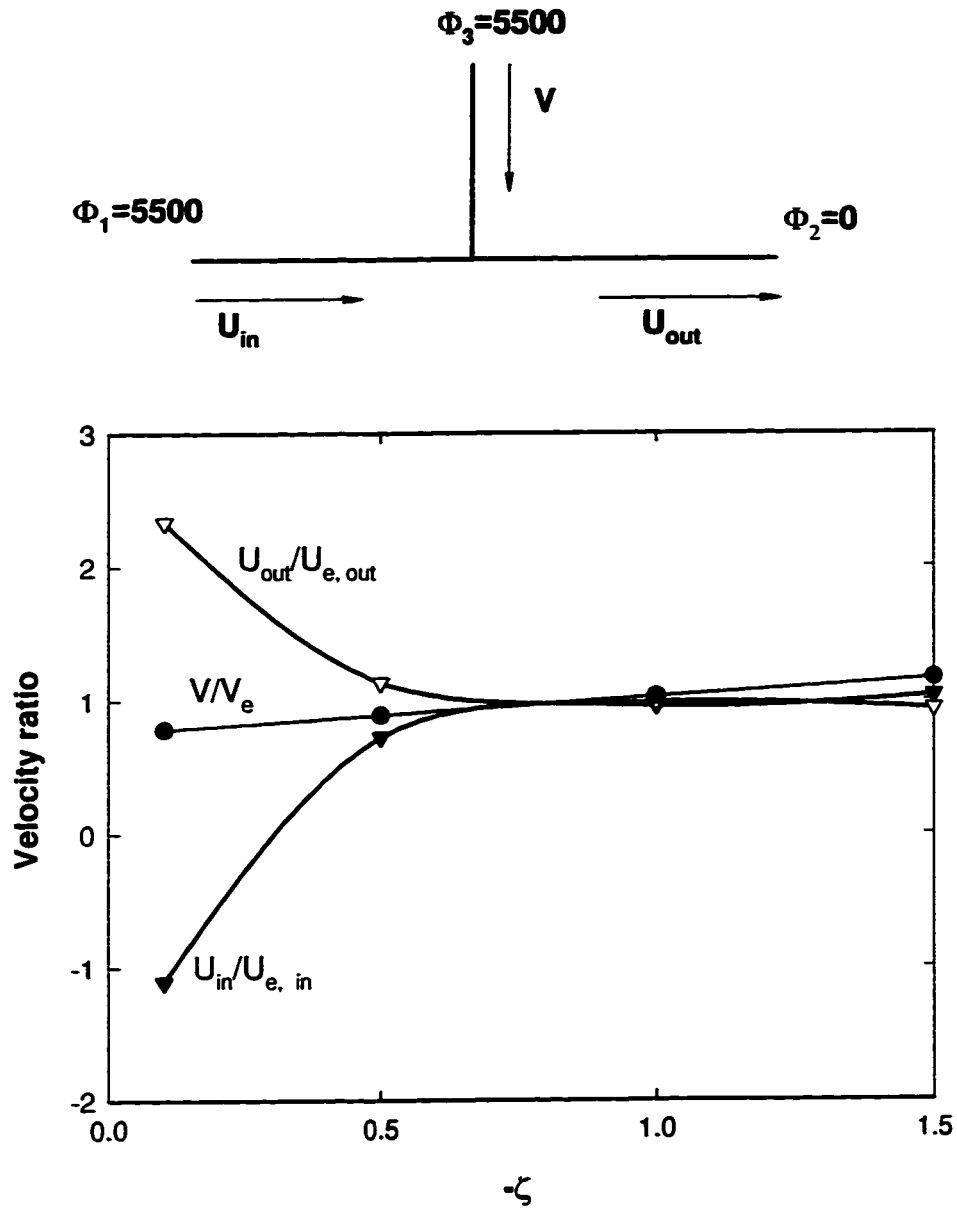


Figure 5.27. Variation of average velocity ratio in the channels with surface potential of the main channel for $L_m=1000$, $L_s=800$, $\zeta'=-1.0$, $\Phi_1=\Phi_3=5500$, $\Phi_2=0$.

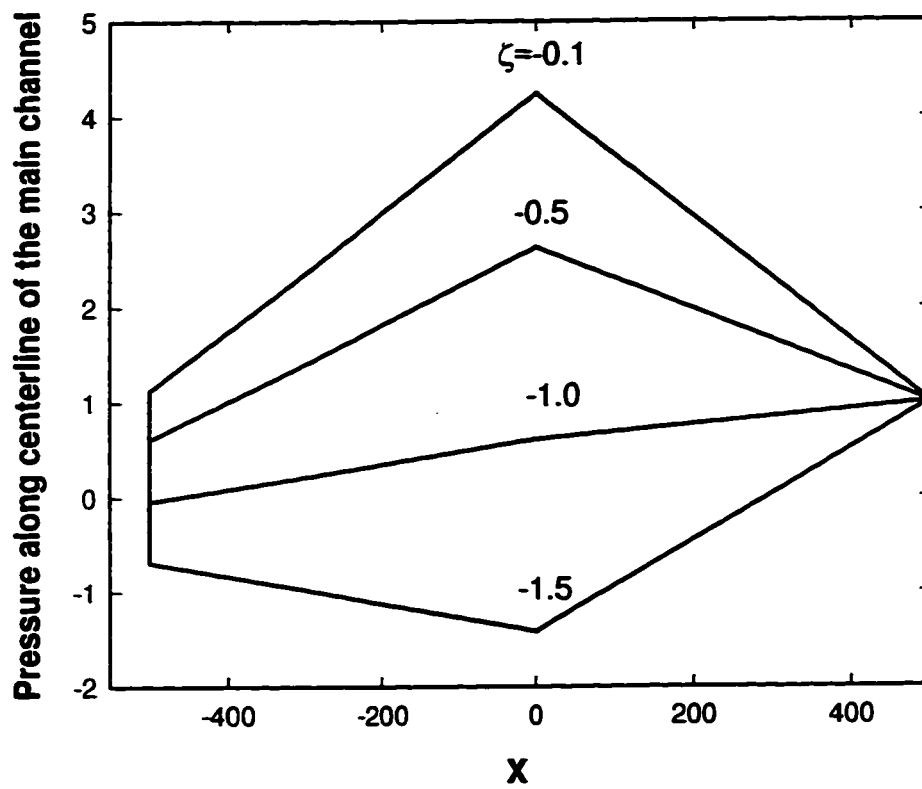
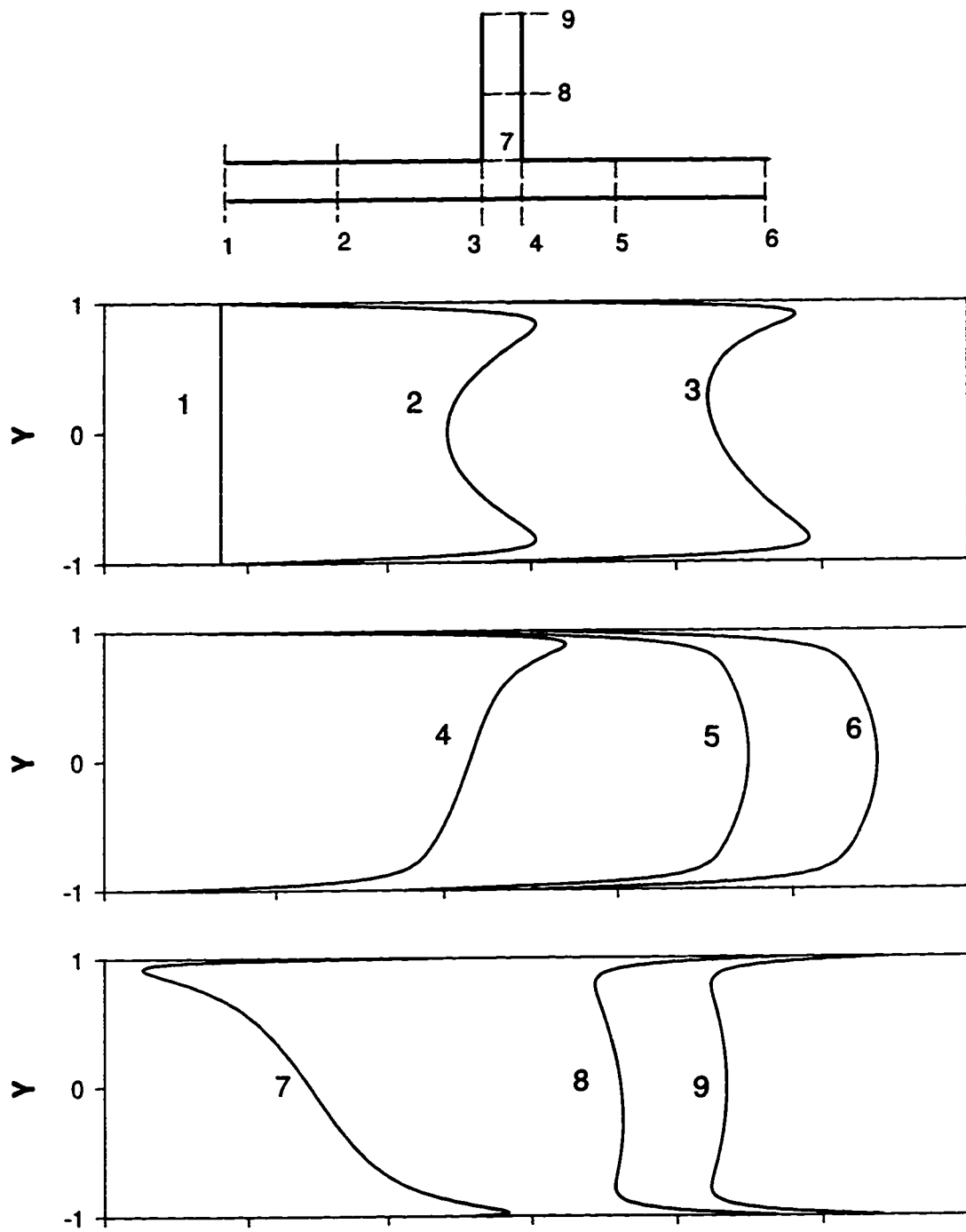


Figure 5.28. Pressure profile along the center line of the main channel for different ζ ($L_m=1000$, $L_s=800$, $\kappa a=20$, $\zeta'=-1.0$, $\Phi_1=\Phi_3=5500$, $\Phi_2=0$.)



Velocity profiles at different sections

Figure 5.29. Velocity profiles at different sections for $L_m=1000$, $L_s=800$, $\Phi_1=\Phi_3=5500$, $\Phi_2=0$, $\zeta=-0.5$, $\zeta'=-1.0$.

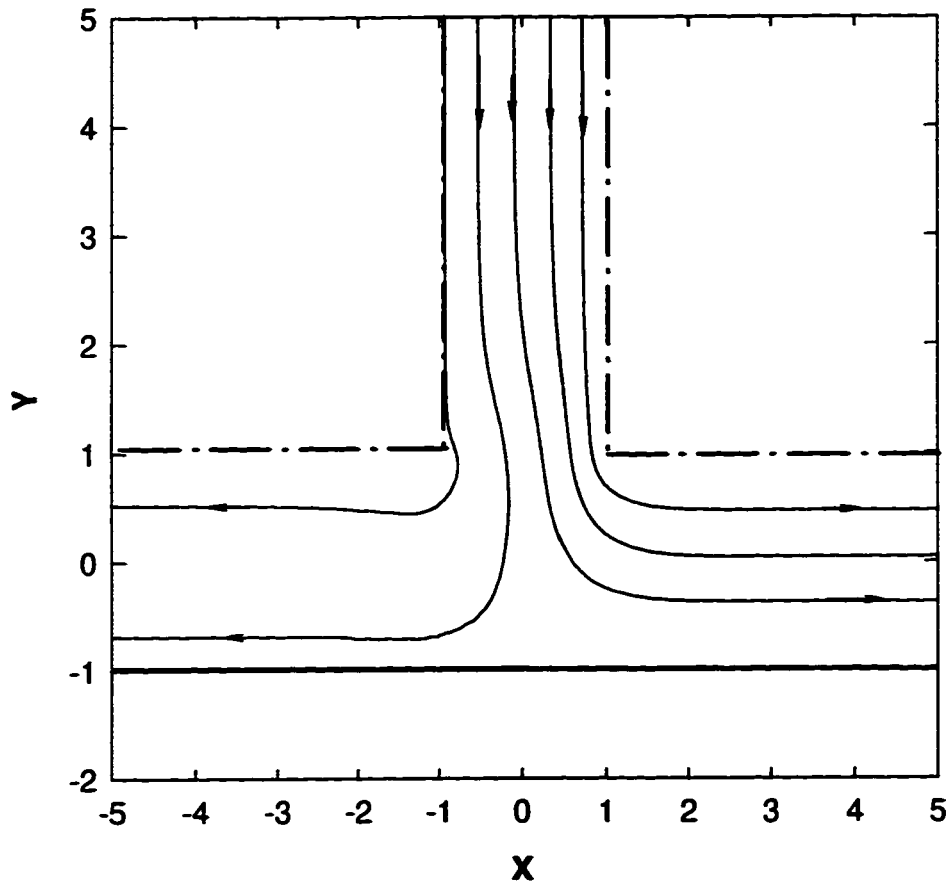


Figure 5.30. Streamlines in the channels for $L_m=1000$, $L_s=800$, $\kappa a=20$, $\zeta=-0.1$, $\zeta'=-1.0$, $\Phi_1=\Phi_3=5500$, $\Phi_2=0$.

that for $\Phi_1=10000$ is that the electroosmotic flow in the side channel for $\Phi_1=10000$ is smaller. Figure 5.22 shows the velocity ratio in the main channel for two different Φ_1 values. The plot illustrates that the relative effect of the hydrodynamic term for $\Phi_1=5500$ is stronger than that for $\Phi_1=10000$, as the electroosmotic flow in the main channel is larger for $\Phi_1=10000$.

Figure 5.23 shows the pressure profiles along the centerline of the main channel for different side channel surface potentials. It shows that the pressure at the intersection becomes larger as the side channel surface potential is increased, indicating the resistance to flow in the main channel is increased as the flow in the side channel is increased. From the pressure profile of figure 5.23, one can expect the velocity profile to be different in each channel, as the velocity profile is the superposition of both the electroosmotic flow due to an electric field and the hydrodynamic flow due to pressure gradient. The velocity profiles at different sections of the channels for $L_m=1000$, $L_s=800$, $\Phi_1=\Phi_3=5500$, $\Phi_2=0$, $\zeta=-1.0$, $\zeta'=-1.3$, are shown in figure 5.24. The velocity profiles at sections 2, 5 and 8 are fully developed profiles in the left, right and side channels, respectively. As indicated in figure 5.23, the pressure gradients in both the side and the left channels are positive, therefore, the hydrodynamic flow is against the electroosmotic flow, leading to concave velocity profiles at sections 2 and 8. The electroosmotic flow in the right channel is enhanced by the hydrodynamic flow, therefore the velocity profile at section 5 is convex. Figure 5.25 shows the streamlines for the conditions indicated in figure 5.24. It shows the flow path of liquid at different locations. The numbers of streamline in each channel indicates the relative magnitude of flow rate in each channel.

Figure 5.26 shows the variation of the dimensionless average velocity in the channels with the main channel surface potential for $L_m=1000$, $L_s=800$, $\Phi_1=\Phi_3=5500$, $\Phi_2=0$, $\zeta=-1.0$. The velocity in each channel increases with the main channel surface potential. It is not hard to understand the increase in flow in the main channel as the electroosmotic flow is proportional to the surface potential. One can observe that when the surface potential of the main channel is very small (e.g. $\zeta=-0.1$), the flow in the left channel is negative (figure 5.30 shows the streamline for this case). This means that for small main channel surface potential the pressure driving force dominates over the

electrokinetic force in the left channel, leading to flow toward the inlet of the left channel. The increase in the flow of the side channel is due to the increase of the momentum in the main channel, leading to more drag force at the intersection region. Figure 5.27 shows the variation of the velocity ratio in the channels with the main channel surface potential. It also illustrates the hydrodynamic effect is significantly higher for small surface potential.

The pressure profile of figure 5.28 may help in understanding the above mentioned trend. As indicated in figure 5.28, the pressure at the intersection is decreased when the main channel surface potential is increased. For $\zeta=-0.1$, the pressure at the intersection is so high that the flow in the left channel is reversed. Figure 5.29 shows the velocity profile for $\zeta=-0.5$. The profiles are similar to those of figure 5.24. The velocity in the left channel and the side channel are concave in shape, indicating the hydrodynamic flow is against the electroosmotic flow. The velocity profiles in the right channel are convex due to the negative pressure gradient, meaning that the net flow is due to the contribution of both the electroosmotic flow and a pressure driven flow.

Chapter 6

Summary and Recommendations

The objective of this study was to analyze the electroosmotic flow in a capillary electrophoresis system (CE). The electroosmotic flow plays a very important role in CE and makes the full automation of a CE system possible. It is desirable that liquid flow in intersecting channels be controlled and determined quantitatively for a CE system in which electroosmotic injection and electrophoresis are integrated together on a planar glass chip. The mechanism of the control of electroosmotic flow in a single straight channel and in intersecting channels of a T-shaped configuration has been studied.

A numerical study was carried out for steady electrokinetic flow in both single straight capillary channels and intersecting channels of a T-shaped configuration. The Poisson-Boltzmann equation was decoupled from the transport equations. The electric potential and the space charge density distributions on a cross section of a capillary were obtained numerically by solving the nonlinear Poisson-Boltzmann equation for arbitrary electrokinetic radius (κa) and arbitrary surface potentials. The electrostatic potential due to an applied electric field was obtained by the Poisson equation. The velocity and pressure profiles were obtained by solving the modified Navier-stokes equation using a primitive variables algorithm.

Initially the electroosmotic flow control in a single straight channel was studied by changing the surface potential on the mid part of the capillary channel and by the use of auxiliary pumping capillary. It was shown that a hydrodynamic effect is induced due to the difference in electroosmotic flow along the channel. The velocity profile is a superposition

of an electroosmotic flow and a Poiseuille flow. The velocity profiles along the channel was no longer 'plug-like' under some conditions. The effect of Taylor dispersion due to non-plug like velocity profile on the separation efficiency of capillary electrophoresis may need to be considered.

A systematic study on the effect of the main variables was undertaken for the intersecting channels in a T-shaped configuration. It was shown that the convective effect is an important factor that affects liquid leakage from the floating channel in an intersecting channel system in which electric field is applied to induce electroosmotic flow in active channels. The magnitude of leakage out of the floating channel depends on the length and location of the channel. The longer the floating channel is, the less the fluid leakage out of it. The ratio of leakage out of the floating side channel to the total flow in the main channel ranges from 14.56% for $L_m=100$ to 1.13% for $L_m=1500$, when the ratio of the length of the side channel to that of the main channel is maintained at 4/5. When the lengths of the channels are kept the same (eg. $L_m=1000$, $L_s=800$), the flow out of the side channel varied with the location of the side floating channel. The ratio of the leakage changed from about 3% to 0.6% when the side channel moved downstream from the entrance to the outlet. It was shown that the leakage phenomenon from the floating channel was the same, irrespective of the direction of flow at the intersection. The surface potential and electric field were quantitatively shown to be very important parameters controlling the electroosmotic flow. The linear dependence of the flow in each channel on the surface potential and electric field were demonstrated.

The predicted streamline pattern was shown to be similar to the experimentally obtained photograph[16]. The velocity profiles in both the main channel and side channel were obtained. It was shown that the velocity profile in a floating channel is parabolic as the driving force in this channel is due to pressure rather than electric force. The velocity profiles in active channels were shown as a combination of electroosmotic flow and Poiseuille flow.

The control of flow in each channel by use of an applied potential was illustrated. It was shown that the direction of the flow could be reversed in one of the channels by manipulating the applied potential at each reservoir. The velocity in each channel varied with the surface potential when an electric potential was applied to each reservoir.

The numerical results, of course, must be validated by experimental tests. To this end, some experiments have been carried out on measuring electroosmotic flow and electrokinetic parameters in the Chemistry Department of University of Alberta. Further studies using numerical modelling of electroosmotic flow for 3- Dimensional problems and heat transfer under the influence of electric current should be conducted.

References

- [1] Grossman, P. D., Colburn, J. C., *Capillary Electrophoresis - Theory and Practice*, Academic Press Inc, San Diego, CA, 1992.
- [2] Li, S., *Capillary Electrophoresis*, J. Chromatography Library, 1993, **52**, Elsevier, London.
- [3] Masliyah, J. H., "Electrokinetic Transport Phenomena", AOSTRA Technical Publication Series 12#, Edmonton, 1994.
- [4] Smoluchowski, M. Z., *Phys. Chem.*, 1918, **93**, 29-35.
- [5] Jorgenson, J.W., Lukacs, K. D., "Capillary Zone Electrophoresis", *Science*, 1980, **222**, 266-273.
- [6] Hayes, M. A., Kheterpal, I. and Ewing, A. G., "Electroosmotic Flow Control and Surface Conductance in Capillary Zone Electrophoresis", *Anal. Chem.* 1993, **65**, 2010-2013.
- [7] Yao, X.W. and Regnier, F. E., "Manipulation of Electroosmotic Flow in Capillary Electrophoresis", *J. Chromatography.*, 1993, **636**, 21-29.
- [8] Tavares, M. F. M. and McGuffin V. L., "Theoretical Model of Electroosmotic Flow for Capillary Zone Electrophoresis", *Anal. Chem.*, 1995, **67**, 3687-3696.
- [9] Cohen, N. and Grushka, E., "Controlling Electroosmotic Flow in Capillary Zone Electrophoresis", *J. Chromatography A* 1994, **678**, 167-175.
- [10] Hayes, M. A., Kheterpal, I. and Ewing, A.G., "Effects of Buffer pH on Electroosmotic Flow Control by An Applied Radial Voltage for Capillary Zone Electrophoresis", *Anal. Chem.*, 1993, **65**, 27-31.
- [11] Hayes, M. A., Kheterpal, I. and Ewing, A. G. "Electroosmotic Flow Control and Surface Conductance in Capillary Zone Electrophoresis ", *Anal. Chem.* 1993, **65**, 2010-2013.

- [12] Hayes, M.A., Kheterpal, I. and Ewing, A. G., "Electroosmotic Flow Control and Monitoring With an Applied Radial Voltage for Capillary Zone Electrophoresis", *Anal. Chem.*, 1992, **64**, 512-516.
- [13] Huang, T. L., Wu and Lee, C. S., "Mechanistic Studies of Electroosmotic Control at the Capillary-Solution Interface", *Anal. Chem.*, 1993, **65**, 2887-2894.
- [14] Keely, C. A., Holloway, R. R., Van de Goor, T. A. A. M., and McManigill, D. "Dispersion on Capillary Electrophoresis with External Flow Control Methods", *Journal of Chromatography, A*, 1993, **652**, 283-289.
- [15] Dasgupta, P. K., and Liu, S. "Auxiliary Electroosmotic Pumping in Capillary Electrophoresis", *Anal. Chem.* 1994, **66**, 3070-3065.
- [16] Harrison, D. J., Fluri, K., Seiler, K., Fan, Z. H., Effenhauser, C. S., and Manz, A., "Micromachining A Miniaturized Capillary Electrophoresis-Based Chemical Analysis System on a Chip", *Science* 1993, **261**, 898-897.
- [17] Manz, A., Effenhauser, C. S., Burggraf, N., Harrison, D. J., Seiker, K., and Fluri, K., "Electroosmotic Pumping and Electrophoretic Separations for Miniaturized Chemical Analysis Systems", *J. Micromech. Microeng.*, 1994, **4**, 257-265.
- [18] Seiler, K., Fan, Z. H., Fluri, K., and Harrison, D. J. "Electroosmotic Pumping and Valveless Control of Fluid Flow Within A Manifold of Capillaries on A Glass Chip", *Anal. Chem.*, 1994, **66**, 15-23.
- [19] Fan, Z.H., and Harrison, D. J., "Micromachining of Capillary Electrophoresis Injectors and Separations on Glass Chips and Evaluation of Flow at Capillary Intersections", *Anal. Chem.*, 1994, **66**, 177-184.
- [20] Seiler, K., Harrison, D. J., and Manz, A. "Planar Glass Chips for Capillary Electrophoresis: Repetitive Sample Injection, Quantisation, and Separation Efficiency", *Anal. Chem.*, 1993, **65**, 1481-1488.
- [21] Harrison, D. J., Manz, A., Fan, Z., Ludi, H., and Widner, H. M. "Capillary Electrophoresis and Sample Injection Systems Integrated on a Planar Glass Chip", *Anal. Chem.*, 1992, **64**, 1926-1932.

- [22] Harrison, D. J., and Glavina, P. G, "Towards Miniaturized Electrophoresis and Chemical Analysis Systems in Silicon: an Alternative to Chemical Sensors ", *Sensors and Actuators B*, 1993, **10**, 107-116.
- [23] Davies, J. T., Rided, E. K., ' *Interfacial phenomena*', Academic press: New York, 1963.
- [24] Rice, C. L. and Whitehead, R., "Electrokinetic Flow in a Narrow Cylindrical Capillary", *The Journal of Physical Chemistry*, 1965, **69**, 4017-4023.
- [25] Levine, S., Marriott, R., Neale, G., and Wpstein, N, "Theory of Electrokinetic Flow in Fine Cylindrical Capillaries at High Zeta-Potentials", *Journal of Colloid and Interface Science*, 1975, **52**, 136-149.
- [26] Does, E. V., and Guiochon, G, "Timescales of Transient Processes in Capillary Electrophoresis", *Journal of chromatography A* , 1993, **652**, 263-275.
- [27] Henry, D. C . "The Cataphoresis of Suspended Parties, Part I . The Equation of Cataphoresis", *Proc. Roy. Soc, Lond.*, 1931, **133A**, 106-29.
- [28] Acton, F. S., " *Numerical Methods that Work*", Harper, Row, New York, 1970.
- [29] Bowen, W. R. M. Jenner, F., "Electroviscous Effect in Charged Capillaries", *Journal of Colloid and Interface Science*, 1995, **173**, 388-395.
- [30] Liu, S., and Masliyah, J.H, " A Decoupling Numerical Method for Fluid Flow ", *Int. J. Number. Methods fluid*, 1993, **16**, 659-682.
- [31] Kaushik, S., and Rubin , S.G., "Incompressible Navier-Stokes Solutions With a New Primitive Variable Solver", *Computers and Fluids*, 1995, **24** , 27-40.
- [32] Patankar, S. V. , " A Calculation Procedure for Two-Dimensional Elliptic Situations", *Number. Heat Transfer* 1981, **5**, 409-425.
- [33] Patankar, S. V. and D. B. Spalding, "A Calculation Procedure for Heat, Mass and Momentum Transfer in Three-dimensional Parabolic Flows," *Int. J. Heat Mass Transfer*, 1972, **15**, 1787-1793.
- [34] Patankar, S.V., "Numerical Heat Transfer and Fluid Flow", Hemisphere, Washington, D.C, 1980.

- [35] Van Doormal, J. P., and Raithby, G. D, "Enhancements of the Simple Method for Predicting Incompressible Fluid Flows", Numerical Heat Transfer, 1984, **7**, 147-163.
- [36] Bodoia , J. R., and Osterle , J. F, "Finite Difference Analysis of Plane Poiseuille and Coquette Flow Developments", Appl. Sci. Res., 1961, **A10**, 205-276.
- [37] Friedmann, M., Gillis, J., and Liron, N., "Laminar Flow in a Pipe at Low and Moderate Reynolds Numbers", Appl. Sci. Res., 1968, **19**, 426-433.
- [38] Atkinson, B., M. P. Bricklebank, C. C. H. Card, and Smith, J. M., "Low Reynolds Number Developing Flows", AIChE Journal, 1965, **15**, 548-553.
- [39] Morihara, H. and Cheng, R. T., "Numerical Solution of the Viscous Flow in the Entrance Region of Parallel Plates ", Journal of Computational Physics, 1973, **11**, 550-572.
- [40] Abarvanel . S., Bennett, B., Brandt, A., and Gillis, H, "Velocity Profiles of Flow at Low Reynolds Numbers", Journal of Applied Mechanics, 1970, **March**, 2-4.
- [41] Mcdonald, J. W., Denny, V. E., and Mills, A. F, " Numerical Solutions of the Navier-Stokes Equations in Inlet Regions", Journal of Applied Mechanics , 1972, **December**, 873-878.
- [42] Narang , B. S., and Krishnamorthy, G., "Laminar Flow in the Entrance Region of Parallel Plates ", Journal of Applied Mechanics , 1976, **March** , 186-188.
- [43] Al-Ali, H. H. and Selim , M. S., "Momentum and Heat Transfer in the Entrance Region of a Parallel Plate Channel: Developing Laminar Flow With Constant Wall Temperature", J. Computational Phys., 1972, **10**. 668-675.
- [44] Carvalho, T. M. B., Cotta, R. M., and Mikhailov, M. D, " Flow Development in Entrance Region of Ducts ", Communications in Numerical Methods in Engineering, 1993, **9**, 503- 509.
- [45] Perez Guerrero, J, S., and Cotta, R.M, " Integral Transform Solution of Developing Laminar Duct Flow in Navier-Stokes Formulation", International Journal for Numerical Methods in Fluids, 1995, **20**, 1203-1213.

- [46] Datta, R., Kotamarthi, V. R., "Electrokinetic Dispersion in Capillary Electrophoresis", *AIChE J.*, 1990, **36**, 916-926.
- [47] Aris, R., "On the Dispersion of a Solution in a Fluid Flowing through a Tube", *Proc. Roy. Soc., London*, 1956, **A235**, 67-77.
- [48] Hultquist, P. F., "Numerical methods for Engineers and Computer Scientists", The Benjamin/Cummings Publishing Company, Inc., CA, 1988.
- [49] Taylor, G. T. , "Dispersion of Soluble Matter in solvent Flowing Slowly through a Tube", *Proc. Roy. Soc. London*, 1953, **A219**, 186-193.